

AD _____

Award Number: DAMD17-03-1-0353

TITLE: Monitoring of Breast Tumor Response to Local
Chemotherapeutic Agent Delivered by Biodegradable Fibers

PRINCIPAL INVESTIGATOR: Jae G. Kim

CONTRACTING ORGANIZATION: The University of Texas at Arlington
Arlington, Texas 76019-0145

REPORT DATE: May 2004

TYPE OF REPORT: Annual

PREPARED FOR: U.S. Army Medical Research and Materiel Command
Fort Detrick, Maryland 21702-5012

DISTRIBUTION STATEMENT: Approved for Public Release;
Distribution Unlimited

The views, opinions and/or findings contained in this report are those of the author(s) and should not be construed as an official Department of the Army position, policy or decision unless so designated by other documentation.

REPORT DOCUMENTATION PAGEForm Approved
OMB No. 074-0188

Public reporting burden for this collection of information is estimated to average 1 hour per response, including the time for reviewing instructions, searching existing data sources, gathering and maintaining the data needed, and completing and reviewing this collection of information. Send comments regarding this burden estimate or any other aspect of this collection of information, including suggestions for reducing this burden to Washington Headquarters Services, Directorate for Information Operations and Reports, 1215 Jefferson Davis Highway, Suite 1204, Arlington, VA 22202-4302, and to the Office of Management and Budget, Paperwork Reduction Project (0704-0188), Washington, DC 20503

1. AGENCY USE ONLY (Leave blank)		2. REPORT DATE May 2004	3. REPORT TYPE AND DATES COVERED Annual (1 May 2003 - 30 Apr 2004)	
4. TITLE AND SUBTITLE Monitoring of Breast Tumor Response to Local Chemotherapeutic Agent Delivered by Biodegradable Fibers			5. FUNDING NUMBERS DAMD17-03-1-0353	
6. AUTHOR(S) Jae G. Kim				
7. PERFORMING ORGANIZATION NAME(S) AND ADDRESS(ES) The University of Texas at Arlington Arlington, Texas 76019-0145 E-Mail: jae@uta.edu			8. PERFORMING ORGANIZATION REPORT NUMBER	
9. SPONSORING / MONITORING AGENCY NAME(S) AND ADDRESS(ES) U.S. Army Medical Research and Materiel Command Fort Detrick, Maryland 21702-5012			10. SPONSORING / MONITORING AGENCY REPORT NUMBER	
11. SUPPLEMENTARY NOTES				
12a. DISTRIBUTION / AVAILABILITY STATEMENT Approved for Public Release; Distribution Unlimited				12b. DISTRIBUTION CODE
13. ABSTRACT (Maximum 200 Words) The goal of this research project is to investigate the possibilities of using NIRS to monitor the effects of chemotherapy and to reduce the side effects of chemotherapy by delivering the chemotherapeutic agent locally into the tumor. High dose of cyclophosphamide was administered to the rat through i.p. injection, and rat body weight and tumor volume were measured before and after administration of cyclophosphamide. The rat was given gas intervention from air to oxygen, and the dynamic changes of [HbO ₂], [Hb], and [Hb _{total}] were measured in real time during the experiments. I have compared the simultaneously measured hemodynamic changes from four different locations of the tumor and shown intratumoral heterogeneity in tumor vascular structure. Hemodynamic parameters obtained by fitting the measured data with our hemodynamic model was compared between before and after cyclophosphamide administration, and it was found that destruction of tumor occurs much faster in the well perfused region than in the poorly perfused region. In addition, decrease in maximum of Δ[HbO ₂] during oxygen intervention was also observed after chemotherapy. All the results support that we can apply NIRS to monitor the efficacy of cancer treatment such as radiation therapy, photodynamic therapy, and chemotherapy.				
14. SUBJECT TERMS near-infrared spectroscopy, ¹⁹ FMR pO ₂ mapping, biodegradable fiber				15. NUMBER OF PAGES 107
				16. PRICE CODE
17. SECURITY CLASSIFICATION OF REPORT Unclassified	18. SECURITY CLASSIFICATION OF THIS PAGE Unclassified	19. SECURITY CLASSIFICATION OF ABSTRACT Unclassified	20. LIMITATION OF ABSTRACT Unlimited	

NSN 7540-01-280-5500

Standard Form 298 (Rev. 2-89)
Prescribed by ANSI Std. Z39-18
298-102

Table of Contents

Cover.....	1
SF 298.....	2
Introduction.....	4
Body.....	5
Key Research Accomplishments.....	13
Reportable Outcomes.....	13
Conclusions.....	14
References.....	15
Appendices.....	17

Introduction

Chemotherapy has been used with other cancer therapies to increase the survival rate of patients, but it also causes serious side effects due to its great toxicity for tissues with high growth fractions such as the bone marrow, gastrointestinal epithelium, hair follicles, and gonadal tissue. For the breast cancer therapy, chemotherapy has been used as an adjuvant therapy or a neoadjuvant therapy (or induction chemotherapy). In both of the cases, a chemotherapeutic agent is given by systemic administration, and thus side effects are often occurred to breast cancer patients. Therefore, delivery of chemotherapeutic drugs only into breast cancer cells will reduce side effects of chemotherapy significantly, and the patients will be more comfortable during chemotherapy.

Currently, MRI and CT are the only tools for monitoring the effects of chemotherapy by measuring the tumor size. However, detecting early effects of therapy is needed to improve therapy efficiency and to increase patients' survival rate. In the last decade, significant investigations in both laboratory and clinical settings using near-infrared spectroscopy (NIRS) have been conducted for non-invasive, quantitative measurements and imaging of tissue oxygenation of the brain^{1,2,3,4,5} and muscle^{6,7,8} *in vivo*. Recently, Liu *et al.*⁹ and other groups^{10,11} have shown that the NIR techniques can be also used for monitoring vascular oxygen dynamics of breast tumors during respiratory intervention non-invasively.

We have previously studied tumor oxygenation under gas intervention using NIRS and found that oxyhemoglobin concentration changes during gas intervention can be fitted by a two-exponential equation containing two time constants.^{Error! Bookmark not defined.} We suggested that those two time constants are related to blood perfusion in tumors. If a drug is delivered into a breast tumor by drug-loaded, biodegradable fibers, the drug will be released most likely into the tumor cells, and this will decrease the side effects of chemotherapy. Our hypothesis for this proposed work is that: when the drug is delivered locally by biodegradable fibers to the tumor cells, changes in blood perfusion in the tumor will occur and can be observed by the NIRS measurement. If the tumor vascular and tissue oxygenation changes during respiratory challenges show different and significant responses before and after the administration of the chemotherapeutic agent, it may indicate that NIRS could be a novel technical means in monitoring early effects of chemotherapy, which will help physicians make proper tumor treatment plans for individual patients.

Therefore, this study will allow us to validate a non-invasive tool that can monitor the effects of chemotherapy on breast tumors and to demonstrate advantages of local drug delivery using biodegradable fibers for breast tumor treatment. Our study may help breast cancer patients under chemotherapy have a higher survival rate and better quality of life with reduced side effects and proper tumor treatment selection.

Objectives:

The goals of this research are to evaluate NIRS technique and ¹⁹F MR pO₂ mapping as non-invasive tools for monitoring the drug effects in breast tumors and to compare the effects of systemically delivered drug and locally delivered drug with embedded biodegradable fibers. The project has five specific aims and tasks as shown below:

Aim 1: to monitor tumor vascular oxygenation during oxygen/carbogen interventions using both NIRS and ¹⁹F MR pO₂ mapping after a systemic drug delivery.

Aim 2: to compare the effects of the systemically delivered drugs on the vascular and tissue oxygenation of the breast tumors in order to validate the monitoring capability of the two techniques for breast cancer treatment.

Aim 3: to develop/implement biodegradable fibers loaded with a chemotherapeutic agent for local drug delivery at the specific breast cancer site.

Aim 4: to monitor tumor vascular oxygenation during oxygen/carbogen interventions using both NIRS and ^{19}F MR pO_2 mapping after a local drug delivery through a biodegradable fiber.

Aim 5: to compare the chemotherapy effects between local drug delivery and systemic drug delivery.

Task 1: To obtain the knowledge and appropriate training for handling laboratory animals and performing the measurements. (months 1-7):

- a. Get training in handling laboratory animals (month 1).
- b. Study the fundamentals and operation of the NIR oximeter (months 2-3).
- c. Study the fundamentals and operation of the ^{19}F MR EPI of HFB method (months 4-6).
- d. Gain basic understanding of tumor physiology, oxygenation and dynamic processes (month 7).

Task 2: To monitor tumor vascular oxygenation during oxygen/carbogen interventions using both NIRS and ^{19}F MR pO_2 mapping after a systemic drug delivery. (months 8-16):

- a. To implant breast tumors on Fisher rats (month 8).
- b. To perform NIRS and ^{19}F MR pO_2 mapping measurement on breast tumors with oxygen/carbogen inhalation after systemic drug administration, and evaluate oxyhemoglobin level and tumor tissue pO_2 changes from NIRS and ^{19}F MR pO_2 mapping, respectively. (months 9-14)
- c. To measure tumor size and hemoglobin level in blood periodically after systemic drug delivery to observe the effects of systemic chemotherapy. (months 9-14)
- d. To compare the effects of the systemically delivered drugs on the vascular and tissue oxygenation of the breast tumors in order to validate the monitoring capability of the two techniques for breast cancer treatment. (month 15)
- e. To study the effects of the systemically delivered drug, e.g. tumor size reduction and time constant during respiratory changes. (month 16)

Body of the Report

As mentioned above, the purposes of this project are to deliver a therapeutic agent into the breast tumor directly by biodegradable fibers and to utilize NIRS and ^{19}F MR pO_2 mapping as tools to monitoring the therapeutic effects of the chemotherapeutic agent. In the first year, my focus was to obtain the appropriate knowledge and skills for conducting the project (months 1-7), and to perform the measurements of vascular oxygen dynamics in breast tumors by using NIRS system during systemic cancer drug delivery. I have mainly accomplished these tasks, as reported below:

Accomplishments during the first period (months 1-7):

- a. Obtained the skills for handling laboratory animals. I have taken the animal handling class provided by the University of Texas Southwestern Medical Center at Dallas, also taken the online training from the University of Texas at Arlington, and practiced saline injection through i.p. and i.v.
- b. Studied the fundamentals and operation of the NIR oximeter (see the reportable outcomes).

- c. Studied the fundamentals and operation of the ^{19}F MR EPI of HFB method. However, this method has not been used in the first year of project due to mismatch of the animal and tumor implantation schedule.
- d. Gained basic understanding of cell biology and tumor biology. I have taken a course of Cell Physiology at the University of Texas Arlington and also Molecular and Cell Biology of Cancer provided by the University of North Texas Health Science Center at Fort Worth (spring 2004). In addition, I have taken a "Drug Delivery" class at the University of Texas Arlington (fall 2003) since I will use the local drug delivery method in my second year.
- e. Additionally, I have obtained the skills for fabricating the biodegradable fibers which will be necessary for the second-year study of this project. (this was originally scheduled for months 17-18)

- Fundamentals of NIRS system.

NIR light (700 to 900 nm), where photon transport in tissue is dominated by light scattering rather than absorption, has the maximal penetration depth (several centimeters) in tissue, therefore enabling *in vivo* sampling of large tissue volumes, such organs as the breast, the brain, and skeletal muscles, or deep tumors. Our multi-channel NIR spectroscopy system has the ability to measure light signals from eight different locations, but due to the finite tumor size, we used only four detectors to monitor tumor vascular oxygenation dynamics during respiratory challenges. In common with our previous work,^{9,12} we assume that oxyhemoglobin (HbO_2) and deoxyhemoglobin (Hb) are the only significant absorbing materials in the blood-perfused tumor tissue. The absorption coefficients comprise the extinction coefficients for deoxyhemoglobin and oxyhemoglobin multiplied by their respective concentrations (Eqs. 1 and 2) at 730 nm and 850 nm, that have been employed in our multi-channel NIRS system.

$$\mu_a^{730} = \epsilon_{\text{Hb}}^{730}[\text{Hb}] + \epsilon_{\text{HbO}_2}^{730}[\text{HbO}_2], \quad (1)$$

$$\mu_a^{850} = \epsilon_{\text{Hb}}^{850}[\text{Hb}] + \epsilon_{\text{HbO}_2}^{850}[\text{HbO}_2]. \quad (2)$$

Based on modified Beer-Lambert's law, the data presented in this report were analyzed using amplitude values to find the changes in light absorption (Eq. 3). By manipulating Equations 1-3, changes in oxygenated hemoglobin, deoxygenated hemoglobin and total hemoglobin (Hb_{total}) concentrations were calculated from the transmitted amplitude of light through the tumor (Eqs. 4, 5 and 6).

$$\mu_{aB} - \mu_{aT} = \log(A_B/A_T) / L, \quad (3)$$

$$\Delta[\text{HbO}_2] = [-0.674 \cdot \log(A_B/A_T)^{730} + 1.117 \cdot \log(A_B/A_T)^{850}] / L, \quad (4)$$

$$\Delta[\text{Hb}] = [0.994 \cdot \log(A_B/A_T)^{730} - 0.376 \cdot \log(A_B/A_T)^{850}] / L, \quad (5)$$

$$\Delta[\text{Hb}]_{\text{total}} = \Delta[\text{Hb}] + \Delta[\text{HbO}_2] = [0.32 \cdot \log(A_B/A_T)^{730} + 0.741 \cdot \log(A_B/A_T)^{850}] / L, \quad (6)$$

where A_B = baseline amplitude; A_T = transition amplitude; L = optical pathlength between the source and detector. The constants contained in these equations were computed with the extinction coefficients for oxy- and deoxy-hemoglobin at the two wavelengths used.¹³ In principle, L should be equal to the source-detector separation, d , multiplied by a differential pathlength factor (DPF), i.e., $L = d \cdot \text{DPF}$. However, little is known about DPF for tumors, although a DPF value of 2.5 has been used by others.¹¹ Since our focus is on dynamic changes and relative values of tumor $[\text{HbO}_2]$ in response to oxygen intervention, we have taken the approach of including the DPF in the unit, and eq. (4) becomes as follows:

$$\Delta[\text{HbO}_2] = [-0.674 \cdot \log(A_B/A_T)^{730} + 1.117 \cdot \log(A_B/A_T)^{850}] / d, \quad (7)$$

where d is the direct source-detector separation in cm, and the unit of $\Delta[\text{HbO}_2]$ in Eq. (7) is mM/DPF.

Accomplishments during the second period (months 8-12):

a. Dynamic responses of breast tumor $\Delta[\text{HbO}_2]$ to oxygen intervention monitored by multi-channel NIRS

The dynamic response of tumor oxygenation to oxygen gas intervention has been observed by multi-channel NIRS system. In this project, four detectors were placed on the side of tumor and light source probe was located centrally on the top of tumor, providing us with four different regional signals of tumor vascular oxygenation during oxygen inhalation (Figure 1). Changes of $[\text{HbO}_2]$, $[\text{Hb}]$, and $[\text{Hb}_{\text{total}}]$ were simultaneously measured on a group of 5 rats during a sequence of air to oxygen and then to air for studying the dynamic response of tumor oxygenation to oxygen intervention.

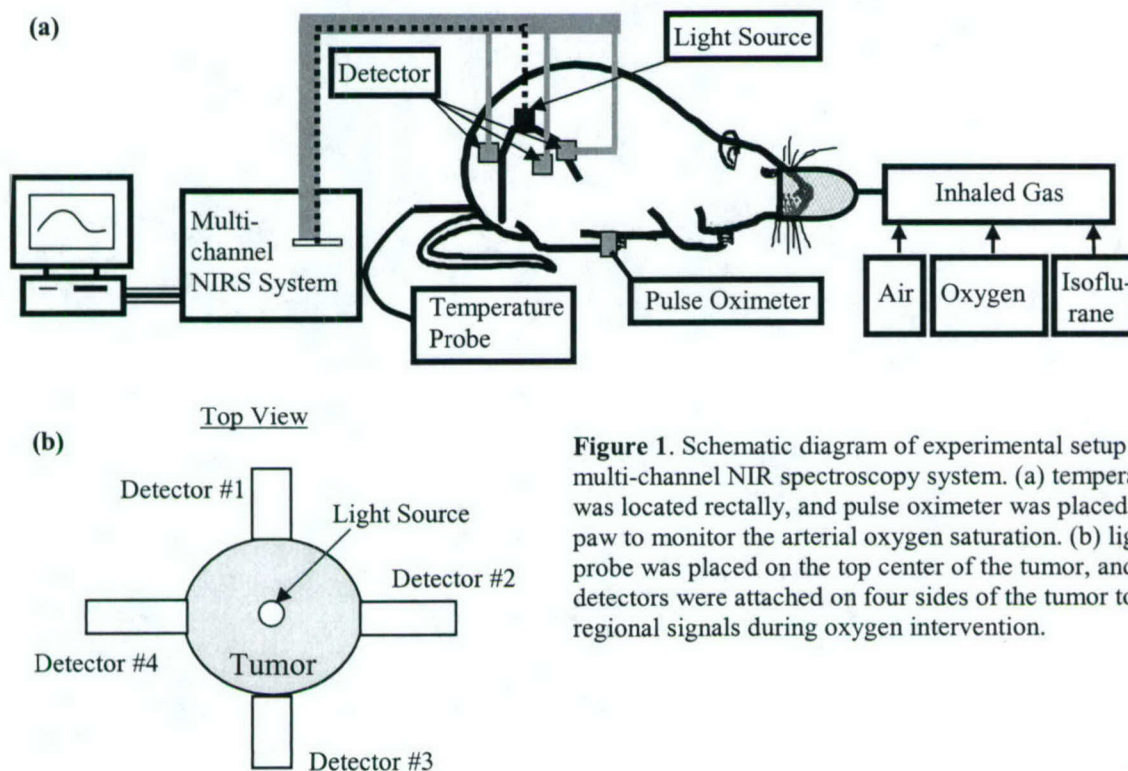


Figure 1. Schematic diagram of experimental setup for the multi-channel NIR spectroscopy system. (a) temperature probe was located rectally, and pulse oximeter was placed on the hind paw to monitor the arterial oxygen saturation. (b) light source probe was placed on the top center of the tumor, and four detectors were attached on four sides of the tumor to detect the regional signals during oxygen intervention.

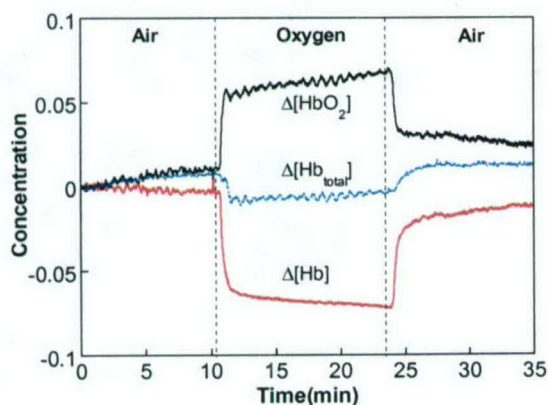


Figure 2. Time course of tumor vascular $\Delta[\text{HbO}_2]$, $\Delta[\text{Hb}]$, and $\Delta[\text{Hb}_{\text{total}}]$ for a representative 13762NF breast tumor with the inhaled gas under the sequence of air-oxygen-air.

A representative result is shown in Fig. 2. After 10 minutes of air breathing measurement as the baseline, the inhaled gas was switched from air to oxygen, causing a sharp increase in $\Delta[\text{HbO}_2]$ ($p < 0.0001$ 1 min. after gas switch) followed by a further gradual, but significant increase over the next 13 min ($P < 0.0001$). However, $\Delta[\text{Hb}_{\text{total}}]$ first dropped rapidly after switching gas from air to oxygen and then became stabilized during the next 13 minutes of oxygen inhalation. This behavior is expected since oxygen intervention may cause vasoconstriction of artery and result in blood flow decreases, which reduces blood volume. After returning to air inhalation, $\Delta[\text{HbO}_2]$ decreased and $\Delta[\text{Hb}_{\text{total}}]$ increased, both reaching approximately their respective baseline level. This result clearly shows that an NIRS can monitor the changes of blood oxygenation or blood volume in tumor dynamically and in real-time.

b. Body weight and tumor volume changes during chemotherapy

The tumor type, which we are using, is murine mammary adenocarcinomas 13762NF, and this tumor type is highly responsive to alkylating agents and platinum chemotherapeutic agents.¹⁴ Cyclophosphamide, one of alkylating agents, has been used in various types of cancer such as leukemia, ovarian cancer and breast cancer.¹⁵ We have injected cyclophosphamide into the rat through i. p. with a single high dose of 200 mg/kg for this experiment to see whether we can detect acute effects of cyclophosphamide on tumor vascular oxygenation dynamics. Some rats were failed to survive during the treatment, but the others survived with apparent reduction of tumor volume during the 10 days after i. p. injection of cyclophosphamide. Figures 3a and 3b show changes in rat body weight and tumor volume, respectively, before and after administration of cyclophosphamide. (Day 0 was the day for the injection.) These Figures show clearly decreases in rat body weight as well as in tumor volume for 5 experimental rats.

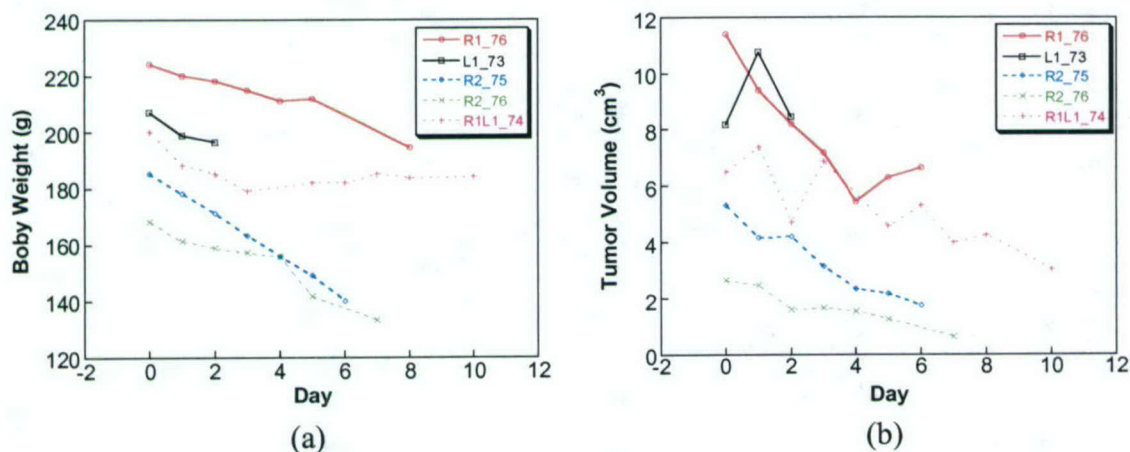


Figure 3. Changes of rat body weight (a) and tumor volume (b) during chemotherapy.

c. Intratumoral heterogeneity of vascular oxygenation observed by multi-channel NIRS

Solid tumors are known to exhibit heterogeneous blood flow distribution.^{16,17} Intensive studies from Mason's group using ^{19}F MR [*FREDOM* (Fluorocarbon Relaxometry using Echo planar imaging for Dynamic Oxygen Mapping)] have revealed intratumoral heterogeneity of pO_2 distribution and also heterogeneous response to hyperoxic gas breathing.^{18,19,20} The findings of severe pO_2 heterogeneity in tumors suggest the heterogeneous distribution of blood flow, since tissue pO_2 level is determined by a

balance between the supply of oxygen from blood vessels and the oxygen consumption rate of tissue cells.²¹ Unlike *FREDOM*, near-infrared spectroscopy (NIRS) techniques measure hemoglobin oxygen saturation and concentration *in vivo*, providing information on vascular oxygenation of the measured sample/organ, such as the brain^{3,4,22} and animal tumors.^{9,11,23} Therefore, multi-channel NIRS can detect signals from many locations of a solid tumor, enabling us to study vascular heterogeneity of a tumor.

In our experiment, we have applied four detectors and one light source on the rat breast tumors, and the setup has been shown in Fig. 1. After 10 minutes of baseline measurement with air breathing, gas was switched to pure oxygen, which caused a rapid increase of tumor $\Delta[\text{HbO}_2]$. These changes were measured simultaneously from 4 locations of the tumor, and Fig. 4 shows a representative set of data. Red circles show the raw data measured by multi-channel NIRS, and the solid black lines represent the fitted curves using our double-exponential model for hemodynamics during oxygen intervention⁹. As we can see from these figures, none of the data from four detectors are identical even though some are showing quite similar trends of $\Delta[\text{HbO}_2]$.

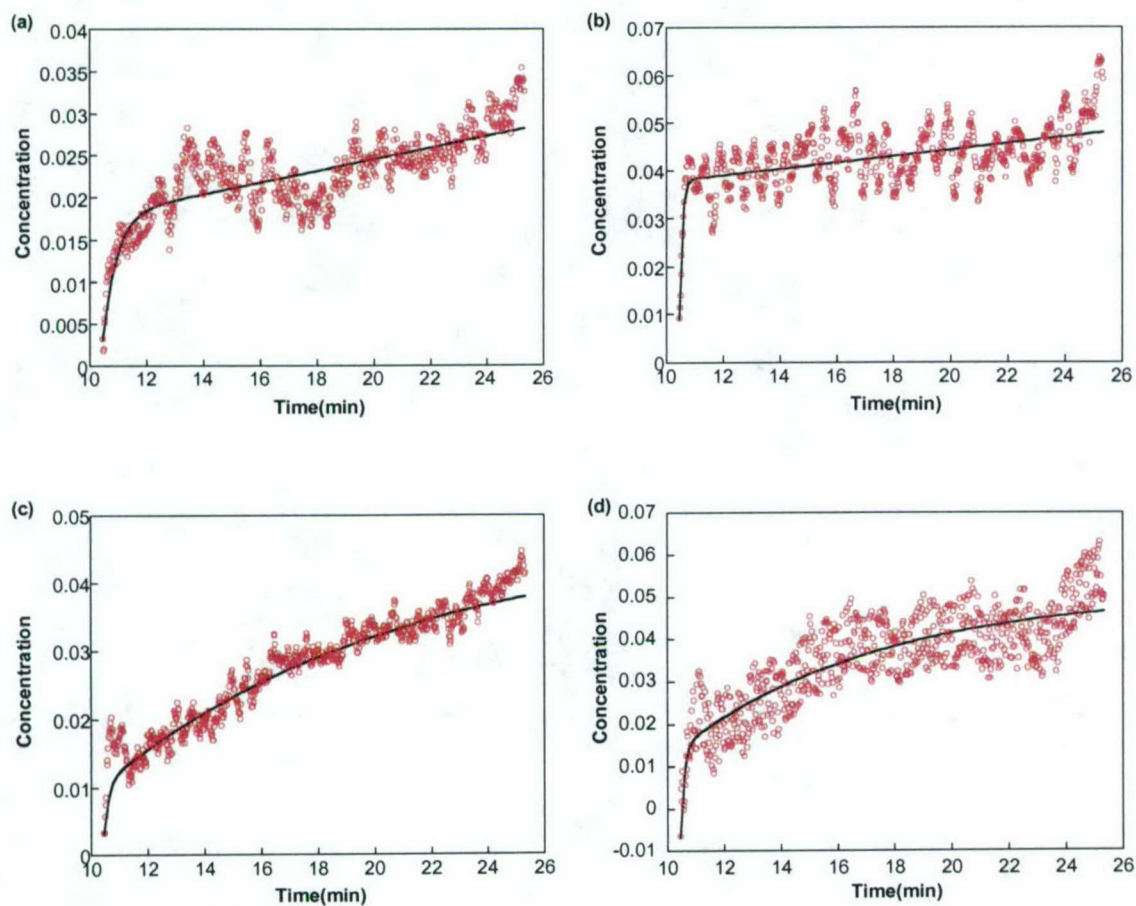


Figure 4. Dynamic changes of tumor $[\text{HbO}_2]$ from four detectors in a rat breast tumor (Tumor A with a volume of 8.2 cm^3). The rising part of $\Delta[\text{HbO}_2]$ from the four detectors was fitted using double-exponential expressions and Fig. 4(a)-4(d) are taken from detectors #1-#4, respectively. In this case, the tumor was not treated yet.

Table 1. Summary of vascular oxygen dynamics determined at the four detectors from Figure 4 for Tumor A.

Detector	A1	A2	τ_1	τ_2	$A1/A2 (= \gamma_1/\gamma_2)$	τ_1/τ_2	f_1/f_2
No. 1	0.013	0.027	0.48	24.3	0.48	0.02	24
No. 2	0.029	0.026	0.09	29.8	1.12	0.003	373
No. 3	0.008	0.036	0.15	10.6	0.22	0.014	16
No. 4	0.021	0.037	0.12	7.25	0.57	0.017	34

To compare the data taken from four locations of the tumor more clearly, the time constants and amplitudes from the four fitted curves are summarized in Table 1. The ratios of γ_1/γ_2 and f_1/f_2 basically characterize tumor vascular structure and blood perfusion within the volume of tumor interrogated by light.⁹ In principle, when γ_1/γ_2 is close to 1, it implies that the measured optical signal results equally from both region 1 (i.e., well perfused region) and 2 (i.e., poorly perfused region); if $\gamma_1/\gamma_2 < 1$, the measured signal results more from region 2 than region 1 [Figures 3(a), 3(c) and 3(d)]. As Table 1 demonstrates, only detector #2 has a ratio of γ_1/γ_2 slightly higher than 1, and the readings from detectors #1, #3 and #4 have the ratios of γ_1/γ_2 less than 1. This may suggest that the tumor volume that was optically interrogated by detector #2 consists of more volumes from well perfused region than poorly perfused region, while most of other tumor volumes detected by detectors #1, #3 and #4 are composed of more poorly perfused regions. Furthermore, all the ratios of f_1/f_2 from Tumor A at the four locations are much greater than 1, indicating that the blood perfusion rate in well perfused region is much greater than that in poorly perfused region. Especially, f_1/f_2 from detector #2 is 10 to 20 times higher than those from detectors #1, #3, and #4, showing a high level of intratumoral heterogeneity in dynamic vascular structure.

d. Monitoring vascular hemodynamics of breast tumors before and after chemotherapy

The hemodynamics of tumor during oxygen intervention was measured before and after administration of cyclophosphamide. The representative data from tumor B are shown in Fig. 5. As it was mentioned before, there were 4 detectors on the surface of tumor, and Fig. 5 shows the acute and then gradual changes of $[HbO_2]$ after switching the breathing gas from air to oxygen, and the data were observed by detector #1 from day 0 to day 5. This figure clearly demonstrates that we can observe significant changes in tumor hemodynamics after chemotherapy by giving respiratory challenges. The fitted parameters from our mathematical model are summarized in Table 2 to compare the changes in hemodynamic parameters before and after administration of cyclophosphamide. The rising part of $\Delta[HbO_2]$ from detector #1 was fitted using either single- or double- exponential expression.

Table 2. Summary of vascular oxygen dynamics determined at detector #1 from Tumor B before and after cyclophosphamide administration.

Day	A1	A2	τ_1	τ_2	$A1/A2 (= \gamma_1/\gamma_2)$	τ_1/τ_2	f_1/f_2
0	0.044	0.031	0.23	25.21	1.42	0.0091	156
1	0.032	0.033	0.13	11.36	0.97	0.0114	85
3	0.0087	0.014	0.089	8.36	0.62	0.0106	58
5	0.0087		1.27				

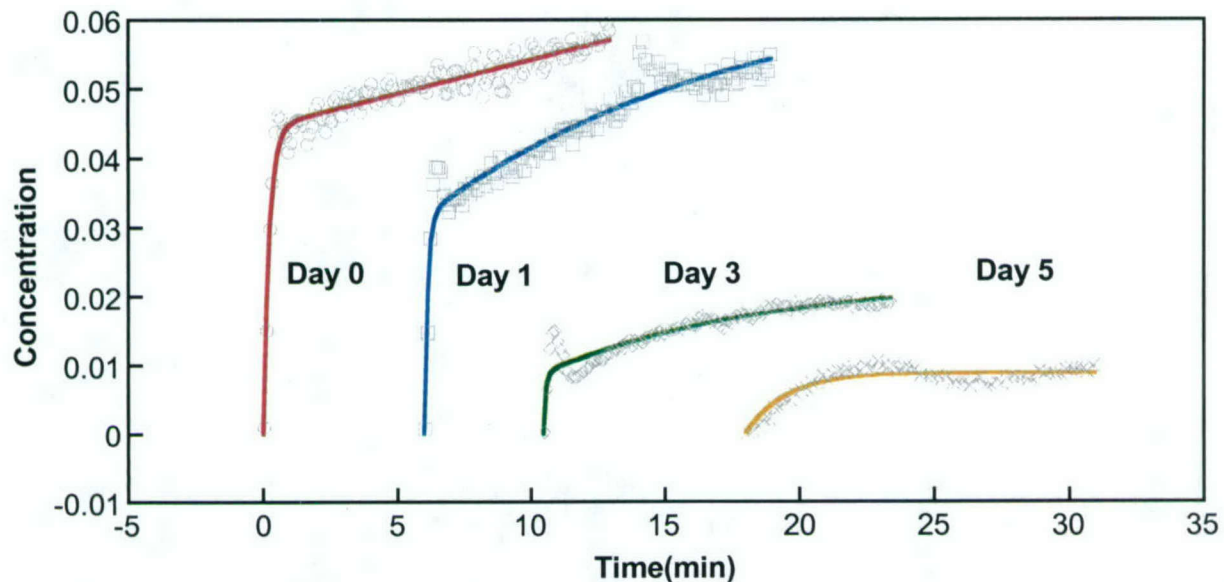


Figure 5. Dynamic changes of $[\text{HbO}_2]$ taken at detector #1 from a rat breast tumor before and after administration of cyclophosphamide (Tumor B with a volume of 5.3 cm^3 at day 0). The rising part of $\Delta[\text{HbO}_2]$ from detector #1 was fitted using either single- or double-exponential expression.

At day 0, we can see that γ_1/γ_2 is higher than 1, indicating that the measured signal results more from the well perfused region than poorly perfused region. However, this ratio becomes less than 1 after injection of cyclophosphamide (Day 1 and 3). This may be explained by destruction of vascular structure in tumor after chemotherapy as follows. After administration of cyclophosphamide, it will be circulated in blood vessels and will be more delivered to the tumor cells in the well perfused region than those in the poorly perfused region. This will cause more apoptosis of tumor cells in the well perfused region than that in the poorly perfused region, eventually causing decreases in tumor volume in the well perfused region more than that in the poorly perfused region. Then, the tumor volume optically interrogated by detector #1 will have less contribution from the well perfused region than the poorly perfused region, leading to a decrease of γ_1/γ_2 , after administration of cyclophosphamide.

After cyclophosphamide administration, the perfusion rate ratio, f_1/f_2 , was also decreased. At day 0, f_1/f_2 is very high, which means there is a big difference of perfusion rate between the well perfused and poorly perfused region in tumor. However, this ratio significantly decreased at day 1 and 3 after cyclophosphamide administration, representing that the perfusion rate gap between the well perfused region and poorly perfused region became much smaller than that from day 0. At day 5, the changes of $[\text{HbO}_2]$ during oxygen intervention does not show any bi-phasic behavior anymore, and it was fitted by a single-exponential model. This may indicate that most of tumor cells in the well perfused region possibly destroyed by the effect of cyclophosphamide, and vascular structure has been totally changed.

Similar experiments have been performed on more rat tumors using the same methodology and analysis. A decrease of maximum $\Delta[\text{HbO}_2]$ ($\Delta[\text{HbO}_2]_{\text{max}}$) during oxygen inhalation was clearly observed from all tumors after cyclophosphamide administration. Figure 6 shows a set of dynamic changes of $[\text{HbO}_2]$ right after switching the gas from air to oxygen at day 0 and 3 after cyclophosphamide administration. All of the four tumors showed rapid increase of $\Delta[\text{HbO}_2]$ to the oxygen inhalation, but $\Delta[\text{HbO}_2]_{\text{max}}$ was reduced at day 3 by 20 to 70% compared to $\Delta[\text{HbO}_2]_{\text{max}}$ at day 0. We notice that the decrease of $\Delta[\text{HbO}_2]_{\text{max}}$ at day 3 is mainly from the decrease of A1 (amplitude of rapid increase in $\Delta[\text{HbO}_2]$) rather than A2 (amplitude of gradual increase in $\Delta[\text{HbO}_2]$). Table 3 summarizes the fitted parameters of Fig. 6. As seen from Table

3, γ_1/γ_2 is decreased for all four tumors at day 3 compared to day 0. The perfusion rate ratio, f_1/f_2 , has also been decreased for all tumors at day 3 compared to day 0. These observations are in good agreement with the result shown in Figure 5 and Table 2. All of the results may suggest that the administration of cyclophosphamide treats the tumor well with well perfused vasculature, but not well for the tumors with poorly perfused vasculature. Furthermore, our study shown here proves that we can monitor the effects of chemotherapy in tumor by detecting changes of hemodynamics during respiratory challenges using near infrared spectroscopy.

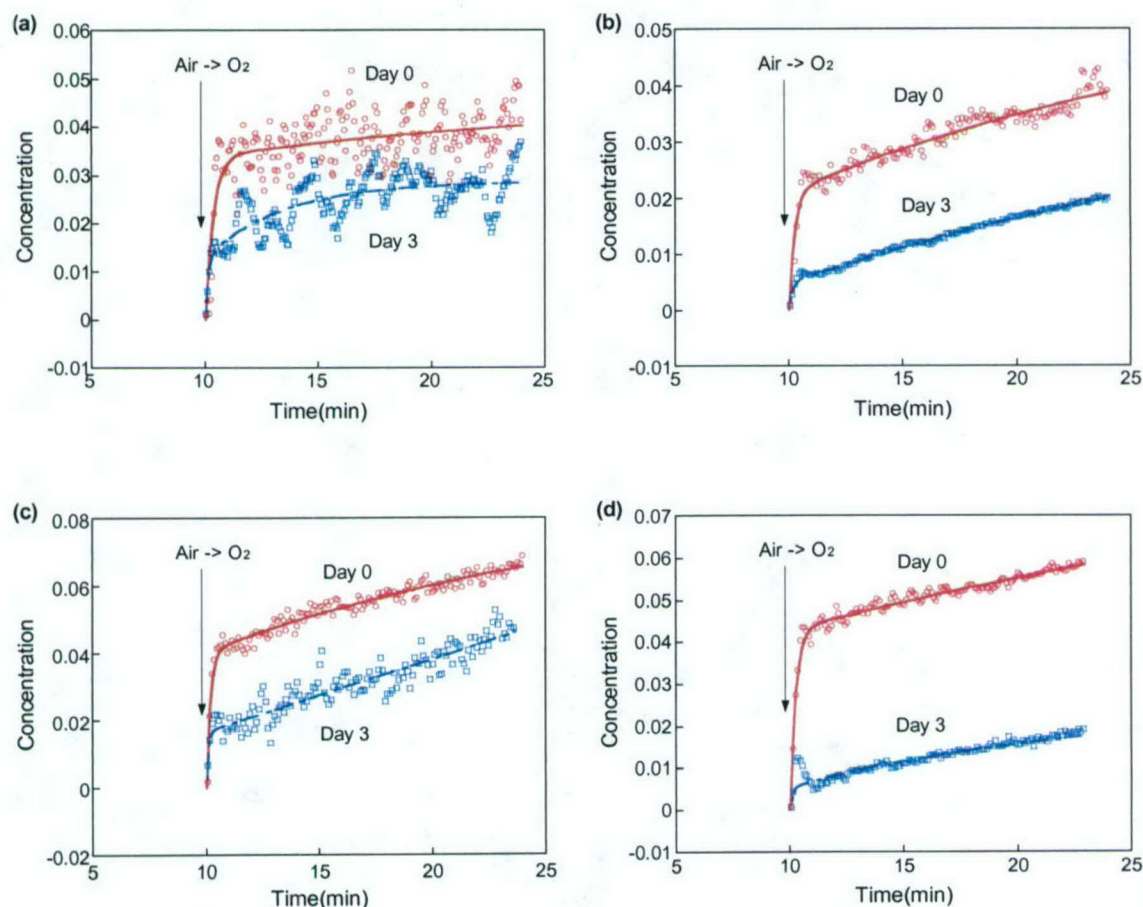


Figure 6. Dynamic changes of $[HbO_2]$ after switching the gas from air to oxygen from four individual rat breast tumors. Red open circles and solid lines indicate raw data of the changes of $[HbO_2]$ at day 0 and fitted curve, respectively. Blue open squares and solid lines indicate raw data of the changes of $[HbO_2]$ at day 3 after cyclophosphamide administration and fitted curve, respectively.

Table 3. Summary of vascular oxygen dynamics determined at day 0 and day 3 from four tumors.

Tumor	Day	A1	A2	τ_1	τ_2	$A1/A2$ ($=\gamma_1/\gamma_2$)	τ_1/τ_2	f_1/f_2
Fig.6a	0	0.034	0.015	0.34	23.92	2.27	0.014	159
	3	0.013	0.016	0.11	3.57	0.81	0.031	26
Fig.6b	0	0.021	0.036	0.24	20.51	0.58	0.012	50
	3	0.005	0.045	0.14	34.10	0.11	0.004	27
Fig.6c	0	0.040	0.046	0.17	17.87	0.87	0.010	91
	3	0.015	0.081	0.07	29.54	0.19	0.002	76
Fig.6d	0	0.043	0.066	0.25	49.33	0.65	0.005	129
	3	0.0053	0.019	0.10	12.23	0.28	0.008	34

Key Research Accomplishments:

- Obtained the main knowledge and skills for conducting this project. (training in handling laboratory animals, studying the fundamentals and operation in the NIR oximeter and ^{19}F MR pO_2 mapping method, studying the drug delivery and also tumor biology, learning the fabrication of biodegradable fiber.)
- Observed the changes of tumor volume and body weight of rats during chemotherapy. This clearly showed the response of tumor to the chemotherapy.
- Studied the intratumoral heterogeneity of breast tumors by multi-channel NIRS. Changes of $[\text{HbO}_2]$, $[\text{Hb}]$ and $[\text{Hb}_{\text{total}}]$ during gas interventions were monitored by multi-channel NIRS in real time, and the data clearly revealed that there is dynamic intratumoral heterogeneity in tumor vascular structure during oxygen intervention.
- Investigated the dynamic response of tumor vascular $\Delta[\text{HbO}_2]$ to oxygen intervention before and after cyclophosphamide administration. The ratios of γ_1/γ_2 and f_1/f_2 have been changed during therapy, indicating that changes in hemodynamics of $\Delta[\text{HbO}_2]$ during oxygen intervention before and after cyclophosphamide can be applied to find the efficacy of chemotherapeutic agent.

Reportable Outcomes

Manuscripts for Peer-reviewed Journals:

- Yueqing Gu, Vincent A. Bourke, **Jae G. Kim**, Anca Constantinescu, Ralph P. Mason, Hanli Liu, "Dynamic response of breast tumor oxygenation to hyperoxic respiratory challenge monitored with three oxygen-sensitive parameters", *Applied Optics*, 42(16), 2960-2967 (2003)
- Hanli Liu, Yueqing Gu, **Jae G. Kim**, Ralph P. Mason, "Near infrared spectroscopy and imaging of tumor vascular oxygenation", *Imaging in Biological Research, Part B* (P. Machael Conn ed.) *Methods in Enzymology*, 386, pp. 349-378 (2004)
- Jae G. Kim**, Hanli Liu, "Investigation of Breast Tumor Hemodynamics: Dynamic Phantoms and FEM Simulations", in preparation and will be submitted to *applied optics*.
- Jae G. Kim**, Anca Constantinescu, Ralph P. Mason, Hanli Liu, "Non-Uniform Tumor Vascular Oxygen Dynamics Monitored by Multi-Channel Near-Infrared Spectroscopy, in preparation and will be submitted to *J. Biomedical Optics*.

Presentations and Proceeding papers:

1) **Jae G. Kim**, and Hanli Liu, "Investigation of breast tumor hemodynamics using tumor vascular phantoms and FEM simulations", in Biomedical Topical Meetings on CD-ROM (The Optical Society of America, Washington, DC, 2004), WF16.

Conclusions

From the work that I have conducted up-to-date, the following conclusions can be drawn.

- a. The dynamic responses of $\Delta[\text{HbO}_2]$ after switching the breathing gas from air to oxygen proved that there exists dynamic intratumoral heterogeneity in breast tumor vascular structure during oxygen intervention. During the oxygen inhalation, all four detectors showed rapid increases of $\Delta[\text{HbO}_2]$ followed by a gradual increases. (The bi-phasic behavior of $\Delta[\text{HbO}_2]$ implies that the signal in the fast phase results from well perfused regions, and the signal in the slow phase results from poorly perfused regions.) However, two ratios (γ_1/γ_2 and f_1/f_2) from the double-exponential fitting to the data showed large differences among the signals taken from each detector. The differences suggest that some parts of tumor consist of more well perfused regions than other parts. The results demonstrate the capability of NIR spectroscopy as a noninvasive, real time monitoring tool for tumor vascular oxygenation.
- b. Changes in hemodynamic parameters before and after chemotherapy were monitored from breast rat tumors. The results showed that $\Delta[\text{HbO}_2]_{\text{max}}$ during oxygen inhalation has been decreased largely after cyclophosphamide administration, which is consistent with the reduction of tumor size. Comparing the two ratios (γ_1/γ_2 and f_1/f_2) before and after the drug injection revealed that tumor blood volume in the well perfused region may be decreased faster than that in the poorly perfused region. Our results may imply that destruction of tumor cells occurred more efficiently in the well perfused region than in the poorly perfused region of tumor. This is expected because the administered drug will be delivered much easier to the tumor cells near the well perfused region than those far from the blood vessels. All of our data obtained in Year 1 prove that measuring hemodynamics of breast tumor during gas intervention can be feasibly used for monitoring the efficacy of cancer therapy, such as radiation therapy, photodynamic therapy, and chemotherapy.

Reference

1. M. Fabiani, G. Gratton, and P. M. Corballis, "Noninvasive near infrared optical imaging of human brain function with subsecond temporal resolution," *J. Biomed. Optics*, **1**(4), pp. 387-398 (1996).
2. R. Wenzel, H. Obrig, J. Ruben, K. Villringer, A. Thiel, J. Bernarding, U. Dirnagl, and A. Villringer, "Cerebral blood oxygenation changes induced by visual stimulation in humans," *J. Biomed. Optics*, **1**(4), pp. 399-404 (1996).
3. M. Cope, and D.T. Delpy, "A system for long term measurement of cerebral blood and tissue oxygenation in newborn infants by near infrared transillumination," *Med. Biol. Eng. Comp.*, **26**, 289-294 (1988).
4. B. Chance, E. Anday, S. Nioka, S. Zhou, L. Hong, K. Worden, C. Li, T. Murray, Y. Ovetsky, D. Pidikiti, and R. Thomas, "A novel method for fast imaging of brain function, non-invasively, with light," *Optics Express*, **2**(10), pp. 411-423, (1998).
5. A. M. Siegel, J. A. Marota, J. Mandeville, B. Rosen, D. A. Boas, "Diffuse optical tomography of rat brain function: a comparative study with fMRI," to appear *Proc. SPIE-Int. Soc. Opt. Eng.*, vol. **3597**, (1999).
6. S. Homma, T. Fukunaga, and A. Kagaya, "Influence of adipose tissue thickness on near infrared spectroscopic signals in the measurement of human muscle," *J. Biomed. Optics*, **1**(4), pp. 418-424 (1996).
7. M. Ferrari, Q. Wei, L. Carraresi, R. A. De Blasi, and G. Zaccanti, "Time-resolved spectroscopy of the human forearm," *J. Photochem. Photobiol. B: Biol.*, **16**, pp. 141-153, (1992).
8. H. Long, G. Iech, S. Nioka, S. Zhou, and B. Chance, "CW imaging of human muscle using near infrared spectroscopy," OSA Trends in Optics and Photonics Series, Advances in Optical Imaging and Photon Migration, ed. By J. G. Fujimoto and M. S. Patterson, **21**, pp. 256-259 (1998).
9. H. Liu, Y. Song, K. L. Worden, X. Jiang, A. Constantinescu, and R. P. Mason, "Noninvasive investigation of blood oxygenation dynamics of tumors by near-infrared spectroscopy," *Appl. Opt.*, **39**, pp. 5231-5243, (2000).
10. E. L. Hull, D. L. Conover, and T. H. Foster, "Carbogen-induced changes in rat mammary tumour oxygenation reported by near infrared spectroscopy," *Brit. J. of Cancer*, **79**, pp. 1709-1716 (1999).
11. R. G. Steen, K. Kitagishi, and K. Morgan, "In vivo measurement of tumor blood oxygenation by near-infrared spectroscopy: Immediate effects of pentobarbital overdose or carmustine treatment," *J. of Neuro-Oncology*, **22**, pp. 209-220 (1994).
12. J. G. Kim, D. Zhao, Y. Song, A. Constantinescu, R. P. Mason, and H. Liu, "Interplay of tumor vascular oxygenation and tumor pO₂ observed using near-infrared spectroscopy, an oxygen needle electrode, and ¹⁹F MR pO₂ mapping," *J. Biomed. Opt.*, **8**(1), 53-62, 2003.
13. M. Cope, "The application of near infrared spectroscopy to non invasive monitoring of cerebral oxygenation in the newborn infant", PhD thesis, University College London, 1991.
14. D. B. S., Hoon, "Circulating immune complexes in rats bearing 6-thioguanine-resistant variants of the 13762 mammary adenocarcinoma," *Cancer Res.*, **44**, 2406-2409 (1984).
15. P. Calabresi, B. A. Chabner, "Antineoplastic agents", In: A.F. Gilman, T. W. Rall, A.S. Niss, and P. Taylor (Editors), *The Pharmacological Basis of Therapeutics*, 8th ed. MacGraw-Hill, Singapore. (1992)
16. R. J. Gillies, P. A. Schornack, T. W. Secomb, and N. Raghunand, "Causes and effects of heterogeneous perfusion in tumors," *Neoplasia*, **1** (3), 197-207, 1999.

-
- 17 D. R. Tailor, H. Poptani, J. D. Glickson, J. S. Leigh, and R. Reddy, "High-Resolution Assessment of Blood Flow in Murine RIF-1 Tumors by Monitoring Uptake of $H_2^{17}O$ With Proton $T_1\rho$ -Weighted Imaging," *Magn. Reson. Med.*, **49**, 1-6, 2003.
- 18 R. P. Mason, A. Constantinescu, S. Hunjan, D. Le, E. W. Hahn, P. P. Antich, C. Blum, and P. Peschke, "Regional tumor oxygenation and measurement of dynamic changes," *Radiat. Res.*, **152**, 239-249, 1999.
- 19 D. Zhao, A. Constantinescu, E. W. Hahn and R. P. Mason. "Tumor oxygenation dynamics with respect to growth and respiratory challenge: Investigation of the Dunning prostate R3327-HI tumor," *Radiat. Res.*, **156**(5), 510-520, 2001.
- 20 S. Hunjan, D. Zhao, A. Constantinescu, E. W. Hahn, P. Antich, and R. P. Mason, "Tumor oximetry: demonstration of an enhanced dynamic mapping procedure using fluorine-19 echo planar magnetic resonance imaging in the dunning prostate R3327-AT1 rat tumor," *Int. J. Radiat. Oncol. Biol. Phys.*, **49**, 1097-1108, 2001.
- 21 M. Höckel, P. Vaupel, "Tumor hypoxia: definitions and current clinical, biologic, and molecular aspects", *J Natl Cancer Inst.*, **93**, 266-76, 2001.
- 22 R. Wenzel, H. Obrig, J. Ruben, K. Villringer, A. Thiel, J. Bernarding, U. Dirnagl, and A. Villringer, "Cerebral blood oxygenation changes induced by visual stimulation in humans", *J. Biomed. Opt.*, **1**(4), 399-404, 1996.
- 23 H. D. Sostman, S. Rockwell, A. L. Sylvia, D. Madwed, G. Cofer, H. C. Charles, R. Negro-Vilar, and D. Moore, "Evaluation of BA1112 rhabdomyosarcoma oxygenation with microelectrodes, optical spectrophotometry, radiosensitivity, and magnetic resonance spectroscopy", *Magn. Reson. Med.*, **20**, 253-267, 1991.

List of Appendices

1. **Jae G. Kim**, Hanli Liu, "Investigation of Breast Tumor Hemodynamics: Dynamic Phantoms and FEM Simulations", in preparation and will be submitted to applied optics.
2. **Jae G. Kim**, Anca Constantinescu, Ralph P. Mason, Hanli Liu, "Non-Uniform Tumor Vascular Oxygen Dynamics Monitored by Multi-Channel Near-Infrared Spectroscopy, in preparation and will be submitted to J. Biomedical Optics.
3. Yueqing Gu, Vincent A. Bourke, **Jae G. Kim**, Anca Constantinescu, Ralph P. Mason, Hanli Liu, "Dynamic response of breast tumor oxygenation to hyperoxic respiratory challenge monitored with three oxygen-sensitive parameters", *Applied Optics*, 42(16), 2960-2967 (2003)
4. Hanli Liu, Yueqing Gu, **Jae G. Kim**, Ralph P. Mason, "Near infrared spectroscopy and imaging of tumor vascular oxygenation", Imaging in Biological Research, Part B (P. Machael Conn ed.) *Methods in Enzymology*, 386, pp. 349-378 (2004)
5. **Jae G. Kim**, and Hanli Liu, "Investigation of breast tumor hemodynamics using tumor vascular phantoms and FEM simulations", in Biomedical Topical Meetings on CD-ROM (The Optical Society of America, Washington, DC, 2004), WF16.

** Appendices 3 and 4 were submitted to be published before PI got a notice of grant approval from DOD so that they do not address PI's grant number in the acknowledgement.

Investigation of Breast Tumor Hemodynamics: Dynamic Phantoms and FEM Simulations

Jae G. Kim, Hanli Liu *

Joint Graduate Program in Biomedical Engineering,
University of Texas Southwestern Medical Center at Dallas/ University of Texas at Arlington
Arlington, TX 76019

Abbreviated Title: Investigation of Tumor Hemodynamics: Dynamic Phantoms and FEM simulations

Correspondence;

Name: Hanli Liu

Address: Joint Program in Biomedical Engineering, P.O. Box 19138, University of Texas at Arlington, Arlington, TX, USA 76019-0167

Phone: 1-817-272-2054

Fax: 1-817-272-2251

Email: hanli@uta.edu

ABSTRACT

In a previous study, switching gas from air to carbogen caused a sharp increase of oxyhemoglobin concentration in breast tumors followed by a further gradual, but significant, increase. This bi-phasic behavior of tumor vascular oxygenation was fitted using a mathematical model based on the hypothesis that the measured signal results from both well-perfused and poorly perfused region in tumor. To prove our hypothesis, we have designed and fabricated a breast tumor dynamic phantom in order to perform three channel experiments with the multi-channel NIR system. Tumor dynamic phantoms are made of gel that encapsulated transparent tubing through which dye flow rates were controlled via two syringe pumps. Tumor phantom experiments showed that two time constants in tumor hemodynamics are indeed from two different perfusion rates. We also conducted computer simulations to further support our tumor phantom measurements and to understand the effects of tumor heterogeneity on the multi-channel NIR readings using a finite element method. (FEM) The FEM simulation results were well matched with the results from tumor phantom experiments and thus these two methods proved our hypothesis. This study demonstrates that by having an appropriate model, we can monitor the therapeutic effects of cancer treatments using non-invasive NIRS and it may have prognostic value, providing insight into tumor vascular development and angiogenesis.

Key Terms: Tumor vascular oxygenation, Finite element method, NIR Spectroscopy, Tumor phantom, Carbogen

INTRODUCTION

Solid tumors develop regions of hypoxia during their growth due to an imbalance between the rate of tumor cell proliferation and branching of the blood vessels.^{1,2,3} Tumor hypoxia can contribute to the failure of radiotherapy,⁴ some forms of chemotherapy,⁵ and photodynamic therapy.⁶ In addition, a number of clinical trials have found that patient survival measured either as tumor regression or as local control depends highly on tumor oxygenation.⁷ Therefore, increasing tumor oxygenation could improve cancer therapy. As one means to improve tumor oxygenation, breathing hyperoxic gas has been used to enhance treatment efficacy. However, poor tumor perfusion may prohibit the oxygen delivery from blood vessels to tumor tissue cells. Therefore, measurements of local vascular oxygenation and distribution of tumor perfusion could be important for tumor treatment planning and to assess methods designed to modulate tumor oxygenation.

Solid tumors are also known to exhibit heterogeneous blood flow distribution.^{8,9} There are various methods to study tumor perfusion heterogeneity, such as Doppler ultrasound,¹⁰ dynamic contrast MRI,¹¹ and the use of tumors grown in window chambers.¹² Intensive studies from Mason's group using ¹⁹F MR [*FREDOM* (Fluorocarbon Relaxometry using Echo planar imaging for Dynamic Oxygen Mapping)] have revealed intratumoral heterogeneity of pO₂ distribution and also heterogeneous response to hyperoxic gas breathing.^{13, 14, 15} The findings of severe pO₂ heterogeneity in tumors suggest the heterogeneous distribution of blood flow, since tissue pO₂ level is determined by a balance between the supply of oxygen from blood vessels and the oxygen consumption rate of tissue cells.¹⁶ Unlike *FREDOM*, near-infrared spectroscopy (NIRS) techniques measure hemoglobin saturation and concentration *in vivo*, providing information on vascular oxygenation of the measured sample/organ. NIRS has been widely applied to investigate hemoglobin oxygenations of muscles,^{17,18,19} the brain,^{20,21,22} and animal tumors.^{23,24,25}

Our previous *in vivo* animal study has clearly demonstrated that carbogen (95% CO₂ and 5% O₂) inhalation can improve the vascular oxygen level of breast tumor. The observed changes in tumor vascular oxygenation exhibited a rapid increase, followed by a gradual but significant increase, in

response to carbogen intervention. (Figure 1) To explain these biphasic behavior of tumor hemodynamics, we established a mathematical model based on the Kety's approach²⁶ and we formed a hypothesis that tumor vasculature is comprised with a well-perfused and poorly perfused region to explain why there are two different time constants in the $\Delta[\text{HbO}_2]$ data. The model further allows us to associate the signal amplitudes to the ratio of vascular coefficients and the ratio of the perfusion rates in the two different regions.

Even though we associated our fitting parameters with physiological factors such as vascular coefficients and perfusion rates mathematically, it was not proved at that time. To provide actual support for this model and to further investigate heterogeneity of breast tumor vasculature, we designed and developed a breast tumor hemodynamic phantom in order to perform three channel experiments with the multi-channel NIRS system. To further support our tumor hemodynamic phantom study, we used FEMLAB software to simulate the dynamic process of light distribution as well as the NIR measurement in breast tumors.

MATERIALS AND METHODS

Mathematical Model of Tumor Vascular Oxygenation

In our previous report,²⁵ we followed an approach used to measure regional cerebral blood flow (rCBF) with diffusible radiotracers, as originally developed by Kety²⁶ in the 1950's. By applying Fick's principle and defining γ as the ratio of HbO_2 concentration change in the vascular bed to that in veins, we arrived at Eq. (1):

$$\Delta\text{HbO}_2^{\text{vasculature}}(t) = \gamma\text{H}_0[1-\exp(-ft/\gamma)] = A[1-\exp(-t/\tau)] \quad (1)$$

where γ is the vasculature coefficient of the tumor ($=\Delta[\text{HbO}_2]^{\text{vasculature}}/\Delta[\text{HbO}_2]^{\text{vein}}$), H_o is the arterial oxygenation input and f is the blood perfusion rate.

If a tumor has two distinct perfusion regions and the measured signal results from both regions (Figure 2), then it is reasonable to include two different blood perfusion rates, f_1 and f_2 , and two different vasculature coefficients, γ_1 and γ_2 , in the model. Therefore, Eq. (1) can be modified to count for the double exponential feature observed in the experiments:

$$\begin{aligned}\Delta\text{HbO}_2^{\text{vasculature}}(t) &= \gamma_1 H_o [1 - \exp(-f_1 t / \gamma_1)] + \gamma_2 H_o [1 - \exp(-f_2 t / \gamma_2)] \\ &= A_1 [1 - \exp(-t / \tau_1)] + A_2 [1 - \exp(-t / \tau_2)]\end{aligned}\quad (2)$$

where f_1 and γ_1 are the blood perfusion rate and the vasculature coefficient in region 1 for the well perfused region, respectively; f_2 and γ_2 have the same respective meanings in region 2 for the poorly perfused region, and $A_1 = \gamma_1 H_o$, $A_2 = \gamma_2 H_o$, $\tau_1 = \gamma_1 / f_1$, $\tau_2 = \gamma_2 / f_2$. Then, if A_1 , A_2 , τ_1 , and τ_2 are determined by fitting the measurements with the model, we can obtain the ratios of two vasculature coefficients and the two blood perfusion rates:

$$\frac{\gamma_1}{\gamma_2} = \frac{A_1}{A_2}, \quad \frac{f_1}{f_2} = \frac{A_1 / A_2}{\tau_1 / \tau_2}. \quad (3)$$

With these two ratios, we are able to understand more about tumor physiology, such as tumor vasculature structure and blood perfusion. In this report, we used three-channel NIR spectroscopy to evaluate our tumor hemodynamics model by quantifying A , τ , γ_1/γ_2 and f_1/f_2 at three different locations on the tumor phantoms.

Tumor Hemodynamic Phantom Design and Measurements

To represent vascular blood vessels in tumor, we designed a vascular modeling device (VMD) by winding a small diameter tube around a big diameter core tube. An example of such a VMD is shown in Figure 3. VMD-1 was fabricated by wrapping ethyl vinyl acetate microbore tubing (0.51 mm ID) around tygon lab tubing (14.4 mm OD), and VMD-2 was fabricated by winding tygon silicone tubing (0.80 mm ID) around tygon lab tubing (14.4 mm OD) to represent small diameter blood vessel and large diameter blood vessel, respectively. All tubing materials were purchased from Cole-Parmer Company (Vernon Hills, IL).

Tumor dynamic phantom was fabricated by embedding two VMDs into a cylinder shape of gel, which represents tissues. Tissue mimic gel was made by mixing 50 g of gel powder (Sigma, Gelatin Type A, St. Louis, MO) into 350 ml of boiling water, and solution was stirred thoroughly until gel powder was dissolved completely. When the solution was cooled down to around 50 °C, 200 ml of intralipid (Intralipid® 20%, Baxter Healthcare Corp., Deerfield, IL) was added and mixed thoroughly to simulate light scattering in tumor tissues. Just before solution started to be solidified, it was poured into a cylindrical container (diameter=4.5 cm, height=3.5 cm), which contained two VMDs inside. After completely being cooled down, the solution became a soft gelatin phantom with the two VMDs embedded inside. The optical properties of tumor gel phantom were measured using near infrared tissue spectrometer (model:96208, ISS Inc., Champaign, IL) and those values were close to tissue optical properties ($\mu_a = 0.032 \text{ cm}^{-1}$, $\mu_s' = 9.2 \text{ cm}^{-1}$ at 750 nm).

For our experiments, two tumor hemodynamic phantoms were fabricated. Phantom 1 contained one VMD-1 and one VMD-2 while two VMD-1s were embedded into a cylindrical gel for phantom 2. A stream of dye solution (diluted black ink, $\mu_a = 1.5 \text{ cm}^{-1}$ at 730 nm) was used to go through the VMDs to simulate a blood flow through tumor vasculature. By applying same dye flow rate into VMD-1 and VMD-2 in phantom 1, we would see the effects of blood vessel length or diameter on bi-phasic behavior of tumor blood oxygenation during carbogen inhalation. Meanwhile, injecting dye into two VMD-1s in

phantom 2 with different flow rates would enable us to find how blood flow rate affects tumor's bi-phasic increase of oxyhemoglobin during carbogen inhalation. In this way, we could mimic a hemodynamic process of a breast tumor by changing the diameter or the length of the small tube or by controlling the flow rate of the dye solution.

Schematic experimental setup for tumor hemodynamic phantom study is shown in Figure 4a. As shown here, NIR light (730 nm) from multi channel NIRS was delivered to the tumor hemodynamic phantom, and three optical detectors placed on the side of cylindrical phantom collected signals, which would be processed in the computer. Dye was injected into VMDs using B-D™ disposable syringe (Cole-Parmer, Vernon Hills, IL) by two syringe pumps (model KDS200, KdScientific Inc., New Hope, PA), and dye wastes were collected in the waste beaker. We used two syringe pumps so that we could control dye flow rate for each VMD. Figure 4b shows more detail setup of light source and three optical detectors around the tumor phantom. Light source was placed between two VMDs, and detector D3 was located across the light source in the transmission mode so that it would detect signal passing through both VMDs. Other two detectors (D1 and D2) were placed in the reflectance geometry with respect to light source so that D1 and D2 would get the NIR signals mostly from only one of two VMDs.

Experimental procedures are as follows. For the tumor phantom 1, VMD-1 and VMD-2 were filled with water first as a baseline, and then dye was injected into the VMD-2 first with a flow rate of 20 ml hr⁻¹ to simulate the light absorption effect of blood, followed by a washout with water. For the second step, dye was injected into the VMD-1 with the same flow rate as that in the first step and also followed by a washout of water. The last step was introducing dye into both VMD-1 and VMD-2 with the same flow rate of 20 ml hr⁻¹. By flowing dye into a tumor phantom 1 in this way, we expected to see two exponential increases of light absorption changes because dye flow velocities will be different between VMD-1 and VMD-2 due to different sizes of tube diameter even though the applied dye flow rate was same for both VMDs.

For the tumor phantom 2, we first filled two VMD-1s with water and then dye was injected into the top VMD-1 with a flow rate of 20 ml hr⁻¹ followed by a washout with water. In the second step, dye

was injected into the bottom VMD-1 with a 20 ml hr⁻¹ flow rate and was washed out with water again. Thirdly, we introduced dye into both VMD-1s with a same flow rate of 20 ml hr⁻¹ following washout water. Finally, dye was injected into two VMD-1s with two different flow rates (5 and 20 ml hr⁻¹ for top and bottom VMD-1, respectively) and was washed out with water. Changes of light absorption were measured through the whole experiment, and the time constants for the dynamic changes in light absorption were obtained by fitting the data with our mathematical models using Kaleidagraph software (Synergy Software, Reading, PA).

FEM Simulation

To further support our tumor hemodynamic phantom study, we used FEMLAB software (COMSOL Inc. Burlington, MA), which is based on the finite element method, to simulate our tumor phantom 2 experiment. It uses numerical approaches to solve partial differential equations (PDE) in modeling and simulating various engineering problems. The geometry of FEM simulation for tumor hemodynamic phantom is shown in the figure 5 and it represents a 2 dimensional horizontal cross section of our phantom 2. E1 represents the body of tumor phantom (diameter = 4 cm), and R5 shows the location of the light source. Furthermore, each tube used in the dynamic phantom is represented by two rectangles (0.1 x 2.4 cm rectangle) as a blood vessel network: R1 and R2 are representing vessels with a fast flow rate, and R3 and R4 denote vessels with a slow flow rate.

Equation 4 is the diffusion equation that has been applied to predict photon distribution in phantom as dye flows through two VMDs.

$$(1/c)(\partial/\partial t)\phi(r,t) - D\nabla^2\phi(r,t) + \mu_a\phi(r,t) = S(r,t) \quad (4)$$

where $\phi(r,t)$ is the diffuse photon fluence rate at the position r , c is the speed of light in the tissue, $S(r,t)$ describes the photon source, and $D = [3(\mu_a + \mu_s')]^{-1}$ is the photon diffusion coefficient.

For the boundary conditions, the partial current boundary condition was applied to FEM model as shown below. (Eq. 5)

$$\phi(r, z = 0, t) - 2AD(\partial / \partial z)\phi(r, z, t)\big|_{z=0} = 0 \quad (5)$$

with

$$A = (1 + r_d) / (1 - r_d) \quad (6)$$

where r_d is the internal reflectance, due to refractive index mismatch between the air and the tissue. This can be estimated using the following empirically determined equation.

$$r_d = -1.440n^{-2} + 0.710n^{-1} + 0.668 + 0.0636n \quad (7)$$

with

$$n = n_{tissue} / n_{air} \quad (8)$$

We used 1.4 and 1.0 as values for n_{tissue} and n_{air} , respectively, and then we could get 3.25 as a value for A . We also used 0.033 cm as a diffusion coefficient of phantom since it gives reduced scattering coefficient, 10 cm^{-1} , of the regular tissue, and 0.03 and 1.5 cm^{-1} were used as absorption coefficients for phantom and

dye in VMDs, respectively. The simulation model was then meshed in the mesh mode resulted in 1147 elements and 609 nodes. Finally, it is solved using the stationary nonlinear solver type.

Two different flow rates in tumor phantom study were simulated by lengthening the heights of R1, R2, and R3, R4 with different frame rates. In other words, a fast flow rate was simulated by increasing the heights of R1 and R2 with a large increment per frame (e.g., 0 to 2.4 cm with 0.6 cm increment per frame), and a slow flow rate was simulated by increasing heights of R3 and R4 with small increment per frame (0 to 2.4 cm with 0.02 cm increment per frame). Therefore, there existed a 20 times difference in flow rate between two VMDs.

We also changed a position of source light to see the effect of vessel/VMD geometry on bi-phasic feature of the tumor hemodynamic measurements. We changed the position of light source to the right side of the phantom (Fig. 10a) and to the center of the phantom (Fig. 10b). In the geometry of Fig. 10a, the light penetrates the slow-flow VMD first and then the fast-flow VMD. This simulation was done to find whether in this geometry, the light signal changes still have the double exponential behavior. In other words, we wish to investigate whether the bi-phasic hemodynamic feature depends on the orientations of the vessels/VMD networks.

Multi-Channel NIR Spectroscopy

Our multi-channel continuous wave NIR spectroscopy system has one light source and eight detectors, but due to the finite tumor dynamic phantom size and for the simplicity of this initial experiment, we used only three detectors to monitor light absorption changes in tumor phantoms during tumor phantom experiments. Based on the modified Beer-Lambert's law, the data presented in this paper were analyzed using amplitude values to find the changes in absorption (Eq. 9).

$$\Delta\mu_a = \mu_{aB} - \mu_{aT} = \log(A_B/A_T) / L, \quad (9)$$

where L is the optical path length, and A_B and A_T are baseline and transient amplitudes of the measured optical signals, respectively.

RESULTS

Tumor Dynamic Phantom Study

Figure 6a shows the absorption changes ($\Delta\mu_a$, wavelength=730nm) of tumor phantom at three different positions when dye was injected into VMDs. The first step for this experiment was injecting dye into only VMD-2, which has large diameter tubing with a 20 ml/hr flow rate. As we can see from the result, the reading from D1 showed largest increase of $\Delta\mu_a$, and D2 showed smallest increase of $\Delta\mu_a$ since at the position of D1, it would detect optical signal changes mostly from the VMD-2. The $\Delta\mu_a$ increase of D3 was between those from D1 and D2, as we expected. A similar pattern is also shown at step 2 where there was a dye flow (20 ml/hr) only into VMD-1, which has small diameter tubing. At this step, D2 had a largest increase of $\Delta\mu_a$ and D1 showed smallest $\Delta\mu_a$ increase with the same reason that was mentioned above. Step 1 and 2 clearly showed us that the D1 and D2 are placed on the tumor phantom properly for this experiment as we designed, and clearly demonstrates that signal from heterogeneity can be detected stronger if it is near the detector. The third step in the measurement was to inject dye into both VMD-1 and VMD-2 simultaneously with a same flow rate as before (20 ml/hr). At this step, we can observe two features: 1) the time profile taken at D2 has a faster transition time than that at D1, and 2) the time profile taken at D3 has a bi-exponential characteristic, which is very similar to those we often observed in our breast tumor dynamic measurements.²⁵

To understand these phantom measurements, let us consider the velocities at each tube. Even though the flow rate was the same for both of the tubes, the velocities of the ink solutions in the two VMDs networks were different due to the different diameters. The solution in the small diameter tube had a velocity 2.74 times faster than that of the large diameter tube, based on the following relationship:

$$\frac{v_{VMD-1}}{v_{VMD-2}} = \frac{r_{VMD-2}^2}{r_{VMD-1}^2} = \frac{0.4^2}{0.255^2} = 2.46 \quad (10)$$

where v_{VMD-1} , and v_{VMD-2} are velocities of the ink solution in the VMD-1 (small diameter tubing) and VMD-2 (large diameter tubing), respectively, and r_{VMD-1} , and r_{VMD-2} present the radii of the VMD-1 and VMD-2, respectively. This velocity difference may be the reason why the transition time is faster in the VMD-1 than that in the VMD-2. When we increased the flow rate of large diameter tube, we could not see the two exponential behaviors from D3. Furthermore, since D3 was in the transmission geometry and was located near both of the VMDs, the signal obtained at D3 should reflect the dynamic changes occurred in both of the VMDs. We expect that the bi-exponential feature recorded by D3 results from a superposition between the two different dynamic transitions at the VMD-1 and VMD-2.

For the further analysis, $\Delta\mu_a$ increases detected from three detectors at step 3 in Figure 6a was fitted by using our mathematical models to obtain amplitudes and time constants values. (Figure 6b) The fitting values for each curve are shown in the table 1. This result shows that when dye flows into both VMD-1 and VMD-2, fast time constant ($\tau_1=11.71 \pm 3.49$) and slow time constant ($\tau_2=35.17 \pm 7.25$) from D3 are very close to $\tau_1 (=7.3 \pm 0.25)$ at D2 (VMD-1) and $\tau_1 (=42.8 \pm 1.53)$ at D1 (VMD-2), respectively. This indeed shows that two exponential behaviors of tumor blood oxygenation during carbogen inhalation can be from two different blood vessels diameters in tumors.

The phantom 1 data presented here basically demonstrate that we can experimentally mimic the bi-exponential behavior with two different velocities, or perfusion rates, from two different diameter VMDs. This knowledge may help us understand the bi-phasic features observed in the breast tumor vascular oxygenation measurements under carbogen inhalation. Furthermore, the next phantom 2 experimental results demonstrate that the bi-exponential dynamics may also result from different flow rates, given the same diameters for the two VMDs.

Figure 7a shows the experimental results from tumor phantom 2, and this phantom is different from tumor phantom 1 by having two VMD-1s instead of one VMD-1 and one VMD-2 in tumor phantom

1. Since we now have two VMD-1s, the velocities of dye in VMDs will be totally depending on the dye flow rates controlled by two syringe pumps. The source and detector positions were same as Figure 6a, which is shown in the Figure 4b, and we observed the results similar to those shown in Figure 6a by alternating flow rates.

The first step for this experiment was injecting dye only into bottom VMD-1 with a flow rate of 20 ml/hr. As a result, D2 showed largest increase of $\Delta\mu_a$ while D1 showed smallest increase of $\Delta\mu_a$ because D1 was located quite away from the bottom VMD-1. For the second step, top VMD-1 was injected with dye at the same flow rate of 20 ml/hr. Here, D1 showed largest increase of $\Delta\mu_a$ and D2 showed smallest increase of $\Delta\mu_a$. In both of the above cases, the signals from D3 showed similar profiles as the others, without clear bi-exponential patterns. Then, as the third step, dye was injected into both top and bottom VMD-1s with the same flow rate (20 ml/hr). Similarly, we did not observe any clear features of the two-exponential increase of $\Delta\mu_a$. For the fourth step, we injected dye into both VMD-1s, but with two different flow rates: 5 ml/hr for top VMD-1 and 20 ml/hr for the bottom VMD-1. Now we can see bi-exponential behavior appears on D3 since D3 is detecting signals from both top and bottom VMD-1s, which have two different dye flow rates.

Once again, time constant analysis was performed for the increase of $\Delta\mu_a$ from three detectors at step 4 in Fig. 7a and is shown in Fig. 7b. This time constant analysis shows that $\Delta\mu_a$ increases from D1 and D2 are well fitted by mono exponential model while $\Delta\mu_a$ increases from D3 is fitted well with double exponential models. As we can see from the table 2, which the values of fitted parameters are summarized, fast time constant ($\tau_1 = 18.13 \pm 0.87$) and slow time constant ($\tau_2 = 133.66 \pm 11.36$) from D3 are well matched with τ_1 in D2 (20.92 ± 0.53) and τ_1 in D1 (131.19 ± 3.46). This suggests that the dynamic signals obtained from D3 with a fast and slow component indeed result from the dynamic changes in both of the VMD-1s.

FEM Simulation

Figure 8 shows an example of the FEM tumor phantom simulation to further support our tumor phantom 2 experiment. Figure 8a is the light distribution of dynamic phantom where there was dye injection into only R1 and R2 (bottom VMD-1 in Fig. 7a) with a fast flow rate and Fig. 8b is the simulation when dye flowed only into R3 and R4 (top VMD-1 in Fig. 7a) with a slow flow rate. Finally, Figure 8c shows how light distributes in a tumor dynamic phantom when dye was injected into both VMD-1s with two different flow rates. As we mentioned earlier at materials and methods section, different flow rate was mimicked by increasing the length of light absorbing object (R1, R2, R3 and R4) with the different frame rates. Figure 8a is the result of simulation at 6th frame while Fig. 8b is the simulated result at 120th frame. This implies that R1 and R2 have 20 times faster flow rate than that in R3 and R4. Figure 8c is also the result of simulation at 120th frame when dye flows in both VMD-1s.

For comparison with the results from phantom experiments, we extracted light intensity values at three positions (2,0), (-2,0), and (0,2) from each frame of simulations to calculate $\Delta\mu_a$, which are shown in the figure 9. These three positions, (2,0), (-2,0), and (0,2), are corresponding to D1, D2 and D3 in Fig. 7a, and time in these plots were obtained by multiplying 2 seconds to each frame. Therefore, Fig. 8a will have 12 seconds to reach the maximum $\Delta\mu_a$ since it has only 6 frames to simulate fast flow, and Fig. 8b and 8c will have 240 seconds to have a maximum absorption because they have 120 frames of slow flow simulation.

Figure 9a and 9b show $\Delta\mu_a$ from three positions of phantom in fast flow only simulation and slow flow only simulation, respectively. Figure 9a shows the $\Delta\mu_a$ is largest in (-2,0) position and smallest in (2,0) position when there is a dye flow only into fast flow VMD-1, and this result is matching with the results from Fig. 6a and 7a. The similar results could be obtained when dye flowed only into slow VMD-1 as we can see from the Fig. 9b. Figure 9c shows $\Delta\mu_a$ from three positions in Figure 8c, and the $\Delta\mu_a$ at (0,2) position shows bi-phasic behavior as we could see from animal tumors and our tumor dynamic

phantoms. This indeed supports that it is necessary to have a different flow rate for tumor to have bi-phasic blood oxygenation dynamics during carbogen inhalations.

We also changed the position of source light to the right side of the phantom (Fig. 10a) and center of the phantom (Fig. 10b) to see how blood vessel/VMD geometry in tumor/phantom affects the bi-phasic feature of the tumor hemodynamics during carbogen inhalation. As described in Figure 5, R1 and R2 represent the fast flow VMD while R3 and R4 represent the slow flow VMD. Light intensity values at several positions were also extracted to calculate $\Delta\mu_a$ and were plotted in Figure 11a and 11b. Figure 11a shows that (0,-2) and (0,2) positions detect little signals from fast flow VMD since both positions will mostly detect light from the slow flow VMD with this geometry. However, this geometry allows (-2,0) position can detect signals from both slow and fast flow VMDs so that we can see bi-phasic behavior from (-2,0) position. Figure 11b also plotted the $\Delta\mu_a$ obtained from four positions on tumor phantom simulation (Fig. 10b) and showed that (-2,0) and (2,0) positions were getting signals mostly from only fast flow and slow flow VMD, respectively. However, (0,2) and (0,-2) positions were showing bi-phasic behavior because they were detecting light signals from both fast flow and slow flow VMDs. All of these results prove that there will be bi-phasic features of tumor hemodynamics as long as two different perfusion rates exist in tumors regardless of vessel geometry.

DISCUSSION

Both tumor dynamic phantom experiments and FEM simulation results supported our hypothesis that the bi-phasic tumor hemodynamic feature results from a well-perfused and poorly perfused region in the tumor vasculature under carbogen inhalation. Through our phantom study, we were able to find that main cause for having a bi-phasic behavior is coming from different blood flow rate, more precisely from different blood velocity in tumor. These differences in velocity can be from different blood vessel diameters with same blood flow rate or from different blood flow rate with same vessel diameter, which tumor vasculatures have both. Tumor blood vessels are known to be very leaky, longer in vessel lengths,

larger in vessel diameter, and also their local microvessel density is much more heterogeneous compare to normal tissues.⁸ In addition, solid tumors usually develop hypoxia, which can be from poor perfusion in the central region when they grow bigger. Meanwhile, the peripheral region of tumor is normally well perfused so that it can be well provided with nutrition and oxygen. Therefore, tumor vasculature can be a mixed structure between well-perfused region and poorly perfused region, which can be observed as a bi-phasic feature of hemodynamics with respiratory challenges. Therefore, the multi-channel NIRS system will allow us to study the dynamic heterogeneity at different locations, showing that the tumor vasculature in the poorly perfused region (with a lower perfusion rate) can be eventually oxygenated if the two dynamic components are observed. On the other hand, if only the fast component exists, it suggests that the poorly perfused region in the tumor may not have much chance to be improved for its vascular oxygenation under carbogen intervention.

FEM simulation results strongly supported our tumor dynamic phantom experimental data and showed that the bi-phasic behavior always existed regardless of geometry of light source and VMDs in phantom as long as a detector is located somewhere it can collect signals from both fast flow and slow flow VMDs. To compare the results from tumor phantom experiments with FEM simulation results, we divided $\Delta\mu_a$ by maximum value of $\Delta\mu_a$ from each detector for normalization. (Figure 12a and 12b) Figure 12a is a normalized plot of step 4 in Fig. 7a (tumor phantom experiment) and Fig. 12b is another normalized plot of Fig. 9c. (FEM simulation) These figures show how much FEM simulation results are close to tumor phantom experiments. Both of them show that $\Delta\mu_a$ increases from D3 and (0,2) position will be well fitted by using a double exponential model. The early time of $\Delta\mu_a$ increases from D3 and (0,2) position (inside the circle) have larger $\Delta\mu_a$ s than D2, D1, (-2,0) and (2,0), which can be explained by locations of detectors. Since the dye flow started from D3 or (0,2) side, both D3 and (0,2) position could detect $\Delta\mu_a$ changes earlier and also larger than those from the other detectors (D1, D2, (2,0), and (-2,0)), which were located a little far from the dye flow starting position. These results indeed show that FEM

simulation can well explain the results from tumor phantom experiments by using light diffusion equation.

As we described in materials and methods section earlier, γ_1/γ_2 may be associated with vascular volume or density of two regions, and f_1/f_2 is related to the ratio of blood perfusion rates between region 1 and 2. Our tumor phantom experiments and FEM simulation of tumor dynamic phantom showed that A or γ values are related with absorption changes of VMDs in tumor phantoms, and τ or f are related to the velocity of dye flow. The intensity of absorption changes that measured from detectors depends on the absorption coefficient of dye, the tube length or diameter in VMD, wrapping number of small tubing around big tubing, and location of detectors. Time constant and perfusion rate are mainly depending on dye flow rate, but it can be also affected by diameter and length of tube in VMD. In tumor's case, μ_a of dye corresponds to the level of blood oxygenation, and tube length or diameter can be thought as those of blood vessel. The number of winding small tubing around big tubing can be thought as a vascular density in tumor, which will affect the values of both γ and f .

Our previous measurements of animal tumors were performed in a transmittance mode by one channel NIRS, which could obtain only global measurements of tumor hemodynamics. Therefore, those results could not show intratumoral or intertumoral vascular heterogeneities. However, multi-channel NIRS, by comparing γ_1/γ_2 and f_1/f_2 among the signals taken at different locations from the same tumor or from different tumors, will enable us to study intratumoral or intertumoral heterogeneity. Since tumor vascular structure will be modified during therapies, we will be able to observe the changes of γ_1/γ_2 and f_1/f_2 through time by giving respiratory challenges such as carbogen or pure oxygen inhalation. Therefore, multi-channel NIRS or imaging not only can detect vascular heterogeneity of tumor but also can be a prognostic tool for monitoring the early effects of tumor treatments such as radiotherapy, photodynamic therapy, or chemotherapy. The detection of early effects of cancer therapies will benefit patients to have a higher survival rate by treating the patients with proper therapies.

CONCLUSION

We developed tumor phantom models to demonstrate our hypothesis on tumor hemodynamics during carbogen inhalation. We believe that bi-phasic feature of tumor blood oxygenation increases during carbogen inhalation is from tumors' distinct vascular structure, which is composed of well-perfused region and poorly perfused region. Our tumor phantom experiments were performed to find what can cause tumor hemodynamics to have two time constants when it is fitted with our mathematical model. We found that two time constants in tumor hemodynamic models can be from different blood flow velocities or anything that can cause changes in blood flow velocities such as blood vessel diameter, and length. In addition, we also found that two different amplitudes in tumor hemodynamic models are from differences in absorption in two region, which are possibly due to different blood oxygenation level (oxyhemoglobin concentration), or vascular density. FEM simulation using a light diffusion equation was performed to simulate our tumor phantom experiments. These simulated results were well matched with our tumor phantom experiments, which indeed supported our hypothesis.

NIRS is a portable, low cost, and real time measurement system that can monitor changes of vascular oxygen levels by using two wavelengths. We have previously used a single-channel NIRS system with one light source and one detector for global measurements of $\Delta[\text{HbO}_2]$ and $\Delta[\text{Hb}_{\text{total}}]$ in tumors during respiratory challenges.²⁵ Now, this study demonstrates that the NIRS multi-channel approach has the great potential to detect and monitor tumor heterogeneity under therapeutic or adjuvant interventions. In the future we propose 1) to further investigate and understand the meaning of vasculature coefficient, γ , and 2) to develop an NIR imaging system to image tumor oxygenation heterogeneities under various interventions used to improve the efficacy of cancer treatments.

ACKNOWLEDGEMENTS

This work was supported by the Department of Defense Breast Cancer Initiative grants DAMD17-03-1-0353 (JGK) and BC990287 (HL). The authors acknowledge the support of the multi-channel NIRS system from Dr. Britton Chance at the University of Pennsylvania, Philadelphia. We also thank to Dr. Kevin Nelson and Brent Crow for the support of syringe pumps and Gowri Srinivas for her help in FEM simulations.

Table 1. Summary of fitted parameters obtained at the three detectors from step 3 in Figure 6a

Parameters	Mono-Exponential fitting $\Delta\text{HbO}_2 = A_1[1-\exp(-t/\tau_1)]$		Double-Exponential fitting $\Delta\text{HbO}_2 = A_1[1-\exp(-t/\tau_1)] + A_2[1-\exp(-t/\tau_2)]$
	Detector D1	Detector D2	Detector D3
A_1 (mM/DPF)	0.49 ± 0.007	0.34 ± 0.001	0.079 ± 0.041
τ_1 (min)	42.8 ± 1.53	7.3 ± 0.25	11.71 ± 3.49
A_2 (mM/DPF)			0.14 ± 0.038
τ_2 (min)			35.17 ± 7.25
χ^2	0.039	0.016	0.0018
R	0.99	0.98	0.99

Table 2. Summary of fitted parameters obtained at the three detectors from step 4 in Figure 7a

Parameters	Mono-Exponential fitting $\Delta\text{HbO}_2 = A_1[1-\exp(-t/\tau_1)]$		Double-Exponential fitting $\Delta\text{HbO}_2 = A_1[1-\exp(-t/\tau_1)] + A_2[1-\exp(-t/\tau_2)]$
	Detector D1	Detector D2	Detector D3
A_1 (mM/DPF)	0.26 ± 0.003	0.17 ± 0.001	0.068 ± 0.0024
τ_1 (min)	131.19 ± 3.46	20.92 ± 0.53	18.13 ± 0.87
A_2 (mM/DPF)			0.047 ± 0.0018
τ_2 (min)			133.66 ± 11.36
χ^2	0.057	0.019	0.0018
R	0.98	0.97	0.99

FIGURE CAPTIONS

Figure 1. Results obtained with the NIR instrument from a 4.5-cm³ rat breast tumor while the breathing gas was switched from 33% O₂ to carbogen. The thicker solid curve represents ΔHbO_2 , the thinner solid curve represents ΔHb_t , and the dashed curve with the filled circles represents arterial saturation. (Liu *et al.* 2000)²⁵

Figure 2. Schematic diagram of light transmitting patterns in tumor when tumor has two distinct perfusion regions. Center of tumor represents poorly perfused region and peripheral region of tumor with gray color is representing a well-perfused region. Since the light transmitting volume is different in each detector, each detector will show the different fitted parameters.

Figure 3. Schematic diagram for one embedded vascular modeling device (VMD): the small tubing wound outside of core tubing simulates blood vessels within a breast tumor.

Figure 4. Experimental setup for the tumor dynamic phantom study. (a) Two syringe pumps were connected to two VMDs in tumor dynamic phantom for controlling dye flow rates. Light was transmitted from light source through tumor phantom and collected at three different detectors for data processing in computer (b) Enlarged tumor dynamic phantom embedded with two VMDs. Tumor phantom 1 has VMD-1 and VMD-2 as shown here and tumor phantom 2 has two VMD-1s.

Figure 5. The geometry for FEM simulations of a tumor dynamic phantom 2. R1 and R2 rectangles represent fast flow VMD while R3 and R4 represent slow flow VMD.

Figure 6. (a) 3-channel NIRS results measured on a tumor dynamic phantom 1 with two size VMDs (VMD-1 and VMD-2). Three traces represent the readings at D3 (in transmission mode and located between the two VMDs), D1 (near the VMD-2), and D2 (near the VMD-1). (b) Temporal profiles of the

NIRS measurements from D1, D2, and D3 with one-exponential fitting (D1, and D2) and bi-exponential fitting (D3).

Figure 7. (a) 3-channel NIRS results measured on a tumor dynamic phantom 2 with two VMD-1s. Three traces represent the readings at D3 (in transmission mode and located between the two VMDs), D1 (near the top VMD-1), and D2 (near the bottom VMD-1). (b) Temporal profiles of the NIRS measurements from D1, D2, and D3 with one-exponential fitting curves (D1, and D2) and bi-exponential fitting curve (D3).

Figure 8. FEM simulations of light distribution inside of a dynamic phantom. (a) The results with a fast simulated flow rate only, (b) the results with a only slow flow rate, and (c) the results with both fast and slow simulated flow rates.

Figure 9. Absorption changes measured at three locations in FEM simulation (Fig. 8) during fast flow only (a), slow flow only (b), and both fast and slow flow (c).

Figure 10. FEM simulations of light distribution inside of a dynamic phantom. (a) The results when the light source is located on (2,0) position, (b) the results when the light source is located in the center of the phantom.

Figure 11. Absorption changes measured at three locations in FEM simulation (Fig. 10a) during both fast and slow flow (a), and $\Delta\mu_a$ measured at four locations in FEM simulation (Fig. 10b) during both fast and slow flow (b).

Figure 12. Normalized $\Delta\mu_a$ plots are shown to compare the results from between tumor dynamic phantom experiment and FEM simulation: (a) Normalized $\Delta\mu_a$ plots of step 4 in Fig. 7a, (b) Normalized $\Delta\mu_a$ plots of Fig. 9c.

REFERENCES

- ¹ P. Vaupel, O. Thews, D. K. Kelleher, and M. Höckel, "Current status of knowledge and critical issues in tumor oxygenation", In: Hudetz and Bruley (eds), *Oxygen Transport to Tissue XX*, 591-602, Plenum Press, New York, 1998.
- ² P. Vaupel, "Vascularization, blood flow, oxygenation, tissue pH, and bioenergetic status of human breast cancer", In: Nemoto and LaManna (eds), *Oxygen Transport to Tissue XVIII*, 243-253, Plenum Press, New York, 1997.
- ³ P. Vaupel, "Oxygen transport in tumors: Characteristics and clinical implications", *Adv. Exp. Med. Biol.*, **388**, 341-351, 1996.
- ⁴ R. H. Thomlinson, and L. H. Gray, "The histological structure of some human lung cancers and the possible implications for radiotherapy", *Br. J. Cancer*, **9**, 539-549, 1955.
- ⁵ B. Teicher, J. Lazo, and A. Sartorelli, "Classification of antineoplastic agents by their selective toxicities toward oxygenated and hypoxic tumor cells", *Cancer Res.*, **41**, 73-81, 1981.
- ⁶ J. D. Chapman, C. C. Stobbe, M. R. Arnfield, R. Santus, J. Lee, and M. S. McPhee, "Oxygen dependency of tumor cell killing *in vitro* by light activated photofrin II", *Radiat. Res.*, **126**, 73-79, 1991.
- ⁷ A. W. Fyles, M. Milosevic, R. Wng, M. C. Kavanagh, M. Pintile, A. Sun, W. Chapman, W. Levin, L. Manchul, T. J. Keane, and R. P. Hill, "Oxygenation predicts radiation response and survival in patients with cervix cancer", *Radiother. Oncol.*, **48**, 149-156, 1998.
- ⁸ R. J. Gillies, P. A. Schornack, T. W. Secomb, and N. Raghunand, "Causes and effects of heterogeneous perfusion in tumors," *Neoplasia*, **1** (3), 197-207, 1999.
- ⁹ D. R. Taylor, H. Poptani, J. D. Glickson, J. S. Leigh, and R. Reddy, "High-Resolution Assessment of Blood Flow in Murine RIF-1 Tumors by Monitoring Uptake of H₂ ¹⁷O With Proton T₁ρ-Weighted Imaging," *Magn. Reson. Med.*, **49**, 1-6, 2003.
- ¹⁰ J. C. Acker, M. W. Dewhirst, G. M. Honore, T. V. Samulski, J. A. Tucker, and J. R. Oleson, "Blood perfusion measurements in human tumors, evaluation of laser Doppler methods," *Int. J. Hypertherm.*, **6**, 287-304, 1990.
- ¹¹ J. Griebel, N. A. Mayr, A. de Vries, M. V. Knopp, T. Gneiting, C. Kremser, M. Essig, H. Hawighorst, P. H. Lukas, and W. T. Yuh, "Assessment of tumor microcirculation: a new role of dynamic contrast MR imaging," *J. Magn. Reson. Imaging*, **7**, 111-119, 1997.
- ¹² M. W. Dewhirst, C. Gustafson, J. F. Gross, and C. Y. Tso, "Temporal effects of 5.0 Gy radiation in healing subcutaneous microvasculature of a dorsal flap window chamber", *Radiat. Res.*, **112**, 581-591, 1987.
- ¹³ R. P. Mason, A. Constantinescu, S. Hunjan, D. Le, E. W. Hahn, P. P. Antich, C. Blum, and P. Peschke, "Regional tumor oxygenation and measurement of dynamic changes." *Radiat. Res.*, **152**, 239-249, 1999.
- ¹⁴ D. Zhao, A. Constantinescu, E. W. Hahn and R. P. Mason. "Tumor oxygenation dynamics with respect to growth and respiratory challenge: Investigation of the Dunning prostate R3327-HI tumor," *Radiat. Res.*, **156**(5), 510-520, 2001.
- ¹⁵ S. Hunjan, D. Zhao, A. Constantinescu, E. W. Hahn, P. Antich, and R. P. Mason, "Tumor oximetry: demonstration of an enhanced dynamic mapping procedure using fluorine-19 echo planar magnetic resonance imaging in the dunning prostate R3327-AT1 rat tumor," *Int. J. Radiat. Oncol. Biol. Phys.*, **49**, 1097-1108, 2001.
- ¹⁶ M. Höckel, P. Vaupel, "Tumor hypoxia: definitions and current clinical, biologic, and molecular aspects", *J Natl Cancer Inst.*, **93**, 266-76, 2001.
- ¹⁷ B. Chance, S. Nioka, J. Kent, K. McCully, M. Fountain, R. Greenfield, and G. Holtom, "Time resolved spectroscopy of hemoglobin and myoglobin in resting and ischemic muscle", *Anal. Biochem.*, **174**, 698-707, 1988.
- ¹⁸ S. Homma, T. Fukunaga, and A. Kagaya, "Influence of adipose tissue thickness on near infrared spectroscopic signals in the measurement of human muscle", *J. Biomed. Opt.*, **1**(4), 418-424, 1996.
- ¹⁹ M. Ferrari, Q. Wei, L. Carraresi, R. A. De Blasi, and G. Zaccanti, "Time-resolved spectroscopy of the human forearm", *J. Photochem. Photobiol. B: Biol.*, **16**, 141-153, 1992.

-
- ²⁰ B. Chance, E. Anday, S. Nioka, S. Zhou, L. Hong, K. Worden, C. Li, T. Murray, Y. Ovetsky, D. Pidikiti, and R. Thomas, "A novel method for fast imaging of brain function non-invasively with light", *Optics Express*, **2**(10), 411-423 1998.
- ²¹ R. Wenzel, H. Obrig, J. Ruben, K. Villringer, A. Thiel, J. Bernarding, U. Dirnagl, and A. Villringer, "Cerebral blood oxygenation changes induced by visual stimulation in humans", *J. Biomed. Opt.*, **1**(4), 399-404, 1996.
- ²² M. Cope, and D. T. Delpy, "A system for long term measurement of cerebral blood and tissue oxygenation in newborn infants by near infrared transillumination", *Med. Biol. Eng. Comp.*, **26**, 289-294, 1988.
- ²³ R. G. Steen, K. Kitagishi, and K. Morgan, "In vivo measurement of tumor blood oxygenation by near-infrared spectroscopy: immediate effects of pentobarbital overdose or carmustine treatment", *J. Neuro-Oncol.*, **22**, 209-220, 1994.
- ²⁴ H. D. Sostman, S. Rockwell, A. L. Sylvia, D. Madwed, G. Cofer, H. C. Charles, R. Negro-Vilar, and D. Moore, "Evaluation of BA1112 rhabdomyosarcoma oxygenation with microelectrodes, optical spectrophotometry, radiosensitivity, and magnetic resonance spectroscopy", *Magn. Reson. Med.*, **20**, 253-267, 1991.
- ²⁵ H. Liu, Y. Song, K. L. Worden, X. Jiang, A. Constantinescu, and R. P. Mason, "Noninvasive Investigation of Blood Oxygenation Dynamics of Tumors by Near-Infrared Spectroscopy", *Applied Optics*, **39**(28), 5231-5243, 2000.
- ²⁶ S. S. Kety, "The theory and applications of the exchange of inert gas at the lungs and tissue," *Pharmacol. Rev.*, **3**, 1-41, 1951.

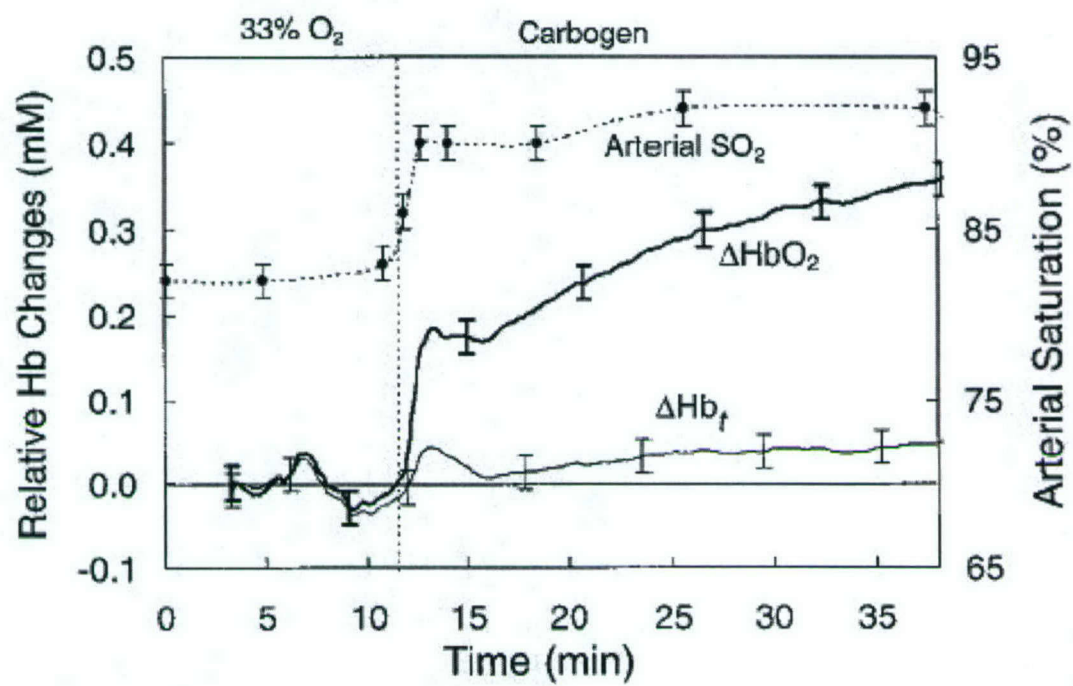


Figure 1

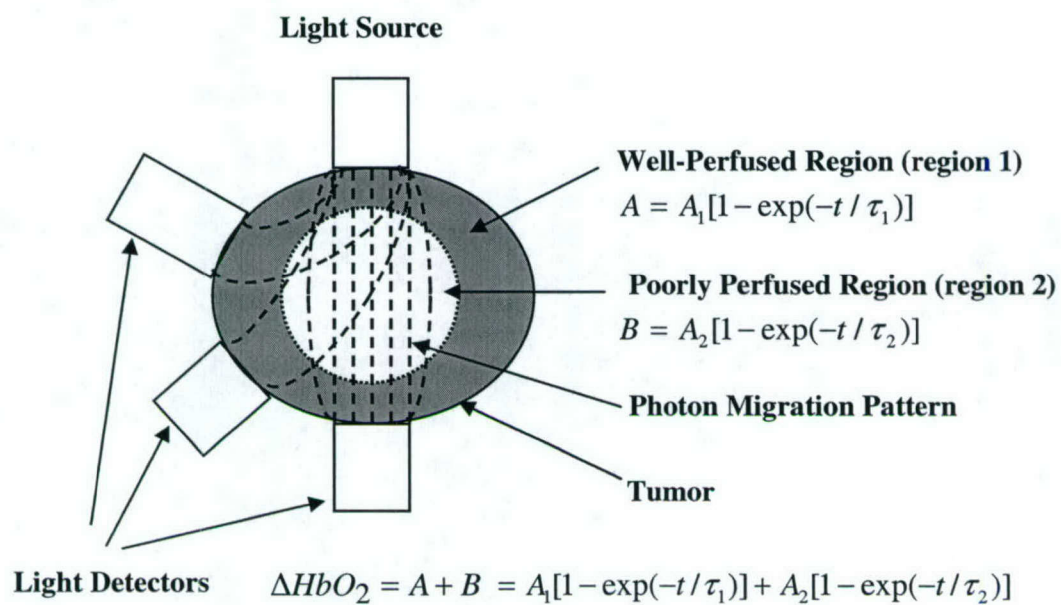


Figure 2

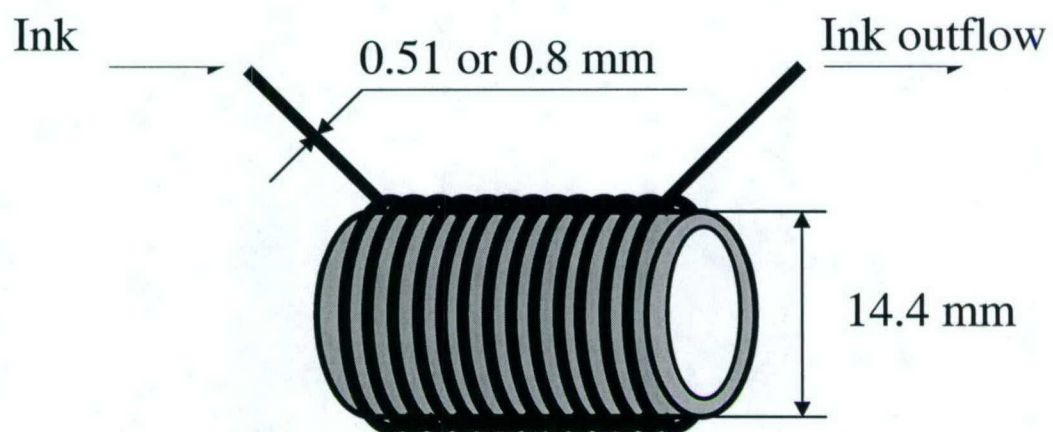


Figure 3

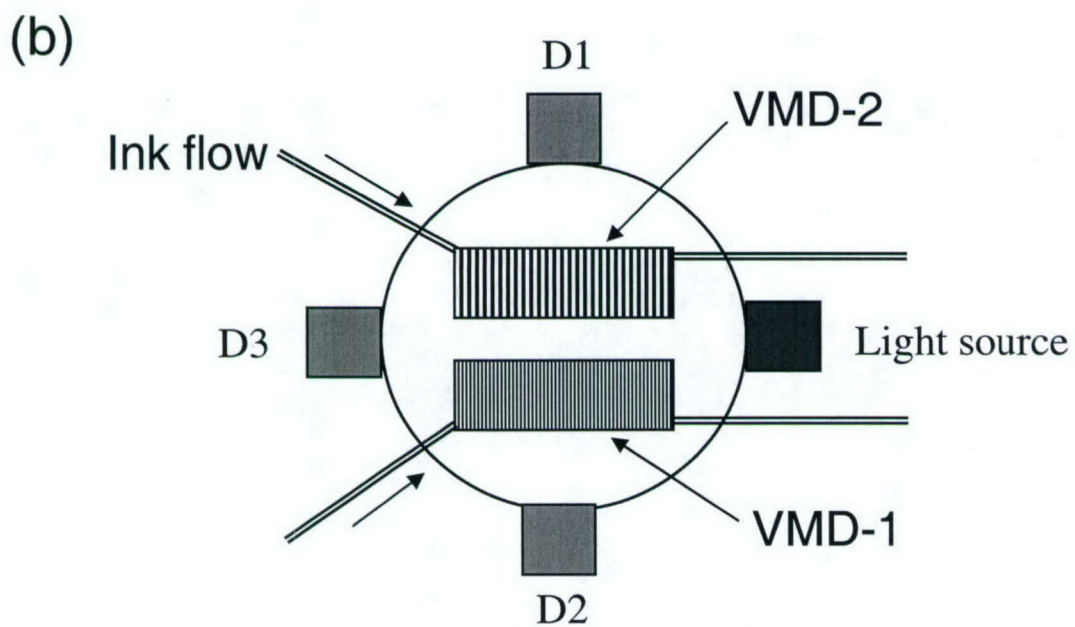
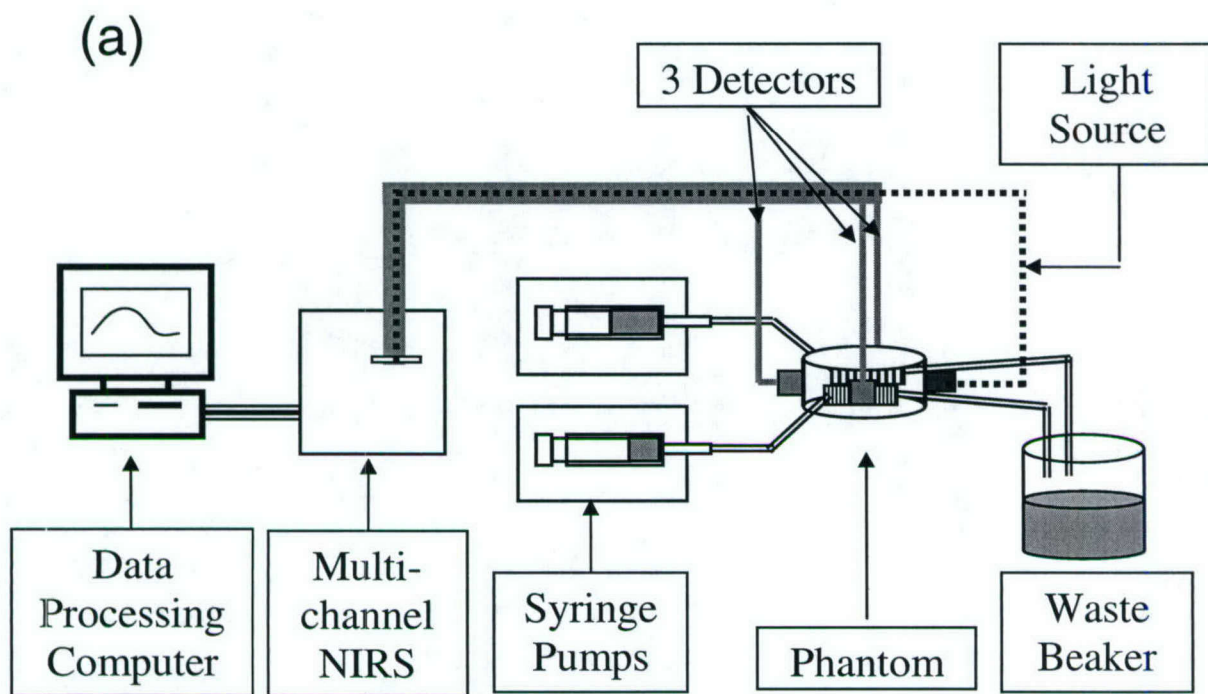


Figure 4

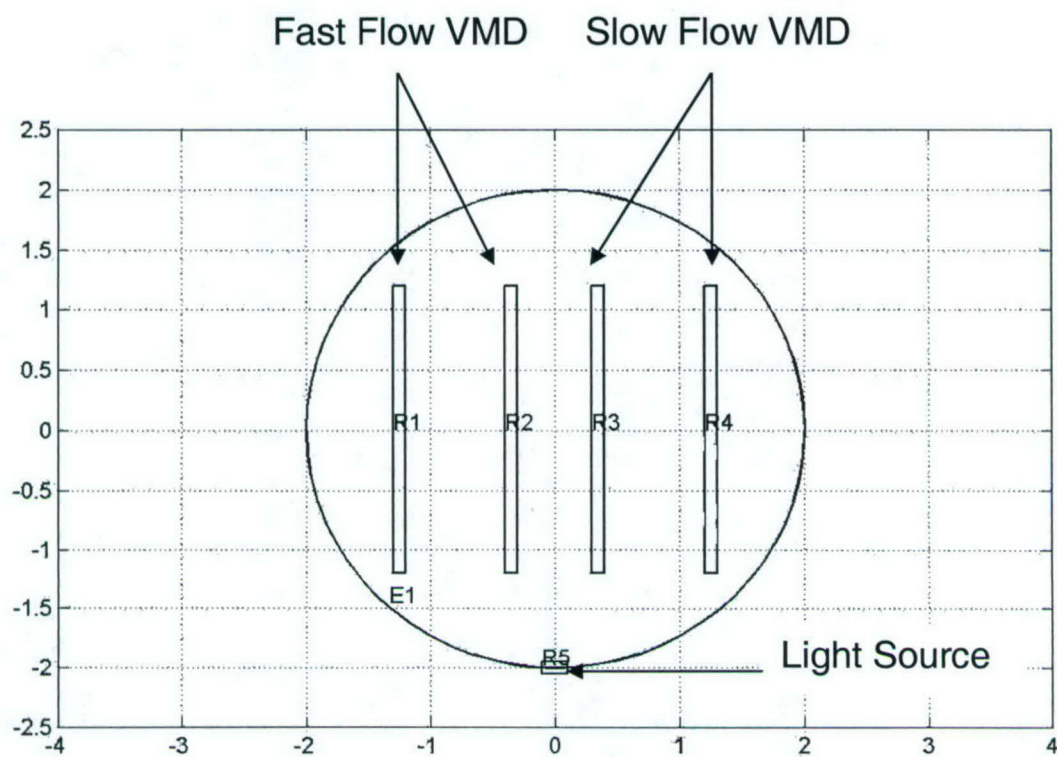


Figure 5

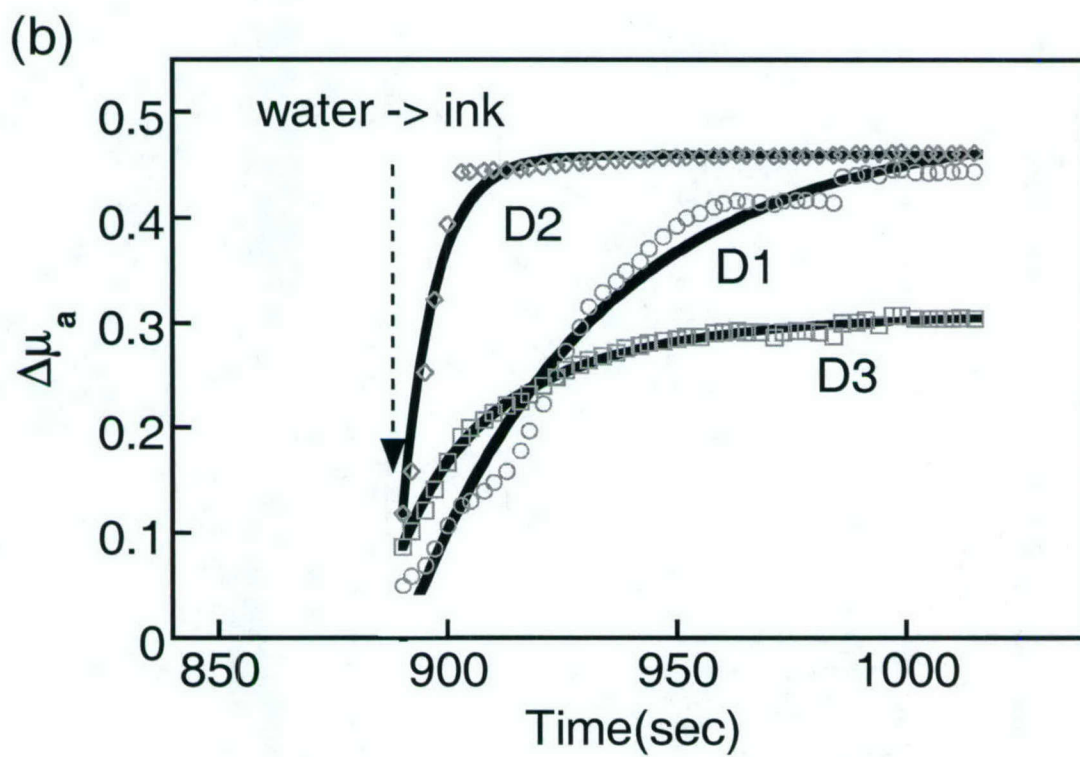
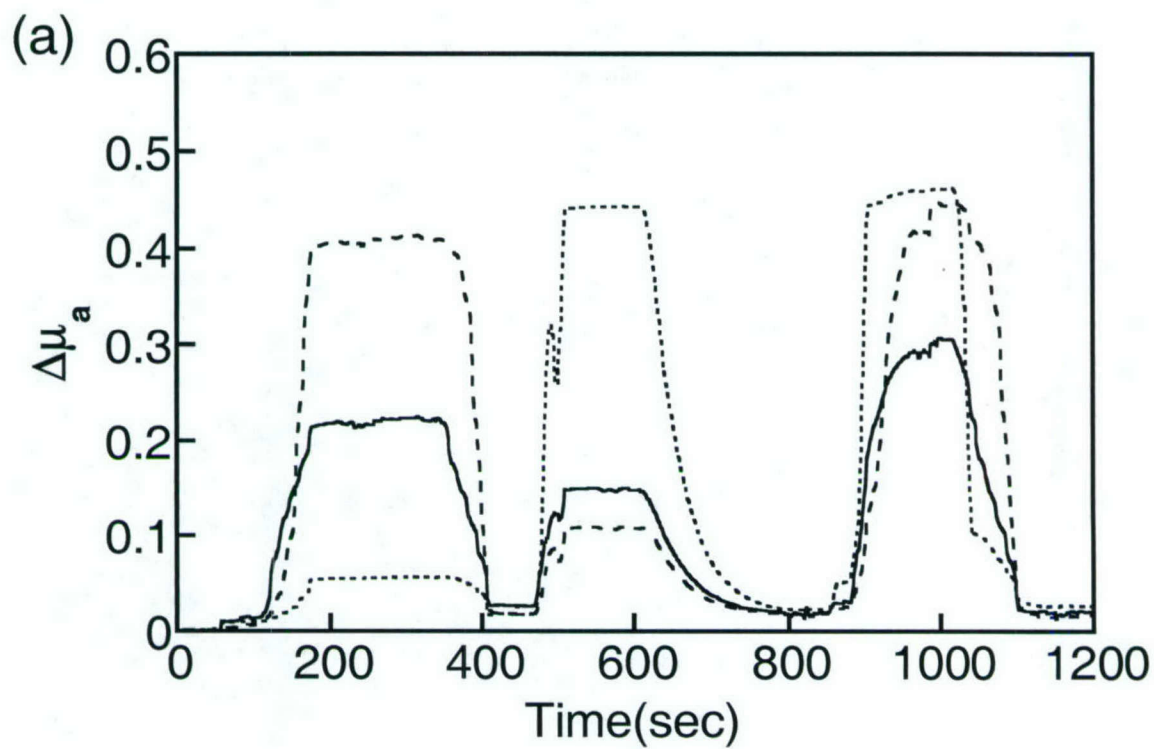


Figure 6

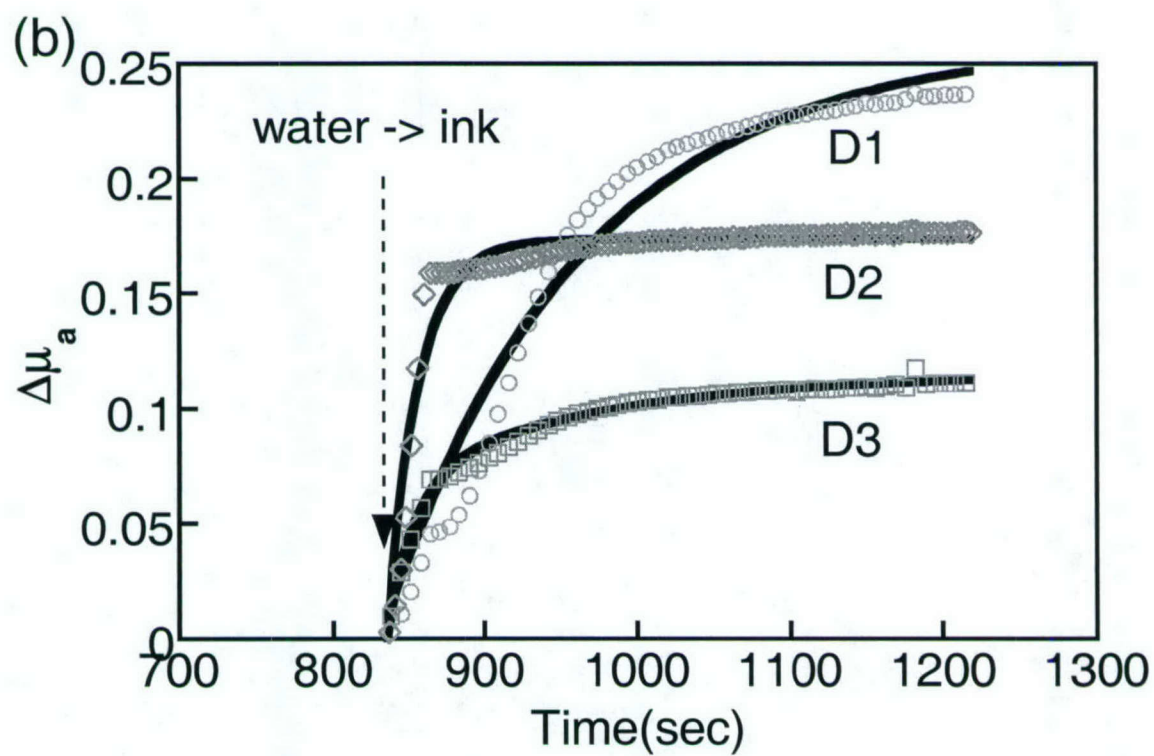
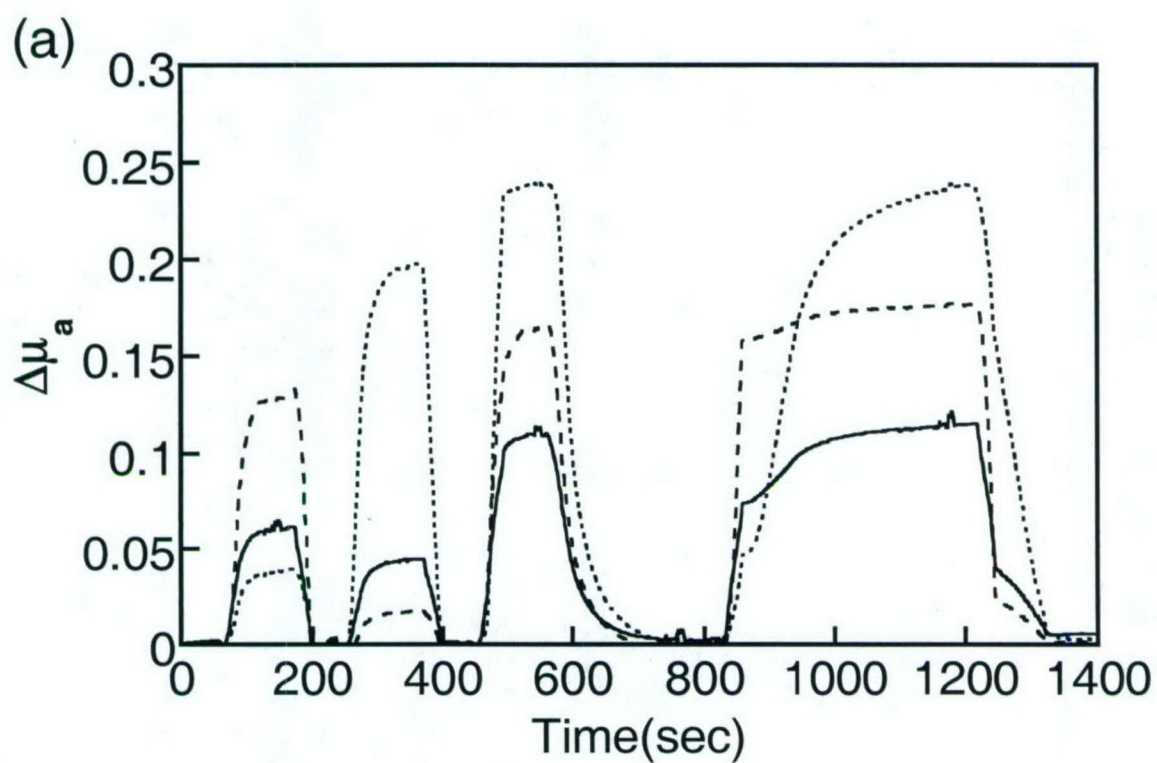
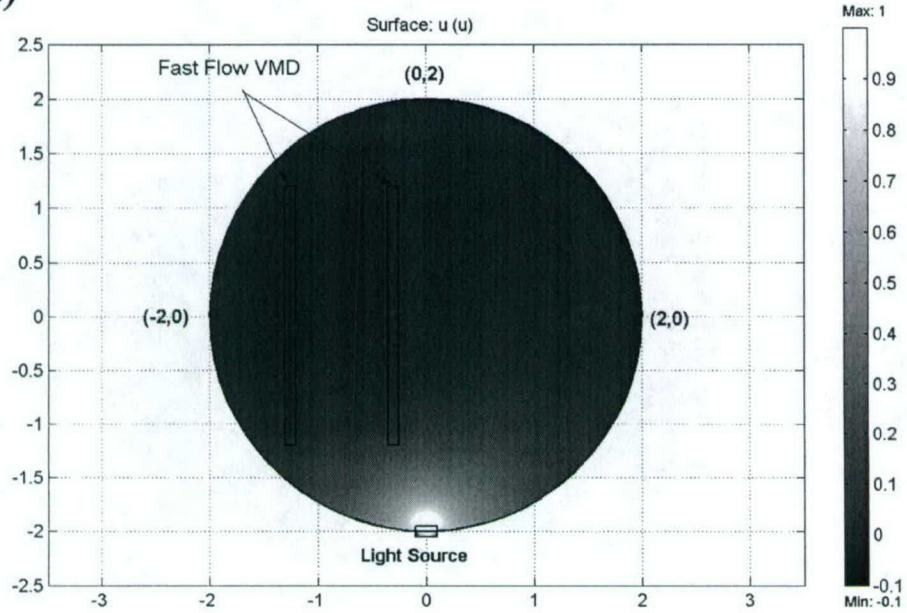


Figure 7

(a)



(b)

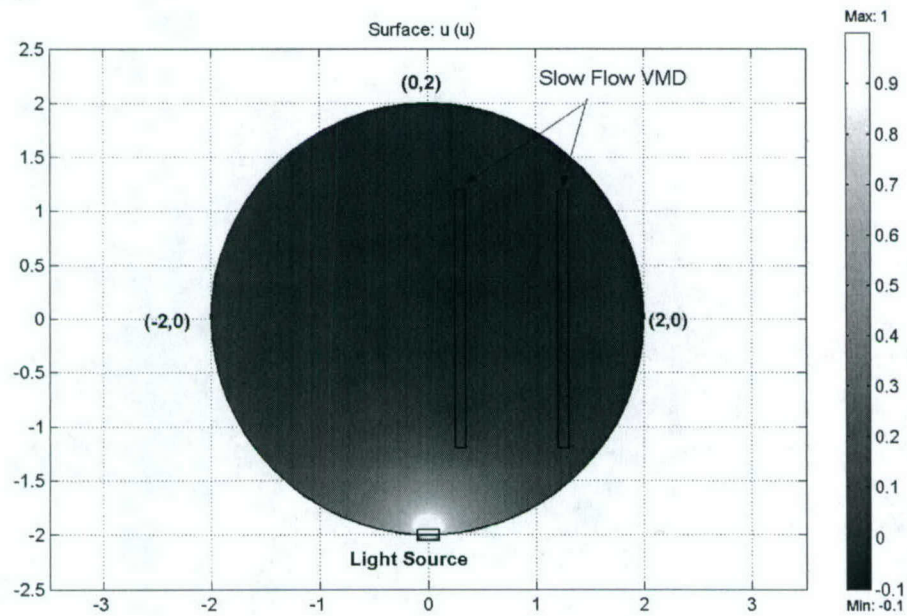


Figure 8

(c)

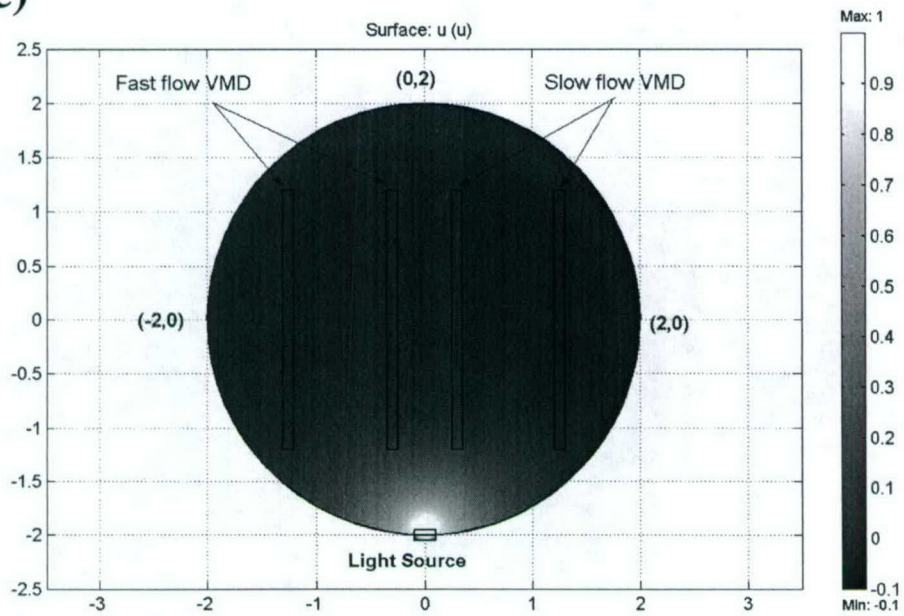


Figure 8

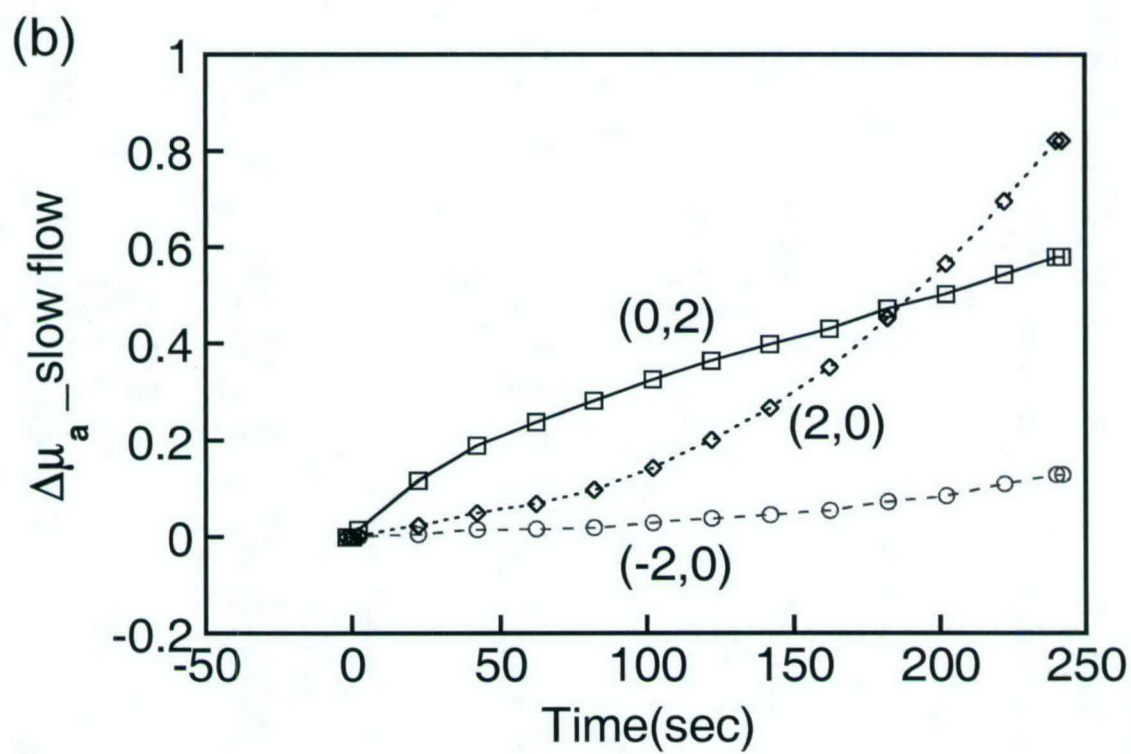
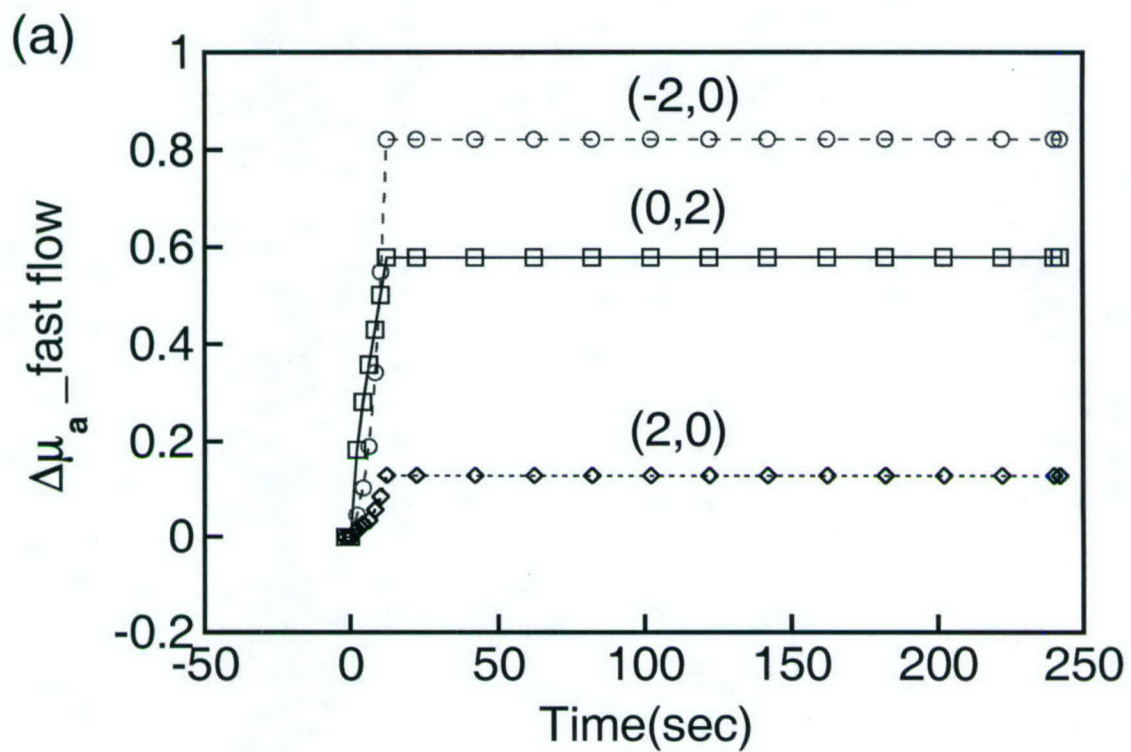


Figure 9

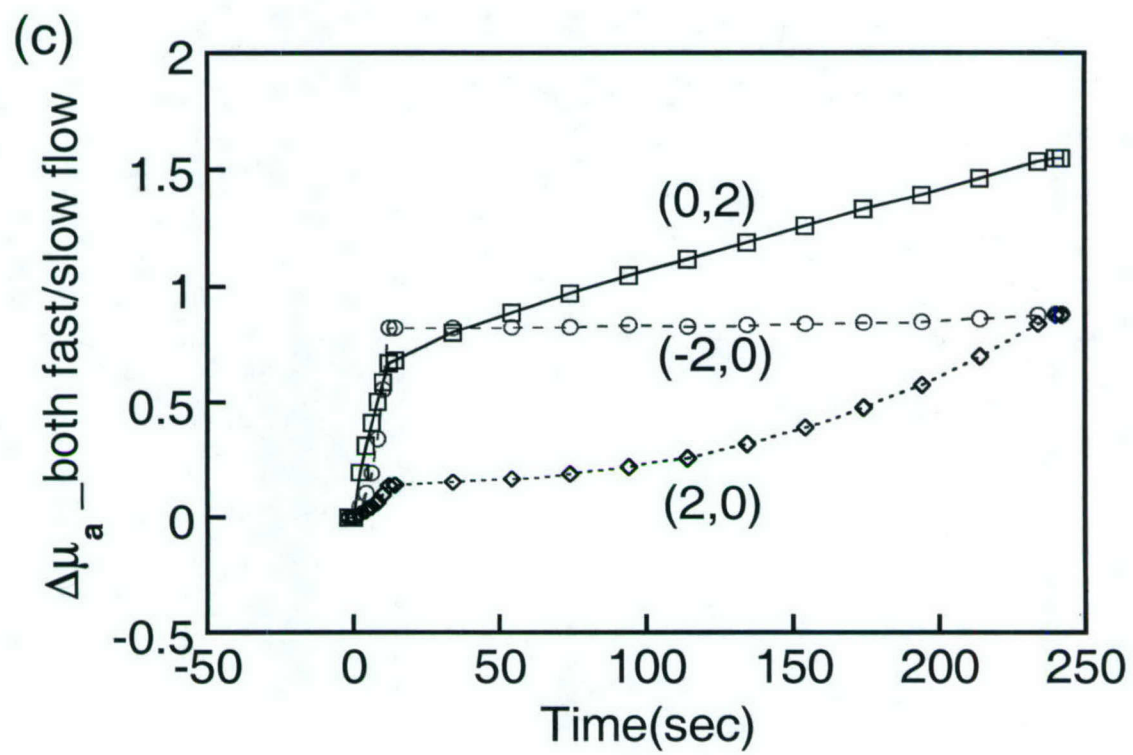


Figure 9

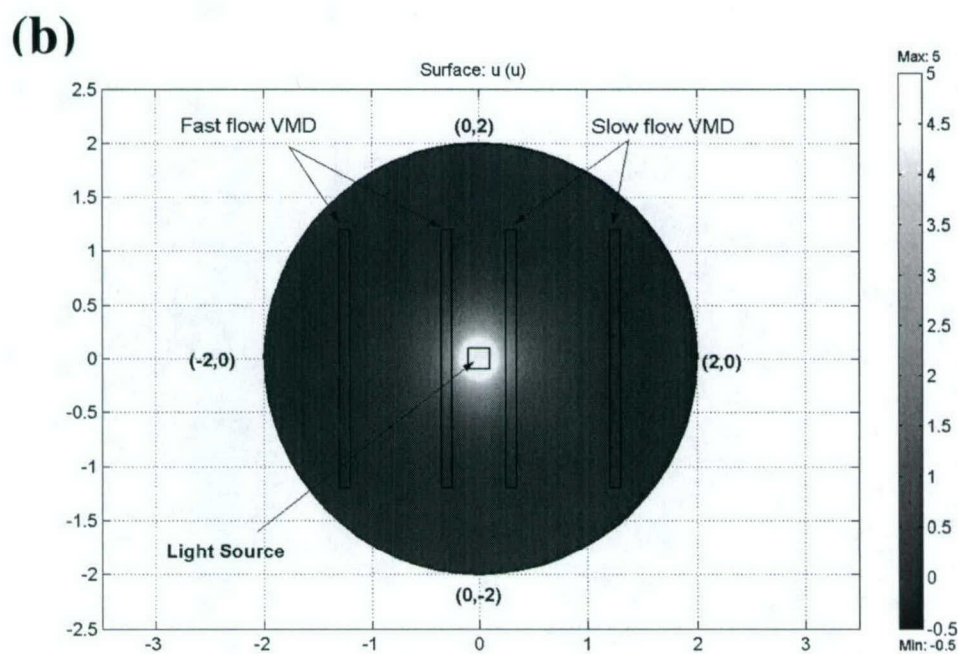
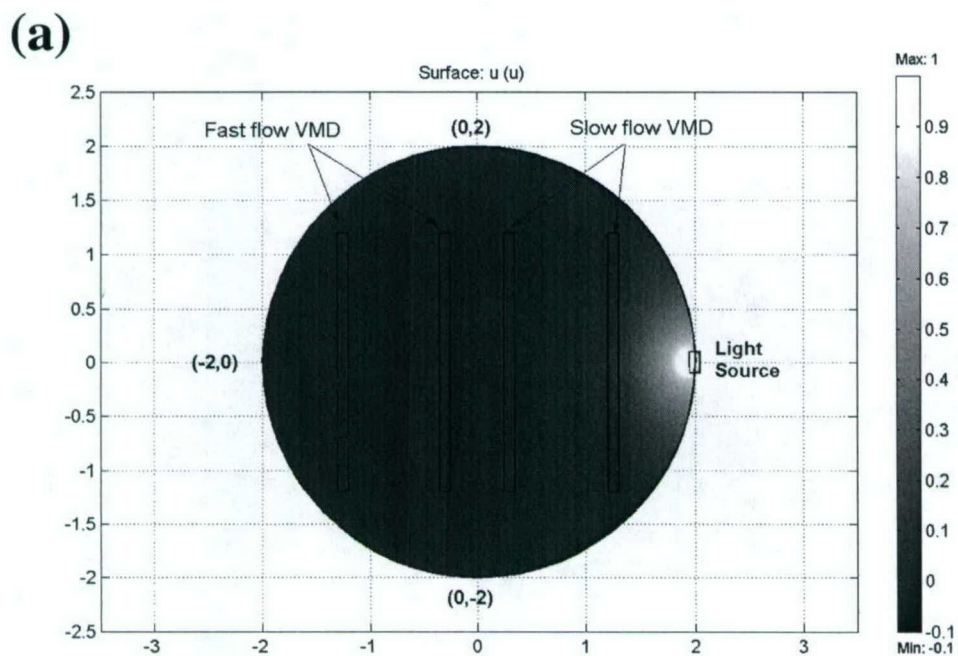


Figure 10

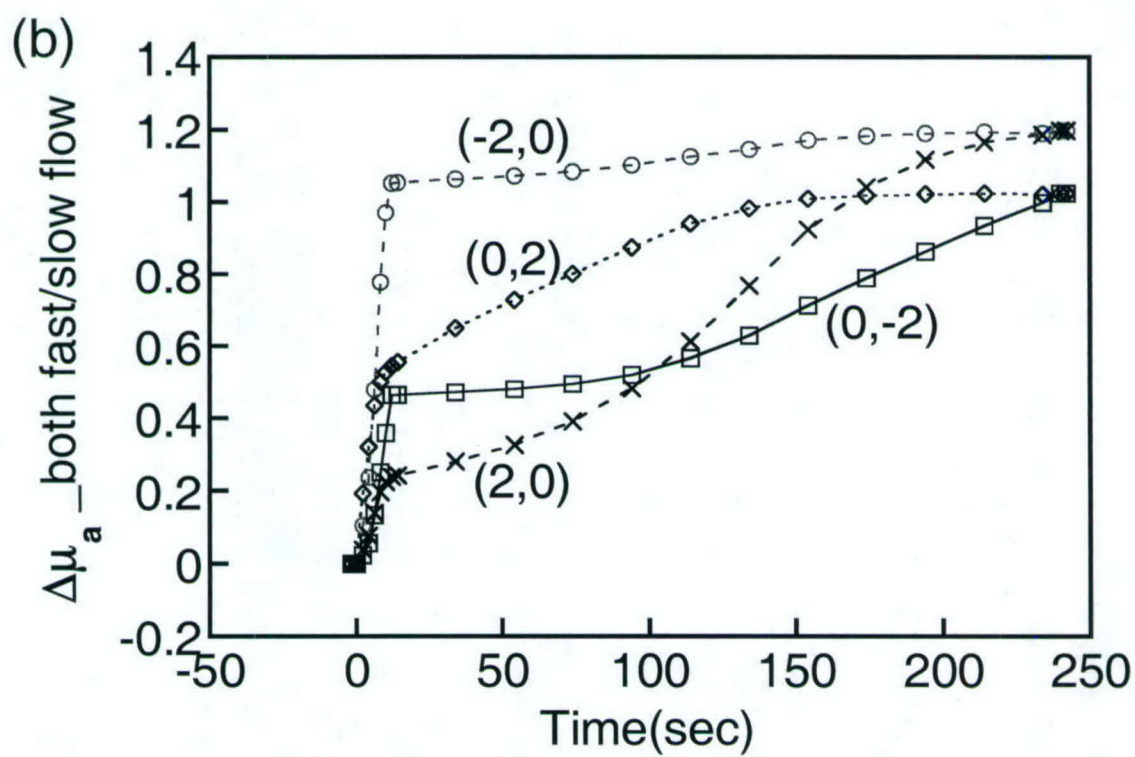
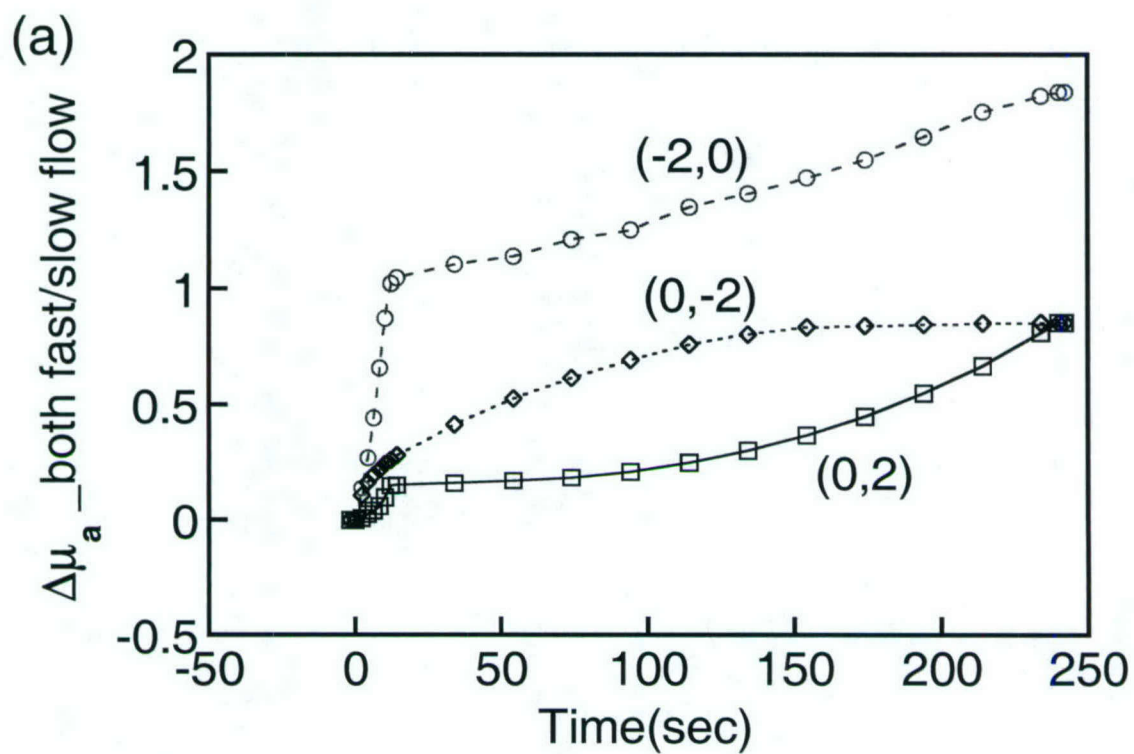


Figure 11

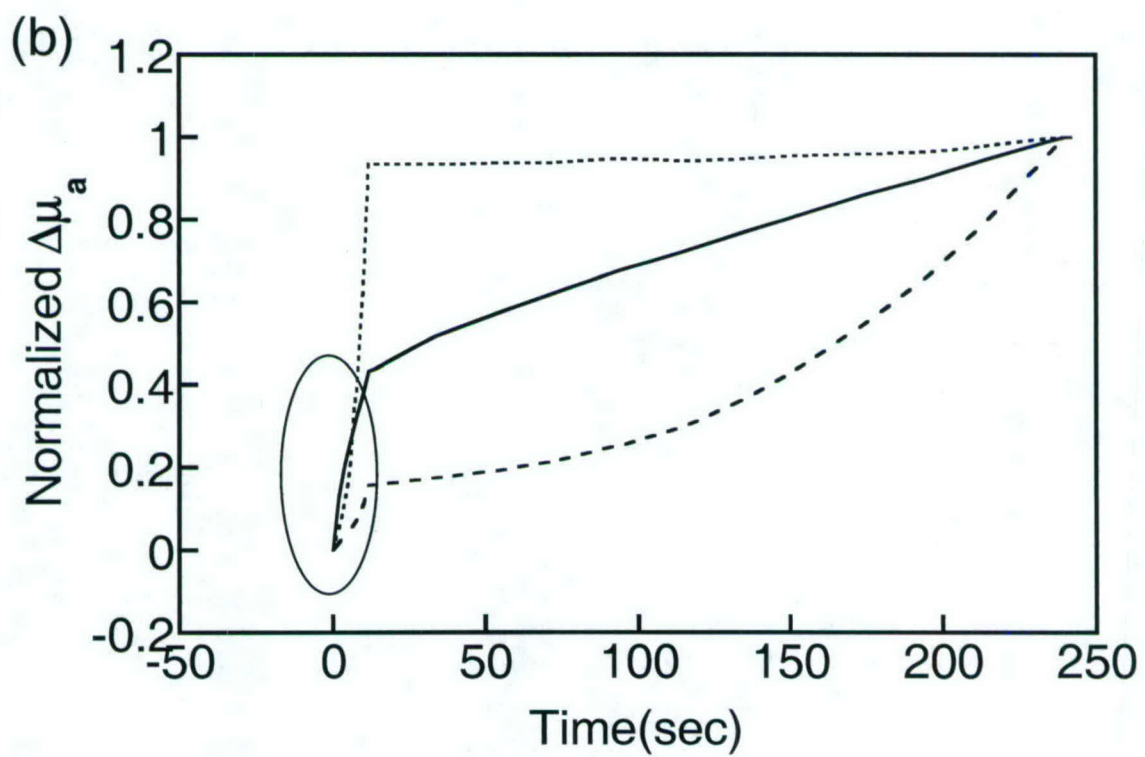
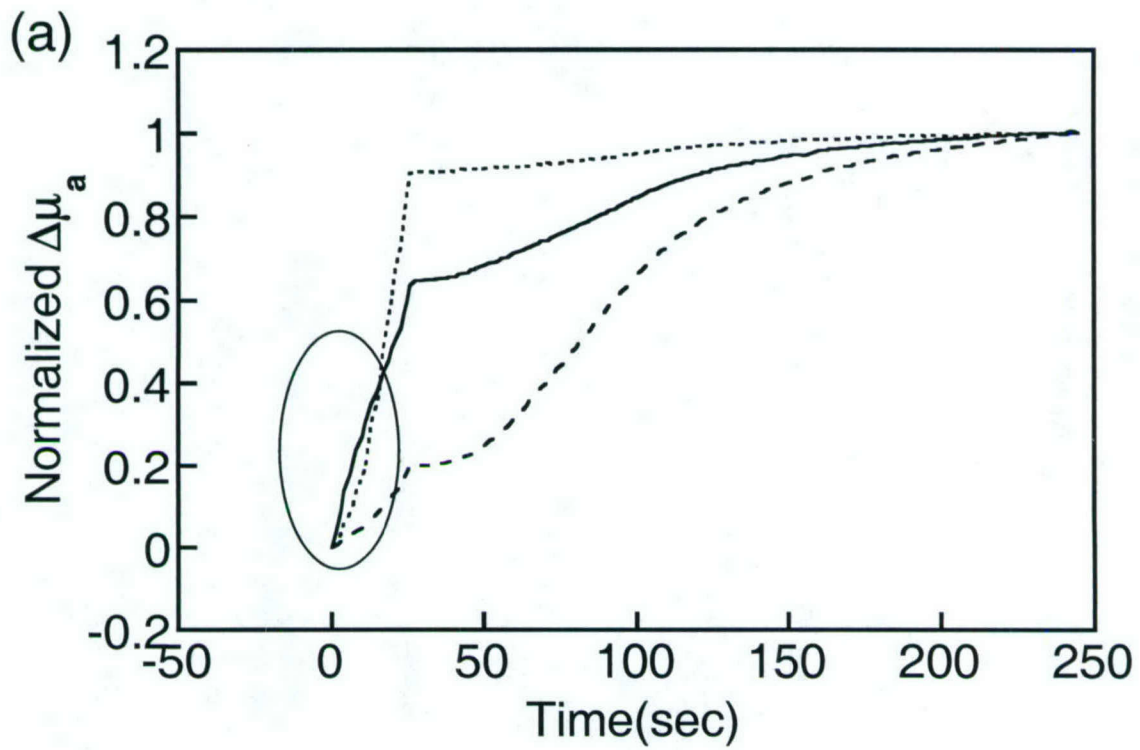


Figure 12

Non-Uniform Tumor Vascular Oxygen Dynamics Monitored By Multi-Channel Near-Infrared Spectroscopy

Jae G. Kim^a, Anca Constantinescu^b, Ralph P. Mason^b, Hanli Liu^{*a}

^aJoint Graduate Program in Biomedical Engineering,
University of Texas Southwestern Medical Center at Dallas/ University of Texas at Arlington
Arlington, TX 76019

^bAdvanced Radiological Sciences, Department of Radiology
University of Texas Southwestern Medical Center at Dallas
Dallas, TX 75390

ABSTRACT

In our previous report, we showed that there was a severe heterogeneity of tumor tissue oxygen dynamics even in a same tumor by using ^{19}F MR pO_2 mapping and near-infrared spectroscopy (NIRS). In this study, we applied a three channel NIRS system to reveal heterogeneity of tumor vascular oxygen dynamics during respiratory challenges. When the implanted tumor's size reached 3 cm, three photo detectors were attached on the surface of tumors in three different positions to measure changes in oxygenated hemoglobin concentration ($[\text{HbO}_2]$) while the inhaled gas was alternated between air and carbogen (95% oxygen, 5% CO_2). Significant changes in tumor oxygenation were observed accompanying respiratory challenge, and these changes could be modeled with either one or two exponential components with fast and slow time constants. Time constant, amplitude, vascular coefficient, and the ratio of perfusion rate obtained from fitting curves of $\Delta[\text{HbO}_2]$ measured from three photo detectors revealed that there were indeed different responses of tumor vascular oxygenation during carbogen inhalation from three different locations. These results clearly show that tumors are highly heterogeneous in terms of vascular oxygenation response to carbogen inhalation. This study demonstrates that the NIR technology can provide an efficient, real-time, non-invasive way for monitoring tumor physiology, and it may have prognostic value and promised insight into tumor vascular development and angiogenesis.

Keywords: Tumor vascular oxygenation, tumor heterogeneity, NIR Spectroscopy, carbogen

1. INTRODUCTION

Solid tumors develop regions of hypoxia during their growth due to an imbalance between the rate of tumor cell proliferation and the proliferation and branching of the blood vessels.^{1,2,3} Tumor hypoxia is responsible for the failure of radiotherapy,⁴ some forms of chemotherapy,⁵ and photodynamic therapy.⁶ In addition, a number of clinical trials have found that patient survival measured either as tumor regression or as local control depends largely on tumor oxygenation.⁷ Tumor hypoxia can occur through diffusion-limited or chronic hypoxia and perfusion-limited or acute hypoxia.⁸ Therefore, measurement of distribution of tumor perfusion rate could be important for tumor treatment planning and assessing methods designed to modulate tumor oxygenation.

Solid tumors are known to exhibit heterogeneous blood flow distribution.^{9,10} There are many methods to measure tumor perfusion heterogeneity, such as Doppler ultrasound,¹¹ dynamic contrast MRI,¹² and the use of tumors grown in windowed chambers.¹³ Intensive studies from Mason's group using ¹⁹F MR pO₂ mapping have revealed intratumoral heterogeneity of pO₂ distribution and also heterogeneous response to hyperoxic gas breathing.^{14,15,16} The group's findings of severe pO₂ heterogeneity in tumors can indirectly indicate the heterogeneous distribution of blood flow, since tissue pO₂ level is decided by a balance between the supply of oxygen from blood vessels and oxygen consumption by tissue cells.¹⁷ Unlike the ¹⁹F MR pO₂ mapping technique, near-infrared spectroscopy (NIRS) techniques cannot measure pO₂ in tissue but can measure *in vivo* hemoglobin saturation and concentration. NIRS has been applied to muscle,^{18,19,20} brain,^{21,22,23} and tumor.^{24,25,26}

In our previous study, we established a mathematical model of tumor oxygen dynamics during hyperoxic gas, such as carbogen (95% CO₂ and 5% O₂) or oxygen inhalation.²⁶ For our model, we formed a hypothesis that changes in oxygenated hemoglobin concentration ($\Delta[\text{HbO}_2]$) signal is composed of signals from well-

perfused and poorly perfused region to explain why there are two different time constants to fit the $\Delta[\text{HbO}_2]$ data using our model. In addition to time constant, we could get amplitude of fitted curve, ratio of vascular coefficients, and ratio of perfusion rates by applying our dynamic tumor oxygenation model. Therefore, we will be able to detect intratumoral perfusion heterogeneity by applying multi-channel NIRS, since each detector's signal will come from a different region of tumor and, thus, it will show differences of curve fitting parameters among multi-detectors.

The goals of this study were to measure $\Delta[\text{HbO}_2]$ in tumor vasculature during carbogen inhalation using a three channel NIRS system, and to reveal intratumoral vascular heterogeneity by fitting the $\Delta[\text{HbO}_2]$ data with our mathematical model.

2. MATERIALS AND METHODS

2.1 Tumor Model and Measurement

For our study, murine mammary adenocarcinomas 13762NF grown in the hind limb of adult female Fisher 344 rats (~200 g) were used. Once these tumors reached approximately 2-3 cm in diameter, the rats were anesthetized with 0.2 ml ketamine hydrochloride (100 mg/ml; Aveco, Fort Dodge, IA) and maintained under general gaseous anesthesia using a small animal anesthesia unit with air (1 dm³/min) and 1.3% isoflurane (Ohmeda PPD Inc., Fort Dodge, IA) through a mask placed over the mouth and nose. After anesthesia, the rat was placed on a warm blanket to maintain body temperature, which was monitored with a rectally-inserted thermal probe connected to a digital thermometer (Digi-Sense, model 91100-50, Cole-Parmer Instrument Company, Vernon Hills, IL). Tumors were shaved to improve optical contact for transmitting light, and a light source and three detectors were attached to the tumor using posts and swivel post clamps. A pulse oximeter (model: 8600V, Nonin, Inc.) was placed on the hind foot to monitor arterial oxygenation (S_aO_2) and heart rate. Figure 1 shows schematic setup for animal experiment using multi channel NIRS system.

All measurements were performed in the dark room, and measurements were initiated while the rats breathed air for 10 minutes to get a stable baseline. After 10 min of baseline measurement, the inhaled gas was switched to carbogen for 15 minutes, and then back to air for 15 minutes. Tumor volume V (in cm^3) was estimated as $V = (4\pi/3) [(L+W+H)/6]^3$,²⁷ where L , W , and H are the three respective orthogonal dimensions. Raw amplitude data from three detectors were recorded simultaneously during the experiments, and processed after the experiments to obtain the changes in oxygenated hemoglobin concentration ($\Delta[\text{HbO}_2]$) and total hemoglobin concentration ($\Delta[\text{Hb}_{\text{total}}]$). Time constant, amplitude, γ_1/γ_2 , and f_1/f_2 were calculated by fitting the data using Kaleidagraph software (Synergy Software, Reading, PA).

2.2 Multi-Channel NIR Spectroscopy

Our multi-channel NIR spectroscopy system has one light source and eight detectors to measure light signals from eight different locations, but due to tumor versus detector size constraints and to simplify the experiment, we only used three detectors to monitor tumor vascular oxygen dynamics during respiratory challenges.. In common with our previous work^{26,28}, we assume that oxyhemoglobin and deoxyhemoglobin are the only significant absorbance materials in the blood. The absorption coefficients comprise the extinction coefficients for deoxyhemoglobin and oxyhemoglobin multiplied by their respective concentrations (Eqs. 1 and 2).

$$\mu_a^{730} = \epsilon_{\text{Hb}}^{730}[\text{Hb}] + \epsilon_{\text{HbO}_2}^{730}[\text{HbO}_2], \quad (1)$$

$$\mu_a^{850} = \epsilon_{\text{Hb}}^{850}[\text{Hb}] + \epsilon_{\text{HbO}_2}^{850}[\text{HbO}_2]. \quad (2)$$

The data presented in this paper were analyzed using modified Beer-Lambert's law and amplitude values to find the changes in absorption (Eq. 3). By manipulating Equations 1-3, changes in oxygenated hemoglobin,

deoxygenated hemoglobin and total hemoglobin concentrations were calculated from the transmitted amplitude of the light through the tumor (Eqs. 4, 5 and 6).

$$\mu_{aB} - \mu_{aT} = \log (A_B/A_T) / L, \quad (3)$$

$$\Delta[\text{HbO}_2] = [-0.674 \cdot \log (A_B/A_T)^{730} + 1.117 \cdot \log (A_B/A_T)^{850}] / L, \quad (4)$$

$$\Delta[\text{Hb}] = [0.994 \cdot \log (A_B/A_T)^{730} - 0.376 \cdot \log (A_B/A_T)^{850}] / L, \quad (5)$$

$$\Delta[\text{Hb}]_{\text{total}} = \Delta[\text{Hb}] + \Delta[\text{HbO}_2] = [0.32 \cdot \log (A_B/A_T)^{730} + 0.741 \cdot \log (A_B/A_T)^{850}] / L, \quad (6)$$

where A_B = baseline amplitude; A_T = transition amplitude; L = optical pathlength between source/detector. The constants were computed with the extinction coefficients for oxy and deoxyhemoglobin at the two wavelengths used.²⁹ In principle, L should be equal to the source–detector separation, d , multiplied by a differential pathlength factor (DPF), i.e., $L = d \cdot \text{DPF}$. Little is known about DPF for tumors, although a DPF value of 2.5 has been used by others.³⁰ Since our focus is on dynamic changes and relative values of tumor $[\text{HbO}_2]$ with respect to carbogen intervention, we have taken the approach of including the DPF in the unit, i.e., modifying eq. (4) as follows:

$$\Delta[\text{HbO}_2] = [-0.674 \cdot \log (A_B/A_T)^{730} + 1.117 \cdot \log (A_B/A_T)^{850}] / d, \quad (7)$$

where d is the direct source-detector separation in cm, and the unit of $\Delta[\text{HbO}_2]$ in Eq. (7) is mM/DPF.

2.3 Mathematical Model of Tumor Vascular Oxygenation

In our previous report,²⁶ we followed an approach used to measure regional cerebral blood flow (rCBF) with diffusible radiotracers, as originally developed by Kety³¹ in the 1950's, to develop our model. By applying Fick's principle and defining γ as the ratio of HbO₂ concentration changes in the vascular bed to that in veins, which is equal to $(\Delta\text{HbO}_2^{\text{vasculature}})/(\Delta\text{HbO}_2^{\text{vein}})$, we could get Eq. (8) as follows:

$$\Delta\text{HbO}_2^{\text{vasculature}}(t) = \gamma H_0 [1 - \exp(-ft/\gamma)] = A_1 [1 - \exp(-t/\tau_1)] \quad (8)$$

where γ is the vasculature coefficient of the tumor, H_0 is the arterial oxygenation input and f is the blood perfusion rate.

If a tumor has two distinct perfusion regions, and the measured signal is from both regions (Figure 2), then it is reasonable that we will get two different blood perfusion rates f_1 and f_2 , two different vasculature coefficients γ_1 and γ_2 , or all four. Therefore, Eq. (8) can be modified to double exponential expression as

$$\begin{aligned} \Delta\text{HbO}_2^{\text{vasculature}}(t) &= \gamma_1 H_0 [1 - \exp(-f_1 t/\gamma_1)] + \gamma_2 H_0 [1 - \exp(-f_2 t/\gamma_2)] \\ &= A_1 [1 - \exp(-t/\tau_1)] + A_2 [1 - \exp(-t/\tau_2)] \end{aligned} \quad (9)$$

where f_1 and γ_1 are the blood perfusion rate and the vasculature coefficient, respectively, in region 1, f_2 and γ_2 are the same for region 2, and $A_1 = \gamma_1 H_0$, $A_2 = \gamma_2 H_0$, $\tau_1 = f_1/\gamma_1$, $\tau_2 = f_2/\gamma_2$. Then, if A_1 , A_2 , τ_1 , and τ_2 are determined from our measurements, we can obtain the ratios of two vasculature coefficients and the two blood perfusion rates:

$$\frac{\gamma_1}{\gamma_2} = \frac{A_1}{A_2}, \quad \frac{f_1}{f_2} = \frac{A_1/\tau_1}{A_2/\tau_2}. \quad (10)$$

With these two ratios, we will be able to understand more about tumor physiology such as vasculature and blood perfusion. In this report, we used three-channel NIR spectroscopy to explore the tumor vascular heterogeneity by obtaining A_1 , A_2 , τ_1 , and τ_2 from three different locations on tumors.

3. RESULTS

Figure 3(a) shows the $\Delta[\text{HbO}_2]$ obtained from three detectors in a small breast tumor (1.54 cm^3), with a source-detector separation of 1 cm for detector #1, 1.3 cm for detector #2, and 1.8 cm for detector #3, respectively. Detectors #1 and #2 are placed on the side of tumor in a reflection mode while detector #3 was located across of light source in a transmittance mode. The measurement uncertainties are shown at only discrete locations. After 5 min of air breathing measurement as a baseline, inhaled gas was switched from air to carbogen, which caused a sharp increase in $\Delta[\text{HbO}_2]$ ($p < 0.0001$ after 1 min from gas switch) followed by a further slow, gradual, but significant, increase over the next 15 min ($P < 0.0001$).

The rising part of $\Delta[\text{HbO}_2]$ from detector #1, #2, and #3 after gas switch from air to carbogen and the fitted curves are shown in Figure 3(b) – 3(d), respectively. We used single-exponential (Eq. 8) and double-exponential expressions (Eq. 9) to fit the data of rising portion of $\Delta[\text{HbO}_2]$ and it appears that double-exponential expression gives a slightly better fit, as is confirmed by the respective R values [0.99 versus 0.98 (not shown in the table)]. Time constants and amplitudes from three fitted curves are summarized in the Table 1 to describe tumor vascular structure and blood perfusion. By manipulating time constants and amplitudes, we can get physiologically meaningful parameters such as $\gamma_1/\gamma_2 = A_1/A_2$ and $f_1/f_2 = (A_1/A_2)/(\tau_1/\tau_2)$ (Eq. 10). When γ_1/γ_2 is close to 1, it implies that the measured signal results equally from both region 1 and 2, and if $\gamma_1/\gamma_2 < 1$, then the measured signal results more from region 1 than region 2 [Figure 3(b), 3(c) and 3(d)]. All the ratios of f_1/f_2 in Figure 3(b) – 3(d) are larger than 1, which indicate the blood perfusion rate in region 1 is much higher than that in region 2.

Figure 4 depicts $\Delta[\text{HbO}_2]$ obtained from another large breast tumor (16.6 cm³). The fast and significant increases of $\Delta[\text{HbO}_2]$ after switching gas from air to carbogen are similar to those from tumor in Figure 3. However, double-exponential fitting shows much better fitness compared to single-exponential expression in this tumor ($R=0.79\sim0.84$ from single exponential model fitting) and also this tumor has several different characteristics compared to tumor in Figure 3 as can be seen from Table 2. First, this tumor has very different values of time constants between detectors, while the tumor in Figure 3 has close values of time constants between detectors. Fast time constants in Figure 3 are 0.25, 0.23, and 0.26 min, and slow time constants in Figure 3 are 9.16, 8.06, and 8.52 min, which do not have a significant differences between detectors ($p >$), but tumor in Figure 4 shows very different values of time constant between detectors ($p<0.001$ between detector # and # and $p<$ between detector # and #). Fast time constants in Figure 4 are 0.24, 0.30, and 0.27 min, and slow time constants in Figure 4 are 8.3, 9.9, and 7.0 min. In addition to time constants, the γ_1/γ_2 and f_1/f_2 are also very different from those in the Table 1. Figures 4(b) and 4(d) have $\gamma_1/\gamma_2 >1$ while all the detectors in Figure 3 show $\gamma_1/\gamma_2 <1$, which implies that signals from detectors #1 and #3 in Figure 4 are mainly from region 1 rather than region 2. The ratios of perfusion rate in Figure 4, f_1/f_2 , are also much greater than those from tumor in Figure 3.

4. DISCUSSION

We have seen tumor heterogeneity in terms of tissue $p\text{O}_2$ using ^{19}F MR $p\text{O}_2$ mapping via reports from Dr. Mason's research group.^{14,15,16} ^{19}F MR $p\text{O}_2$ mapping technique clearly showed that tumor tissue has a wide distribution of $p\text{O}_2$, and also different responses to respiratory challenges even within a tumor. We know that tissue $p\text{O}_2$ is mainly decided by the balance between the supply of oxygen from blood vessels, and the oxygen

consumption by tissue cells. With assumption of constant oxygen consumption during gas switch from air to carbogen, tumor tissue pO_2 will be mainly dependent of blood oxygen level changes.

NIRS is a portable, low cost, real time measurement system that can measure changes of blood oxygen level by using two wavelengths. We have used a NIRS system that has one light source and one detector so that we could have global measurement of $\Delta[HbO_2]$ and $\Delta[Hb_{total}]$ in tumor during respiratory challenges. Through our previous experiments, we found that most of tumors have bi-phasic behavior of $\Delta[HbO_2]$ increase (rapid increase followed by a slow and gradual increase) after switching the gas from air to carbogen or air to 100% oxygen. To explain this bi-phasic behavior, we formed a hypothesis that the bi-phasic behavior of $\Delta[HbO_2]$ increase during carbogen or oxygen inhalation results from two different regions in tumors in terms of blood perfusion rate and vascular structure, and we developed a mathematical model to get physiologically meaningful parameters from experimental data.

The region in tumor that has fast blood perfusion rate, f_1 , and high ratio of $\Delta[HbO_2]^{vasculature}$ and $\Delta[HbO_2]^{vein}$, γ_1 , is called region 1, while region 2 represents the region that has slow blood perfusion rate, f_2 , and low ratio of $\Delta[HbO_2]^{vasculature}$ and $\Delta[HbO_2]^{vein}$, γ_2 . Thus, the ratio of γ_1 and γ_2 can be simply thought of as a ratio of region 1 volume to region 2 volume. In other words, when a tumor has $\gamma_1/\gamma_2 \approx 1$, it implies that the tumor consists of 50% well-perfused region and 50% poorly perfused region. If a tumor has $\gamma_1/\gamma_2 < 1$ or $\gamma_1/\gamma_2 > 1$, this means the measured signal results mostly from poorly perfused region, or well-perfused region, respectively. Therefore, by looking at these two ratios from Table 1 and 2, we can find the differences between tumor in Figure 3 and tumor in Figure 4 in terms of blood perfusion rate and proportion of either well-perfused region or poorly perfused region. For instance, a large proportion of tumor in Fig. 3 consists of well-perfused region ($\gamma_1/\gamma_2 = 0.96 \sim 2.23$) while tumor in Figure 4 is mostly composed of poorly perfused region ($\gamma_1/\gamma_2 = 0.135 \sim 0.343$). In the case of tumor in Figure 3, the blood perfusion rate in the well-perfused region is much faster

than in the poorly perfused region, while the ratio of blood perfusion rate between well-perfused region and poorly perfused region from tumor in Figure 4 ($f_1/f_2 = 5.13 \sim 18.33$) is not as high as tumor in Figure 3 ($f_1/f_2 = 31.58 \sim 63.75$).

5. CONCLUSION

We applied a three channel NIRS system to show the heterogeneity of tumor vasculature in terms of blood perfusion rate and vascular coefficients. All detectors on tumor showed a sharp increase of $\Delta[\text{HbO}_2]$ that was followed by slow and gradual increase. However, the differences between the signals from three detectors could be found by applying our mathematical model to fit the $\Delta[\text{HbO}_2]$ data during carbogen inhalation. Although all signals from three detectors in both Figures 3 and 4 showed bi-phasic behavior of $\Delta[\text{HbO}_2]$, their time constants and ratio of γ_1/γ_2 and f_1/f_2 revealed that tumor vasculature is not homogeneous and, indeed, it is heterogeneous with respect to blood perfusion rate and proportion of well-perfused region in tumor. Our future study will be conducted to prove our hypothesis on the bi-phasic behavior of $\Delta[\text{HbO}_2]$ during carbogen inhalation and to learn more about meaning of time constant, amplitude, γ_1/γ_2 , and f_1/f_2 from our mathematical model.

ACKNOWLEDGEMENTS

This work was supported in part by The American Cancer Society RPG-97-116-010CCE (RPM), NIH RO1 CA79515 (RPM), the Department of Defense Breast Cancer Initiative grants DAMD17-03-1-0353 (JGK) and BC990287 (HL).

FIGURE CAPTION

Figure 1. Schematic experimental setup of animal experiment. One of three detectors is placed opposite of the light source to detect light in transmission mode, and the other two were located in the semi-reflection mode.

Figure 2. Schematic diagram of two-region tumor model. If tumor has two distinct regions in terms of perfusion rate, the detector will get signal from both regions, and the signal can be fitted with double exponential expression.

Figure 3. Dynamic changes of $[\text{HbO}_2]$ from three detectors in a rat breast (volume: 1.5 cm^3) tumor A. Dotted vertical lines mark the point when the gas was changed [Fig. 3(a)]. The rising part of $\Delta[\text{HbO}_2]$ from detectors was fitted using both single-exponential and double-exponential expressions and Fig. 3(b)-3(d) are from detector #1-#3, respectively.

Figure 4. Dynamic changes of $[\text{HbO}_2]$ from three detectors in a rat breast (volume: 16.6 cm^3) tumor B. Dotted vertical lines mark the point when the gas was changed [Fig. 4(a)]. Figures 4(b)-4(d) show the rising part of $\Delta[\text{HbO}_2]$ after gas switch from air to carbogen, and fitted curves in detector #1-#3, respectively.

Figure 5. Dynamic changes of $[\text{HbO}_2]$ from three detectors in a rat breast (volume: 20.6 cm^3) tumor C. Dotted vertical lines mark the point when the gas was changed [Fig. 5(a)]. Figures 5(b)-5(d) show the rising part of $\Delta[\text{HbO}_2]$ after gas switch from air to carbogen, and fitted curves in detector #1-#3, respectively.

Table 1. Summary of vascular oxygen dynamics determined at the three detectors from Figure 3 for Tumor A

Double-Exponential fitting $\Delta\text{HbO}_2 = A_1[1-\exp(-t/\tau_1)] + A_2[1-\exp(-t/\tau_2)]$			
Parameters	Detector #1 (Fig. 3b)	Detector #2 (Fig. 3c)	Detector #3 (Fig. 3d)
Separation: d (cm)	1.0	1.3	1.8
A_1 (mM/DPF)	0.0069 ± 0.0003	0.0055 ± 0.0002	0.004 ± 0.0002
τ_1 (min)	0.25 ± 0.04	0.23 ± 0.04	0.26 ± 0.05
A_2 (mM/DPF)	0.041 ± 0.001	0.032 ± 0.0003	0.024 ± 0.0003
τ_2 (min)	9.16 ± 0.37	8.06 ± 0.27	8.52 ± 0.36
χ^2	0.00047	0.0003	0.00021
R	0.99	0.99	0.99
$\gamma_1/\gamma_2 = A_1/A_2$	0.17 ± 0.01	0.17 ± 0.01	0.17 ± 0.01
τ_1/τ_2	0.027 ± 0.005	0.029 ± 0.006	0.031 ± 0.007
$f_1/f_2 = (A_1/A_2)/(\tau_1/\tau_2)$	6.3 ± 1.9	5.9 ± 2	5.5 ± 2

Table 2. Summary of vascular oxygen dynamics determined at the three detectors from Figure 4 for Tumor B

Double-Exponential fitting $\Delta\text{HbO}_2 = A_1[1-\exp(-t/\tau_1)] + A_2[1-\exp(-t/\tau_2)]$			
Parameters	Detector #1 (Fig. 4b)	Detector #2 (Fig. 4c)	Detector #3 (Fig. 4d)
Separation: d (cm)	1.5	2.5	2.8
A_1 (mM/DPF)	0.0370 ± 0.0004	0.0125 ± 0.0002	0.0134 ± 0.0002
τ_1 (min)	0.24 ± 0.01	0.30 ± 0.02	0.27 ± 0.01
A_2 (mM/DPF)	0.020 ± 0.001	0.013 ± 0.0004	0.006 ± 0.0001
τ_2 (min)	8.3 ± 0.7	9.9 ± 0.8	7.0 ± 0.6
χ^2	0.0045	0.001	0.00046
R	0.95 0.79	0.96 0.82	0.95 0.84
$\gamma_1/\gamma_2 = A_1/A_2$	1.85 ± 0.07	0.96 ± 0.05	2.23 ± 0.08
τ_1/τ_2	0.029 ± 0.004	0.03 ± 0.004	0.039 ± 0.005
$f_1/f_2 = (A_1/A_2)/(\tau_1/\tau_2)$	64 ± 9	32 ± 5	56 ± 9

Table 3. Summary of vascular oxygen dynamics taken at the three detectors from Figure 5 for Tumor C

Double-Exponential fitting $\Delta\text{HbO}_2 = A_1[1-\exp(-t/\tau_1)] + A_2[1-\exp(-t/\tau_2)]$			
Parameters	Detector #1 (Fig. 4b)	Detector #2 (Fig. 4c)	Detector #3 (Fig. 4d)
Separation: d (cm)	2	2.5	3
A_1 (mM/DPF)	0.01 ± 0.0003	0.0072 ± 0.0001	0.0023 ± 0.0001
τ_1 (min)	0.27 ± 0.03	0.43 ± 0.02	0.16 ± 0.04
A_2 (mM/DPF)	0.033 ± 0.0003	0.021 ± 0.002	0.017 ± 0.0001
τ_2 (min)	4.7 ± 0.1	23 ± 3	6.1 ± 0.2
χ^2	0.00093	0.00019	0.00031
R	0.99 0.97	0.99 0.91	0.99 0.98
$\gamma_1/\gamma_2 = A_1/A_2$	0.30 ± 0.01	0.34 ± 0.03	0.135 ± 0.009
τ_1/τ_2	0.058 ± 0.007	0.019 ± 0.003	0.026 ± 0.007
$f_1/f_2 = (A_1/A_2)/(\tau_1/\tau_2)$	5.2 ± 0.7	18 ± 4	5 ± 1

REFERENCES

- ¹ P. Vaupel, O. Thews, D. K. Kelleher, and M. Höckel, "Current status of knowledge and critical issues in tumor oxygenation", In: Hudetz and Bruley (eds), *Oxygen Transport to Tissue XX*, 591-602, Plenum Press, New York, 1998.
- ² P. Vaupel, "Vascularization, blood flow, oxygenation, tissue pH, and bioenergetic status of human breast cancer", In: Nemoto and LaManna (eds), *Oxygen Transport to Tissue XVIII*, 243-253, Plenum Press, New York, 1997.
- ³ P. Vaupel, "Oxygen transport in tumors: Characteristics and clinical implications", *Adv. Exp. Med. Biol.*, **388**, 341-351, 1996.
- ⁴ R. H. Thomlinson, and L. H. Gray, "The histological structure of some human lung cancers and the possible implications for radiotherapy", *Br. J. Cancer*, **9**, 539-549, 1955.
- ⁵ B. Teicher, J. Lazo, and A. Sartorelli, "Classification of antineoplastic agents by their selective toxicities toward oxygenated and hypoxic tumor cells", *Cancer Res.*, **41**, 73-81, 1981.
- ⁶ J. D. Chapman, C. C. Stobbe, M. R. Arnfield, R. Santus, J. Lee, and M. S. McPhee, "Oxygen dependency of tumor cell killing *in vitro* by light activated photofrin II", *Radiat. Res.*, **126**, 73-79, 1991.
- ⁷ A. W. Fyles, M. Milosevic, R. Wng, M. C. Kavanagh, M. Pintile, A. Sun, W. Chapman, W. Levin, L. Manchul, T. J. Keane, and R. P. Hill, "Oxygenation predicts radiation response and survival in patients with cervix cancer", *Radiother. Oncol.*, **48**, 149-156, 1998.
- ⁸ J. H. Kaanders, J. Bussink, and A. J. van der Kogel, "ARCON: a novel biology-based approach in radiotherapy", *Lancet Oncol.*, **3**(12), 728-37, 2002.
- ⁹ R. J. Gillies, P. A. Schornack, T. W. Secomb, and N. Raghunand, "Causes and effects of heterogeneous perfusion in tumors," *Neoplasia*, **1** (3), 197-207, 1999.
- ¹⁰ D. R. Taylor, H. Poptani, J. D. Glickson, J. S. Leigh, and R. Reddy, "High-Resolution Assessment of Blood Flow in Murine RIF-1 Tumors by Monitoring Uptake of H₂ ¹⁷O With Proton T₁ρ-Weighted Imaging," *Magn. Reson. Med.*, **49**, 1-6, 2003.
- ¹¹ J. C. Acker, M. W. Dewhirst, G. M. Honore, T. V. Samulski, J. A. Tucker, and J. R. Oleson, "Blood perfusion measurements in human tumors, evaluation of laser Doppler methods," *Int. J. Hypertherm.*, **6**, 287-304, 1990.
- ¹² J. Griebel, N. A. Mayr, A. de Vries, M. V. Knopp, T. Gneiting, C. Kremser, M. Essig, H. Hawighorst, P. H. Lukas, and W. T. Yuh, "Assessment of tumor microcirculation: a new role of dynamic contrast MR imaging," *J. Magn. Reson. Imaging*, **7**, 111-119, 1997.
- ¹³ M. W. Dewhirst, C. Gustafson, J. F. Gross, and C. Y. Tso, "Temporal effects of 5.0 Gy radiation in healing subcutaneous microvasculature of a dorsal flap window chamber", *Radiat. Res.*, **112**, 581-591, 1987.
- ¹⁴ R. P. Mason, A. Constantinescu, S. Hunjan, D. Le, E. W. Hahn, P. P. Antich, C. Blum, and P. Peschke, "Regional tumor oxygenation and measurement of dynamic changes." *Radiat. Res.*, **152**, 239-249, 1999.
- ¹⁵ D. Zhao, A. Constantinescu, E. W. Hahn and R. P. Mason. "Tumor oxygenation dynamics with respect to growth and respiratory challenge: Investigation of the Dunning prostate R3327-HI tumor," *Radiat. Res.*, **156**(5), 510-520, 2001.
- ¹⁶ S. Hunjan, D. Zhao, A. Constantinescu, E. W. Hahn, P. Antich, and R. P. Mason, "Tumor oximetry: demonstration of an enhanced dynamic mapping procedure using fluorine-19 echo planar magnetic resonance imaging in the dunning prostate R3327-AT1 rat tumor," *Int. J. Radiat. Oncol. Biol. Phys.*, **49**, 1097-1108, 2001.
- ¹⁷ M. Höckel, P. Vaupel, "Tumor hypoxia: definitions and current clinical, biologic, and molecular aspects", *J Natl Cancer Inst.*, **93**, 266-76, 2001.

- ¹⁸ B. Chance, S. Nioka, J. Kent, K. McCully, M. Fountain, R. Greenfield, and G. Holtom, "Time resolved spectroscopy of hemoglobin and myoglobin in resting and ischemic muscle", *Anal. Biochem.*, **174**,698-707, 1988.
- ¹⁹ S. Homma, T. Fukunaga, and A. Kagaya, "Influence of adipose tissue thickness on near infrared spectroscopic signals in the measurement of human muscle", *J. Biomed. Opt.*, **1**(4), 418-424, 1996.
- ²⁰ M. Ferrari, Q. Wei, L. Carraresi, R. A. De Blasi, and G. Zaccanti, "Time-resolved spectroscopy of the human forearm", *J. Photochem. Photobiol. B: Biol.*, **16**,141-153, 1992.
- ²¹ B. Chance, E. Anday, S. Nioka, S. Zhou, L. Hong, K. Worden, C. Li, T. Murray, Y. Ovetsky, D. Pidikiti, and R. Thomas, "A novel method for fast imaging of brain function non-invasively with light", *Optics Express*, **2**(10), 411-423 1998.
- ²² R. Wenzel, H. Obrig, J. Ruben, K. Villringer, A. Thiel, J. Bernarding, U. Dirnagl, and A. Villringer, "Cerebral blood oxygenation changes induced by visual stimulation in humans", *J. Biomed. Opt.*, **1**(4),399-404, 1996.
- ²³ M. Cope, and D. T. Delpy, "A system for long term measurement of cerebral blood and tissue oxygenation in newborn infants by near infrared transillumination", *Med. Biol. Eng. Comp.*, **26**, 289-294, 1988.
- ²⁴ R. G. Steen, K. Kitagishi, and K. Morgan, "In vivo measurement of tumor blood oxygenation by near-infrared spectroscopy: immediate effects of pentobarbital overdose or carmustine treatment", *J. Neuro-Oncol.*, **22**, 209-220, 1994.
- ²⁵ H. D. Sostman, S. Rockwell, A. L. Sylvia, D. Madwed, G. Cofer, H. C. Charles, R. Negro-Vilar, and D. Moore, "Evaluation of BA1112 rhabdomyosarcoma oxygenation with microelectrodes, optical spectrophotometry, radiosensitivity, and magnetic resonance spectroscopy", *Magn. Reson. Med.*, **20**, 253-267, 1991.
- ²⁶ H. Liu, Y. Song, K. L. Worden, X. Jiang, A. Constantinescu, and R. P. Mason, "Noninvasive Investigation of Blood Oxygenation Dynamics of Tumors by Near-Infrared Spectroscopy", *Applied Optics*, **39**(28), 5231-5243, 2000.
- ²⁷ T. Y. Reynolds, S. Rockwell, and P. M. Glazer, "Genetic instability induced by the tumor microenvironment," *Cancer Res.*, **56**, 5754-5757, 1996.
- ²⁸ Jae G. Kim, Dawen Zhao, Yulin Song, Anca Constantinescu, Ralph P. Mason, and Hanli Liu, "Interplay of tumor vascular oxygenation and tumor pO₂ observed using near-infrared spectroscopy, an oxygen needle electrode, and ¹⁹F MR pO₂ mapping", accepted for *J. Biomed. Opt.*, Jan 2003.
- ²⁹ M. Cope, "The application of near infrared spectroscopy to non invasive monitoring of cerebral oxygenation in the newborn infant", PhD thesis, University College London, 1991.
- ³⁰ R. G. Steen, K. Kitagishi and K. Morgan, "In vivo measurement of tumor blood oxygenation by near-infrared spectroscopy: Immediate effects of pentobarbital overdose or carmustine treatment", *J. Neuro-Oncol.*, **22**, 209-220, 1994.
- ³¹ S. S. Kety, "Cerebral circulation and its measurement by inert diffusible racers," *Israel J. Med. Sci.*, **23**, 3-7, 1987.

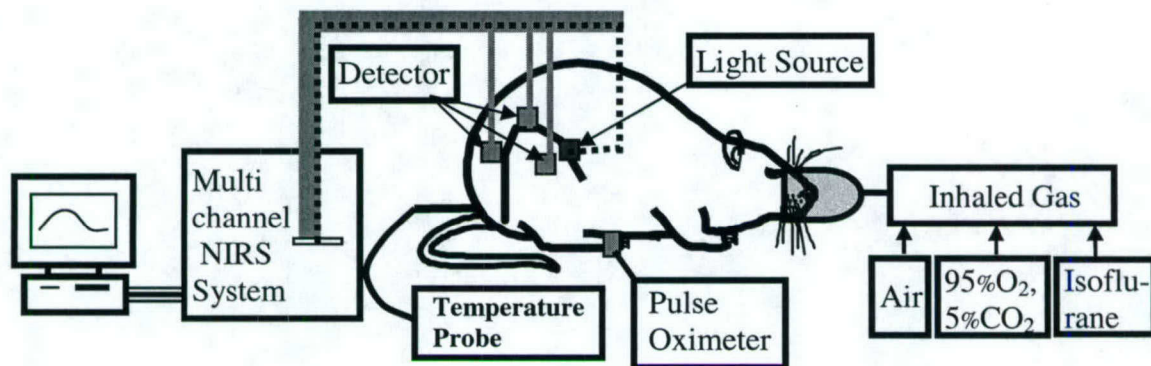


Figure 1

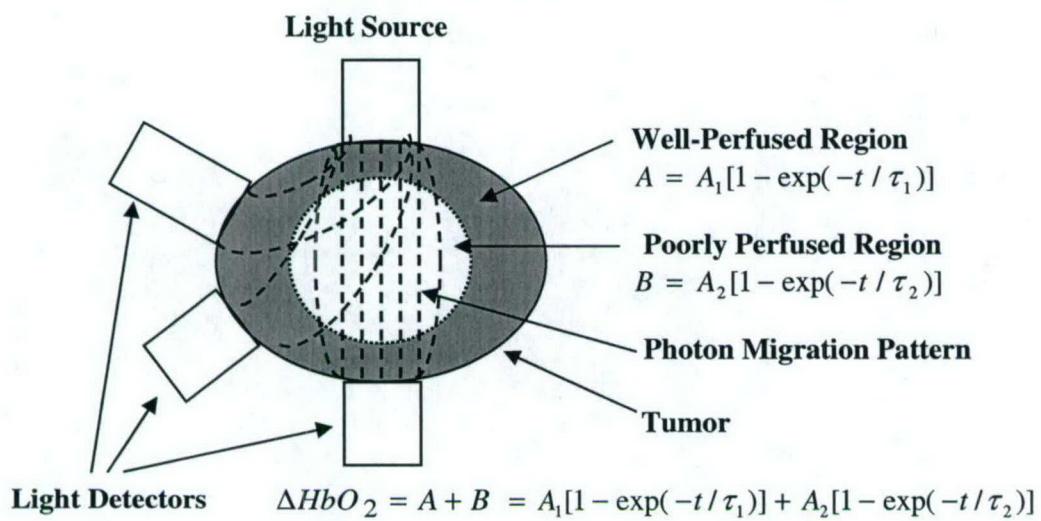


Figure 2

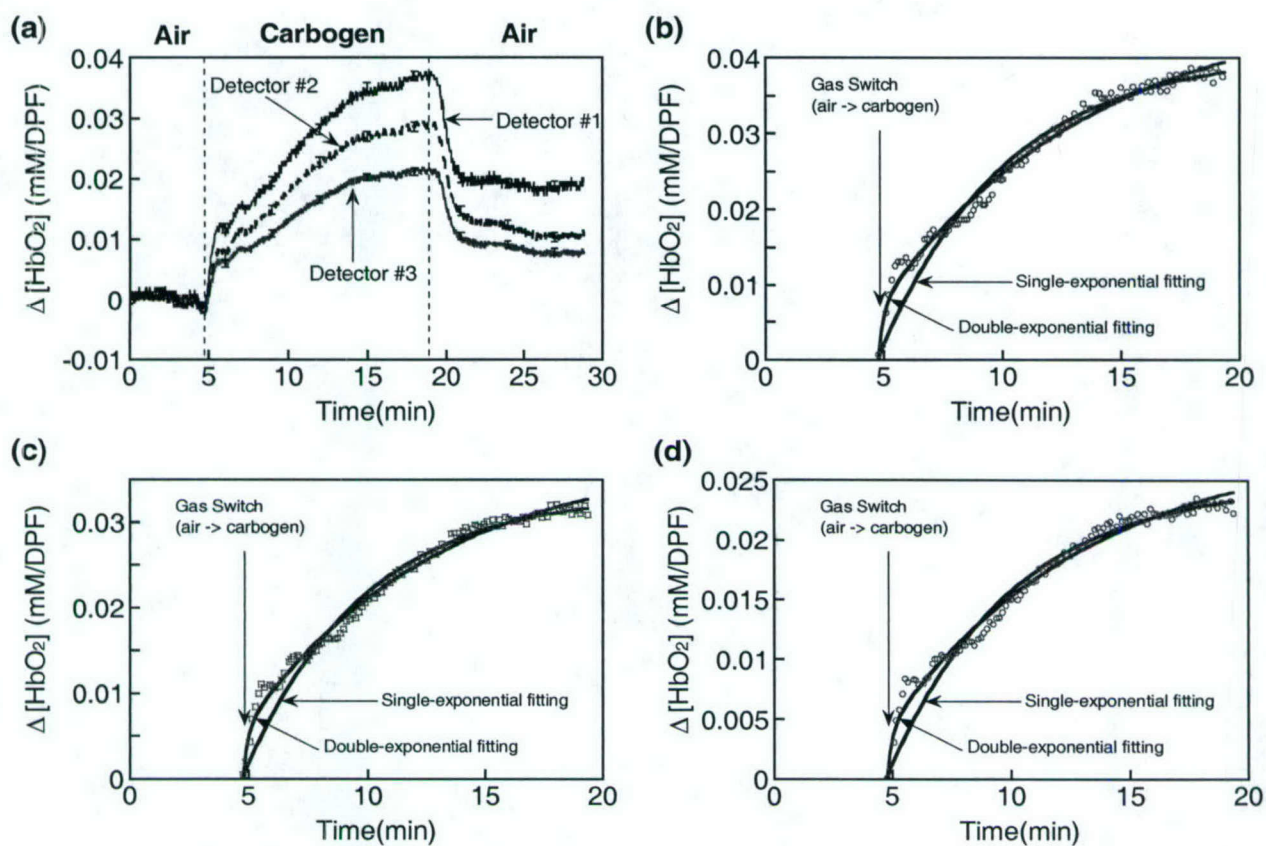


Figure 3

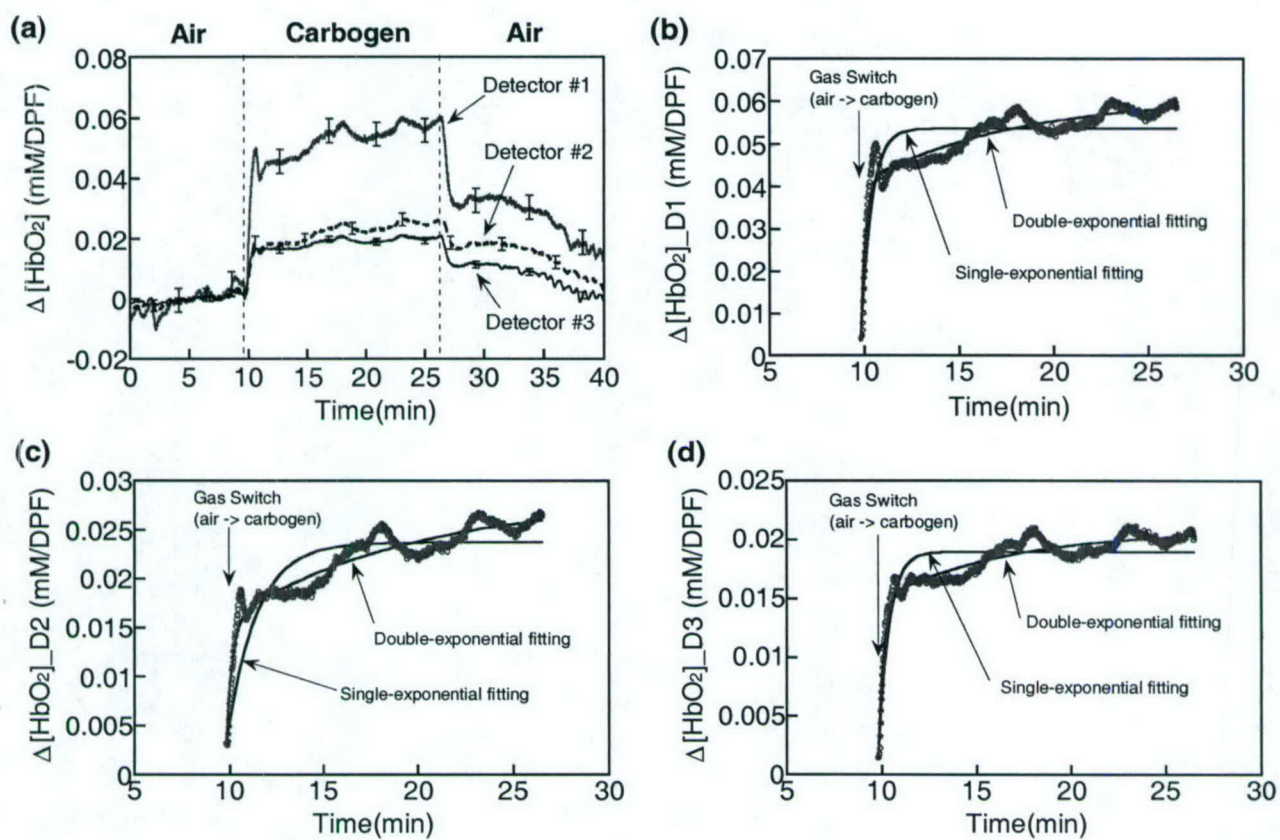


Figure 4

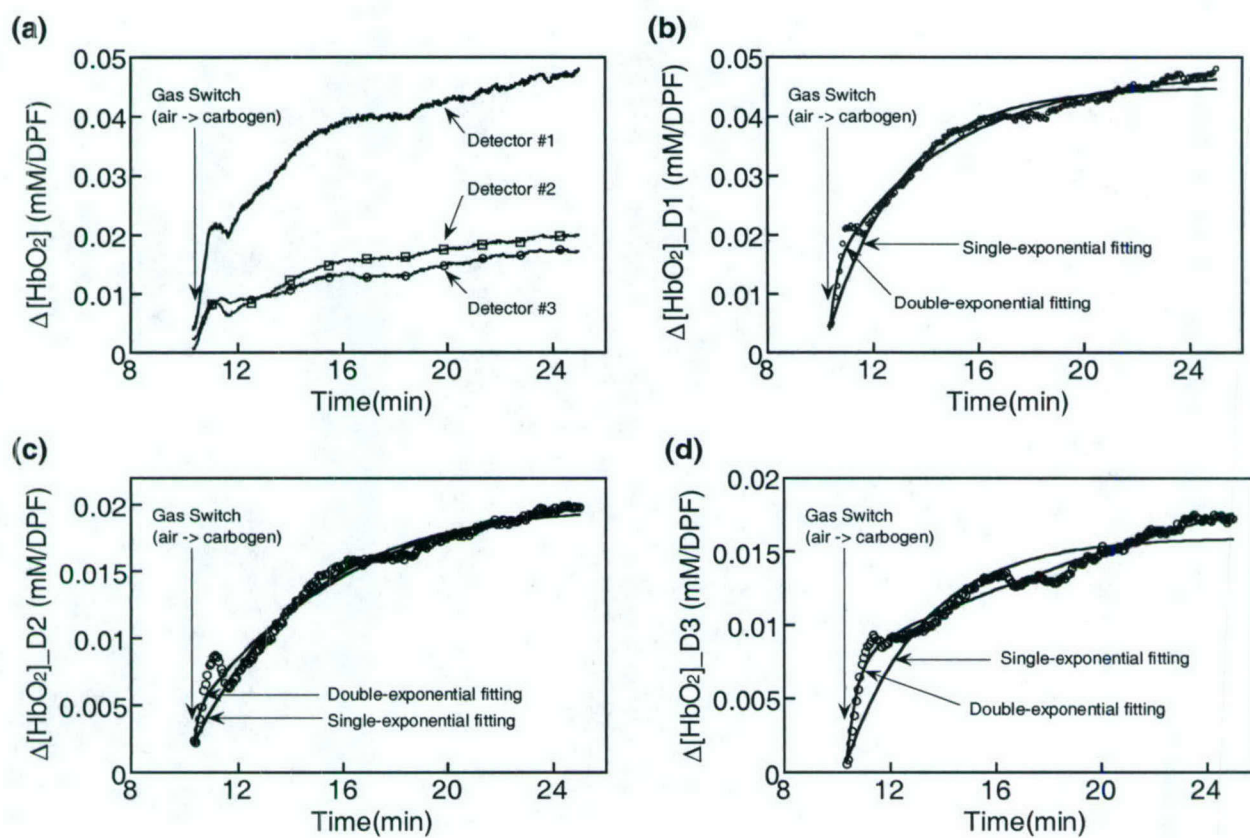


Figure 5

Dynamic response of breast tumor oxygenation to hyperoxic respiratory challenge monitored with three oxygen-sensitive parameters

Yueqing Gu, Vincent A. Bourke, Jae G. Kim, Anca Constantinescu, Ralph P. Mason, and Hanli Liu

The simultaneous measurement of three oxygen-sensitive parameters [arterial hemoglobin oxygen saturation (SaO_2), tumor vascular-oxygenated hemoglobin concentration ($[\text{HbO}_2]$), and tumor oxygen tension (pO_2)] in response to hyperoxic respiratory challenge is demonstrated in rat breast tumors. The effects of two hyperoxic gases [oxygen and carbogen (5% CO_2 and 95% O_2)] were compared, by use of two groups of Fisher rats with subcutaneous 13762NF breast tumors implanted in pedicles on the foreback. Two different gas-inhalation sequences were compared, i.e., air-carbogen-air-oxygen-air and air-oxygen-air-carbogen-air. The results demonstrate that both of the inhaled, hyperoxic gases significantly improved the tumor oxygen status. All three parameters displayed similar dynamic response to hyperoxic gas interventions, but with different response times: the fastest for arterial SaO_2 , followed by biphasic changes in tumor vascular $[\text{HbO}_2]$, and then delayed responses for pO_2 . Both of the gases induced similar changes in vascular oxygenation and regional tissue pO_2 in the rat tumors, and changes in $[\text{HbO}_2]$ and mean pO_2 showed a linear correlation with large standard deviations, which presumably results from global versus local measurements. Indeed, the pO_2 data revealed heterogeneous regional response to hyperoxic interventions. Although preliminary near-infrared measurements had been demonstrated previously in this model, the addition of the pO_2 optical fiber probes provides a link between the noninvasive relative measurements of vascular phenomena based on endogenous reporter molecules, with the quantitative, albeit, invasive pO_2 determinations. © 2003 Optical Society of America

OCIS codes: 170.1470, 170.3660, 170.4580, 120.3890, 120.1880, 230.2090.

1. Introduction

It is widely recognized that hypoxic regions in solid tumors may limit the efficacy of nonsurgical therapy, including radiotherapy, photodynamic therapy, and chemotherapy.¹⁻⁴ Many adjuvant interventions have been tested, including simple strategies such as breathing hyperoxic gases.⁵⁻⁷ However, a meta-analysis of some 10,000 patients showed only a modest benefit, and this benefit was restricted to specific tumor types.⁸ It is thought that the failure of such interventions was largely due to the inability to iden-

tify those patients who would benefit. Indeed, there is growing emphasis on tailoring therapy to the individual characteristics of each patient's tumor. Furthermore, carbogen (5% CO_2 and 95% O_2) and oxygen have been used on experimental tumors in animals as well as on clinical trials in patients for many years.^{9,10} But the therapeutic benefits of the two kinds of respiratory hyperoxic gases are diverse, depending on the tumor types and individuals.¹¹⁻¹³ Accordingly, accurate assessment of tumor oxygenation at various stages of tumor growth and in response to interventions may provide a better understanding of tumor development and may serve as a prognostic indicator for treatment outcome, potentially allowing therapy to be tailored to individual characteristics.

Various techniques have been developed to measure oxygen tension (pO_2) or vascular oxygenation of tumors.¹⁴ Many methods are invasive, and those requiring biopsy preclude dynamic investigations. Optical techniques based on light absorption of endogenous chromophores, e.g., near-infrared (NIR)

Y. Gu, J. G. Kim, and H. Liu (Hanli@uta.edu) are with the Biomedical Engineering Program, The University of Texas at Arlington, Arlington, Texas 76019. V. A. Bourke, A. Constantinescu, and R. P. Mason are with the Department of Radiology, University of Texas Southwestern Medical Center, Dallas, Texas 75390.

Received 8 September 2002; revised manuscript received 15 January 2003.

0003-6935/03/162960-08\$15.00/0

© 2003 Optical Society of America

spectroscopy of oxygenated and deoxygenated hemoglobin, are entirely noninvasive and allow real-time monitoring of tumor vascular oxygenation.^{15–17} However, NIR has limited spatial resolution, and it remains to be determined whether vascular oxygenation is related to therapeutic outcome. Hitherto, quantitative pO_2 has been shown to have prognostic value,^{18–21} but pO_2 represents a balance between oxygen delivery and consumption. Thus, we seek to explore the interplay of vascular and tissue oxygenation. Electrodes have been used widely to study tumor oxygen dynamics with respect to interventions,^{22–24} but they are generally limited to a single location and small probes can be fragile. We have ourselves recently shown a correlation between pO_2 and ΔHbO_2 in some tumors, but we noted distinct heterogeneity, and thus, the global NIR measurements were not always related to local pO_2 .²⁵ Multiple fiber-optic probes may be inserted into a tumor,^{26–28} and we have now investigated correlation between NIR measurements and multiple (three) simultaneous pO_2 measurements.

We now report simultaneous measurements of three oxygen-related parameters, i.e., arterial hemoglobin oxygen saturation, SaO_2 ; tumor oxygenated hemoglobin concentration, $[HbO_2]$; and tumor oxygen tension, pO_2 , to assess dynamic responses of rat breast tumors to hyperoxic gases. Changes in tumor vascular $[HbO_2]$ were measured by NIR spectroscopy (NIRS) using a photon-migration, frequency-domain device; changes in regional pO_2 were monitored by a fluorescence-quenched, oxygen-sensing, fiber-optic system (FOXY); the arterial SaO_2 values were recorded with a fiber-based, pulse oximeter.

2. Materials and Methods

A. Near-Infrared Spectroscopy System for Measurement of Changes in $[HbO_2]$

NIR light (700 to 900 nm) has considerable tissue penetration depth (several centimeters) and permits *in vivo* sampling of large tissue volumes (e.g., human breast, brain, skeletal muscle, or tumors), since photon transport in tissue is dominated by scattering rather than by absorption. Absorption of NIR light by the oxygenated and the deoxygenated hemoglobin chromophores may be used to determine hemoglobin oxygenation and blood concentration changes. As described in detail previously,^{16,25} a homodyne frequency-domain system (NIM, Philadelphia, Pennsylvania) was used to monitor the global changes in oxygenated and deoxygenated hemoglobin concentrations, $\Delta[HbO_2]$ and $\Delta[Hb]$, respectively, in rat breast tumors in response to variations in inhaled gas. Briefly, the light from two NIR laser diodes (758 nm and 785 nm) was coupled into a bifurcated fiber bundle and illuminated on the tumor, and the transmitted light was collected and propagated to a photomultiplier tube (Fig. 1). The fiber bundles were placed on the surface of the tumors in a transmittance mode parallel to the body of the rat. The fiber tips touched firmly on the skin (without com-

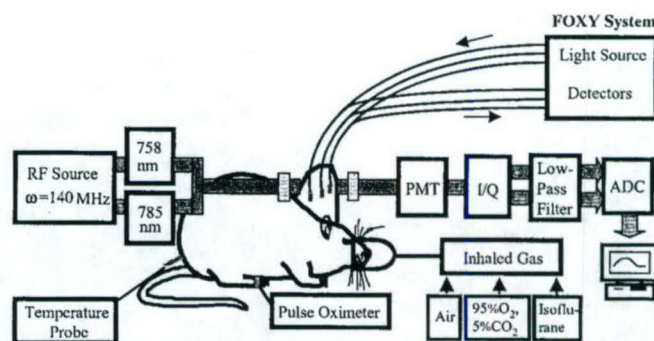


Fig. 1. Experimental setup for simultaneous oximetry. The 3-mm-diameter fiber bundles of the NIRS system deliver and detect the laser light through the tumor in transmittance geometry. PMT represents a photomultiplier tube. I/Q is an in-phase and quadrature phase demodulator for retrieving amplitude and phase information. The FOXY system comprises three fiber-optic oxygen-sensing probes that are inserted into different regions of the tumor. The pulse oximeter probe is placed on the hind foot of the rat.

pression) in the middle parts of the tumors, providing optimal geometry to interrogate deep tumor tissue.

Based on modified Beer–Lambert's law,²⁹ changes in oxygenated and deoxygenated hemoglobin concentrations, $\Delta[HbO_2]$ and $\Delta[Hb]$, due to respiratory intervention were derived from the measured amplitudes at the two wavelengths and calculated with the following equations²⁵:

$$\Delta[HbO_2] = \frac{-10.63 \log\left(\frac{A_B}{A_T}\right)^{758} + 14.97 \log\left(\frac{A_B}{A_T}\right)^{785}}{d}, \quad (1)$$

$$\Delta[Hb] = \frac{8.95 \log\left(\frac{A_B}{A_T}\right)^{758} - 6.73 \log\left(\frac{A_B}{A_T}\right)^{785}}{d}, \quad (2)$$

where A_B and A_T are the baseline and transient amplitudes measured from the NIR system, respectively; d is the source–detector separation; the unit for both $\Delta[HbO_2]$ and $\Delta[Hb]$ is millimolar per differential path-length factor (DPF); and the DPF is for tumor tissues. As demonstrated in our previous study, normalization of $\Delta[HbO_2]$ and $\Delta[Hb]$ to their maximal values can eliminate the effects of d and DPF on the results.²⁵

B. Fiber-Optic Oxygen-Sensing System for Measurement of Changes in pO_2

Regional pO_2 in tumors was monitored with a multichannel, fiber-optic, oxygen-sensing system (FOXY, Ocean Optics, Inc., Dunedin, Florida).³⁰ Three fluorescence-quenched, optical fiber probes (AL300, tip diameter 410 μm) were inserted into different regions of the tumors (Fig. 1). Probes were positioned so that at least one was in a poorly oxygenated region (low baseline pO_2) and at least one in a well-oxygenated region (high baseline pO_2). If necessary,

the probes were gently moved through the tumor until such diverse regions were located. In some cases, the mean pO_2 derived from the three individual measurements is presented. Although this is a commercial system, few details have been published previously,³¹ and no applications to *in vivo* tumor oximetry have been published to our knowledge. Light from a pulsed blue LED (475 nm) was coupled into one branch of a bifurcated optical fiber bundle and propagated to the probe tip. The distal end of the probe is coated with a thin layer of a hydrophobic solgel material, where an oxygen-sensing ruthenium complex is effectively trapped. Illumination of the ruthenium complex causes fluorescence at ~ 600 nm. If the excited ruthenium complex encounters an oxygen molecule, the excess energy is transferred to the oxygen molecule in a nonradiative transition, decreasing or quenching the fluorescence signal. The degree of quenching correlates with the oxygen concentration, and hence, pO_2 .

The fluorescence response of the ruthenium crystal complex is highly temperature dependent, so to accomplish probe calibration it was necessary to stream gases of known oxygen concentrations (100%, 20.9%, 10%, 2%, and 0%) through a cylindrical water jacket heated to 37 °C. Calibration curves were automatically calculated by means of the vendor-supplied software, with the second-order, polynomial calibration:

$$\frac{I_0}{I} = 1 + K_1[O] + K_2[O]^2 \quad (3)$$

where, I_0 is the fluorescence intensity at zero oxygen concentration (nitrogen), I is the measured intensity of fluorescence at a pressure of oxygen, $[O]$ represents the oxygen concentration (related to pO_2), K_1 and K_2 are the first- and the second-order coefficients and are automatically supplied by the curve-fitting routine from the calibration measurements.

C. Pulse Oximeter for Measurement of Arterial S_aO_2

Arterial S_aO_2 of the breast-tumor-bearing rats was also monitored with a fiber-optic pulse oximeter (Nonin Medical, Inc., Plymouth, Minnesota) placed on the hind foot of the rats. The system consisted of two optical fibers used for delivering and receiving the light. The tips were placed on either side of the foot in transmission mode.

D. Animal Model

Mammary adenocarcinomas 13762NF (originally obtained from the Division of Cancer Therapeutics, NIH, Bethesda, Maryland) were implanted in skin pedicles³² on the foreback of adult female Fisher 344 rats (~ 150 g). Once the tumors reached 1–2 cm diameter, rats were anesthetized with 150- μ l ketamine hydrochloride (100 mg/ml, i.p.) and maintained under general gaseous anesthesia with 1.3% isoflurane in air (1 dm³/min). Body temperature was maintained at 37 °C by a warm water blanket. Tumors were shaved to improve optical contact for transmitting NIR light. The tumor diameters along the

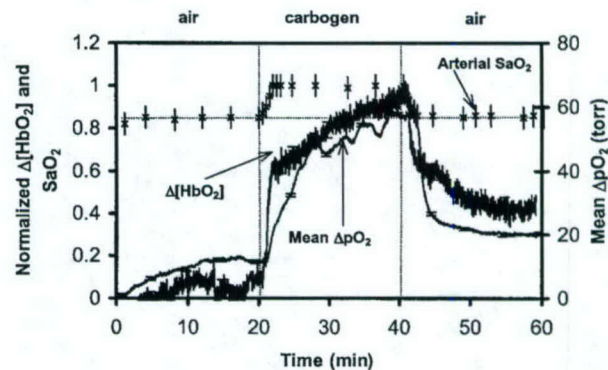


Fig. 2. Time profile of the three oxygen-sensitive parameters, i.e., the normalized changes of tumor $\Delta[HbO_2]$, the mean changes of tumor ΔpO_2 , and the arterial S_aO_2 with respect to carbogen breathing in a representative 13762NF rat breast tumor (No. 1, 3.2 cm³).

three major orthogonal axes (a , b , c) were measured with calipers and volume estimated with an ellipsoid approximation with the formula: $V = (\pi/6)(abc)$.

Two groups of rats ($n = 7$ in each group) were used to compare the effects of carbogen and oxygen on vascular oxygenation of breast tumors. Group 1 experienced the gas-inhalation sequence of air–carbogen–air–oxygen–air. Group 2 was exposed to the reverse sequence of air–oxygen–air–carbogen–air. Each gas was maintained for 20 min. In addition, the FOXY pO_2 probes were applied to five rats from Group 1, and the dynamics of the three oxygen-related parameters were measured simultaneously.

3. Results

A. Dynamic Responses of Three Oxygen-Related Parameters to Carbogen Intervention

Typical time profiles of the normalized $\Delta[HbO_2]$, mean ΔpO_2 , and S_aO_2 in response to carbogen intervention are shown for a representative 13762NF breast tumor (No. 1, 3.2 cm³) in Fig. 2. When the inspired gas was switched from air to carbogen, the S_aO_2 readings increased rapidly and significantly from the baseline value of 85% to the maximum of 100% within 2.5 minutes ($p < 0.0001$). The normalized $\Delta[HbO_2]$ showed a sharp initial rise in the first minute ($p < 0.0001$) followed by a slower, gradual, but further significant increase over the next 19 min ($p < 0.001$). Mean ΔpO_2 increased rapidly by approximately 50 Torr within 8 min ($p < 0.0005$) and also continued a slower and gradual increase over the next 12 min ($p < 0.005$). Return to breathing air produced a significant decline for all three signals ($p < 0.0001$).

S_aO_2 and pO_2 displayed a single-phase dynamic behavior in response to carbogen intervention, whereas $\Delta[HbO_2]$ showed an apparent biphasic response. These dynamics may be characterized by time constants of a single-exponential response. For the tumor in Fig. 3, S_aO_2 had the fastest response, with a time constant of $\tau(S_aO_2) = 1.1 \pm 0.2$ min ($R =$

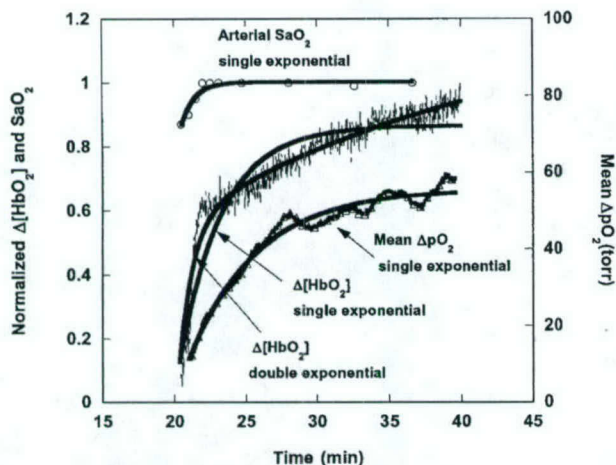


Fig. 3. Dynamic responses of the three oxygen-sensitive parameters to carbogen intervention in a rat breast tumor (No. 1, 3.2 cm³). Single-exponential curve fitting yielded $SaO_2 = 0.204\{1 - \exp[-(t - 20.02)/1.1]\} + 0.85$ ($R = 0.93$), $\Delta[HbO_2] = 0.655\{1 - \exp[-(t - 20.36)/2.59]\} + 0.125$ ($R = 0.89$), and $\Delta pO_2 = 42.68\{1 - \exp[-(t - 21.01)/4.56]\} + 16.66$ ($R = 0.98$); biexponential fitting resulted in $\Delta[HbO_2] = 0.373\{1 - \exp[-(t - 20.36)/0.61]\} + 0.648\{1 - \exp[-(t - 20.36)/21]\}$ ($R = 0.97$).

0.93), followed by $[HbO_2]$ with $\tau(\Delta[HbO_2]) = 2.59 \pm 0.06$ min ($R = 0.89$), whereas ΔpO_2 yielded the slowest response $\tau(\Delta pO_2) = 4.56 \pm 0.06$ min ($R = 0.98$). Time constants for Group 1 are listed in Table 1. In every case $\tau(SaO_2) < \tau(\Delta[HbO_2]) < \tau(\Delta pO_2)$, based on the single-exponential fitting. No apparent relation between the time constant and the tumor volume was observed.

It is clear that the response of $\Delta[HbO_2]$ is not well represented by a single exponential, and thus, a double-exponential expression with two time constants, τ_1 and τ_2 , was also used (Fig. 3). Comparison between the biexponential fitting for $\Delta[HbO_2]$ and the single-exponential results for both SaO_2 and ΔpO_2 in the first five rat tumors (Table 1) shows that the time constants of SaO_2 ($\sim 1.2 \pm 0.4$ min) are similar to those of the first phase of $\Delta[HbO_2]$ ($\sim 0.5 \pm 0.2$ min), whereas the second phase is longer and highly vari-

able ($\sim 14 \pm 11$ min). No significant correlations were found between any of the time constants in Table 1.

Time delay, t_d , between the time when the gas intervention was initiated and the time when the changes in signals were detected, reveals another difference among the three oxygen-sensitive parameters. For tumor 1 (Fig. 2), the SaO_2 signal was the first to respond to the intervention. Change in $\Delta[HbO_2]$ was observed 30 s later with $t_d = 30$ s, followed by changes in ΔpO_2 another 30 s later ($t_d = 60$ s). Similarly, when the gas was returned from carbogen to air, the SaO_2 signal decreased immediately, followed by declines in $\Delta[HbO_2]$ and in ΔpO_2 with t_d of 30 and 120 s later, respectively. As expected, changes in SaO_2 always preceded $\Delta[HbO_2]$, and ΔpO_2 occurred last for all tumors.

B. Comparison of the Effects of Carbogen and Oxygen Intervention on Tumor Oxygenation

Switching from air breathing to carbogen or oxygen produced similar changes in $\Delta[HbO_2]$ [Fig. 4(a)]. However, the time course was substantially different, requiring a biphasic exponential fit for carbogen, but a single exponential for oxygen [Fig. 4(b)]. For the seven tumors in Group 1, there was no significant difference ($p > 0.3$) in the maximum magnitude of $\Delta[HbO_2]$ caused by carbogen or oxygen interventions [Fig. 4(c)].

To examine the possible effect of preconditioning required that Group 2 experience a reversed gas intervention, with exposure to oxygen prior to carbogen [Fig. 5(a)]. In this case, the time constants of the normalized tumor vascular $\Delta[HbO_2]$ were now similar for both gas challenges: indeed, for six of seven tumors, carbogen no longer induced the biphasic behavior. Figure 5(b) shows that changes in $(\Delta[HbO_2])_{\max}$ were similar to those in Group 1, and again, the two gases did not produce significantly different response in $(\Delta[HbO_2])_{\max}$. This is emphasized for both Groups 1 and 2 by a strong linear correlation (slope $\cong 1.16$) between the $\Delta[HbO_2]_{\max}$ values observed in response to each of the two con-

Table 1. Time Constants of SaO_2 , $\Delta[HbO_2]$, and ΔpO_2 Response to Carbogen and Oxygen Intervention in the Breast Tumors^a

Breast Tumors Volume (cm ³)	Single-Exponential Fitting of SaO_2 , $\Delta[HbO_2]$ and ΔpO_2 (Carbogen Intervention)						Double-Exponential Fitting for $\Delta[HbO_2]$ (Carbogen Intervention)			Single-Exponential Fitting of $\Delta[HbO_2]$ (O ₂ Intervention)	
	SaO_2		$\Delta[HbO_2]$		ΔpO_2		$\Delta[HbO_2]$ (Carbogen Intervention)			$\Delta[HbO_2]$ (O ₂ Intervention)	
	τ (min)	R	τ (min)	R	τ (min)	R	τ_1 (min)	τ_2 (min)	R	τ (min)	R
No. 1 (3.2)	1.1 \pm 0.2	0.93	2.59 \pm 0.06	0.89	4.56 \pm 0.04	0.98	0.61 \pm 0.03	21 \pm 3	0.97	0.35 \pm 0.01	0.92
No. 2 (3.0)	1.6 \pm 0.2	0.98	3.40 \pm 0.07	0.91	4.6 \pm 0.1	0.82	0.62 \pm 0.06	11 \pm 1	0.96	0.51 \pm 0.01	0.91
No. 3 (4.6)	1.2 \pm 0.2	0.97	2.12 \pm 0.06	0.76	2.26 \pm 0.02	0.98	0.6 \pm 0.1	37 \pm 3	0.96	1.52 \pm 0.02	0.89
No. 4 (2.6)	1.9 \pm 0.3	0.98	2.68 \pm 0.05	0.93	3.5 \pm 0.1	0.86	0.12 \pm 0.02	5.2 \pm 0.1	0.98	1.71 \pm 0.03	0.94
No. 5 (5.6)	0.8 \pm 0.2	0.91	2.68 \pm 0.05	0.74	4.51 \pm 0.02	0.99	0.17 \pm 0.03	12.5 \pm 0.6	0.99	5.49 \pm 0.03	0.98
No. 6 (1.9)	0.9 \pm 0.2	0.81	1.62 \pm 0.01	0.95	nd	/	0.63 \pm 0.08	2.3 \pm 0.1	0.96	5.16 \pm 0.06	0.93
No. 7 (0.72)	1.0 \pm 0.5	0.95	3.60 \pm 0.03	0.93	nd	/	0.61 \pm 0.02	10.5 \pm 0.3	0.98	3.54 \pm 0.03	0.95
Mean	1.2 \pm 0.4		2.7 \pm 0.6		4 \pm 1		0.5 \pm 0.2	14 \pm 11		2.5 \pm 2	

^aUnder the inhalation sequence of air-carbogen-air-oxygen-air.

^bnd, not determined.

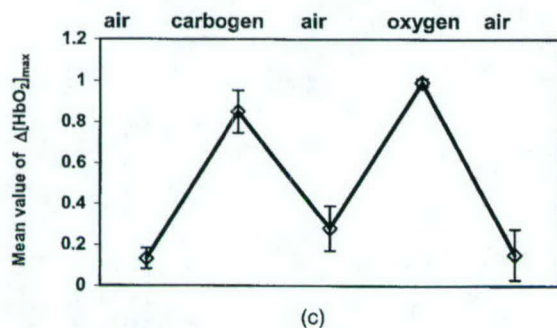
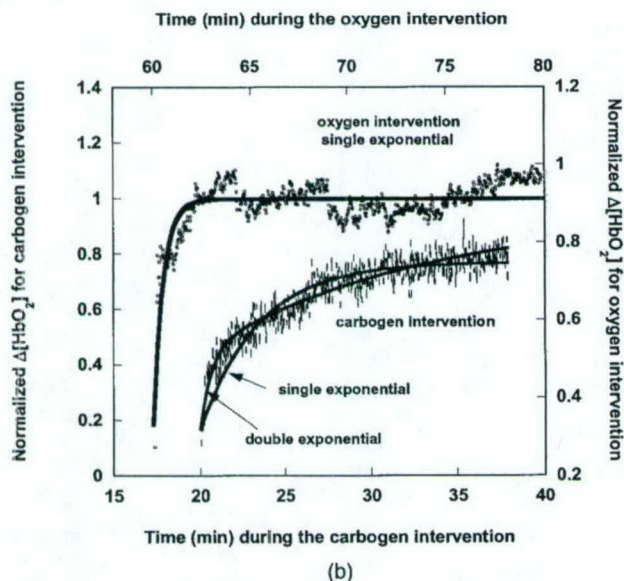
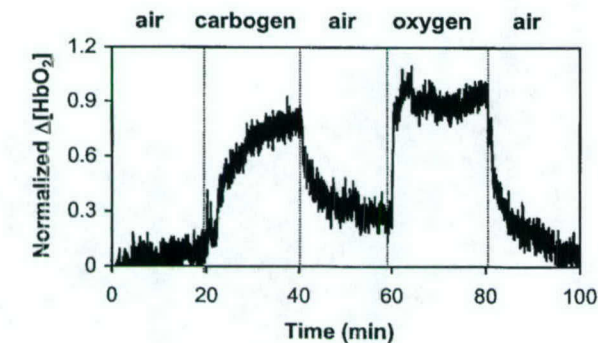


Fig. 4. (a) Time course of changes in tumor vascular $\Delta[\text{HbO}_2]$ for a representative 13762NF breast tumor from Group 1 (No. 2, 3.0 cm^3) with respect to altering inhaled gas. (b) Respective curve fits for the carbogen and oxygen interventions. (c) Average maximum values of normalized $\Delta[\text{HbO}_2]$ for the seven breast tumors in Group 1.

secutive interventions [Fig. 5(c)]. In this case, non-normalized data are shown for specific comparison of the absolute $\Delta[\text{HbO}_2]_{\text{max}}$ produced by oxygen and carbogen for each of the tumors.

C. Tumor pO_2

The FOXY pO_2 probes generally indicated distinct heterogeneity in pO_2 . Moreover, response to the hy-

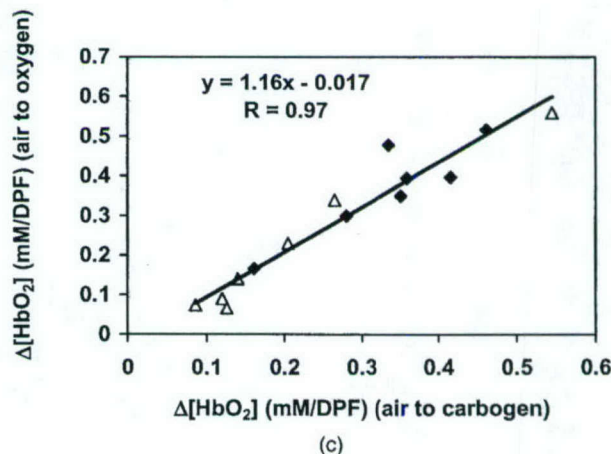
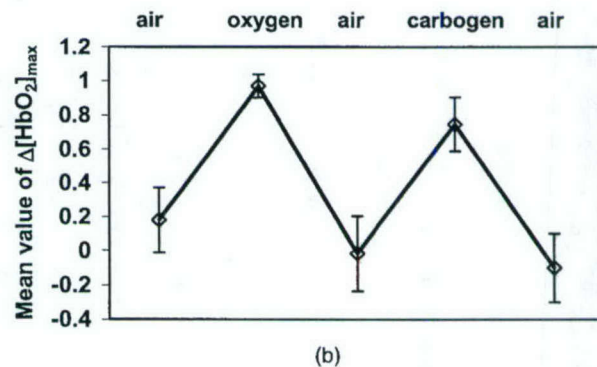
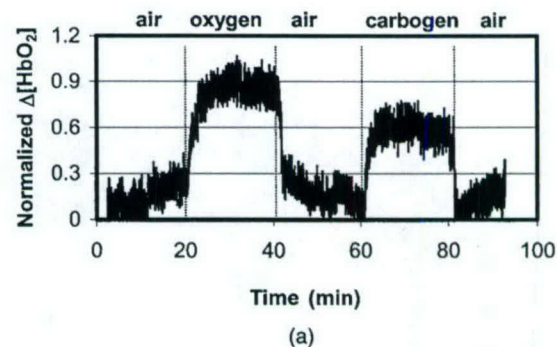


Fig. 5. (a) Dynamic changes in tumor vascular $\Delta[\text{HbO}_2]$ for a representative 13762NF breast tumor from Group 2 (No. 9, 2.6 cm^3) with gas-inhalation sequence reversed compared with Group 1. (b) Average maximum values of normalized $\Delta[\text{HbO}_2]$ for Group 2. Gas-inhalation sequence reversed compared with Group 1. (c) Correlation between maximum $\Delta[\text{HbO}_2]$ achieved with carbogen inhalation versus that with oxygen ($R = 0.97$): \blacklozenge , carbogen first; \triangle , oxygen first.

peroxic gas was diverse: those probes that indicated apparently well-oxygenated regions usually showed a large and rapid response, whereas those with lower baseline pO_2 often showed little change [Fig. 6(a)]. The pO_2 responses to the two interventions showed a highly consistent behavior at each individual location [Fig. 6(b)]. There was also a distinct correlation between the global NIR measurements and the mean ΔpO_2 (Fig. 7). Because of heterogeneity in regional pO_2 , the standard deviations of the mean pO_2 values were large.

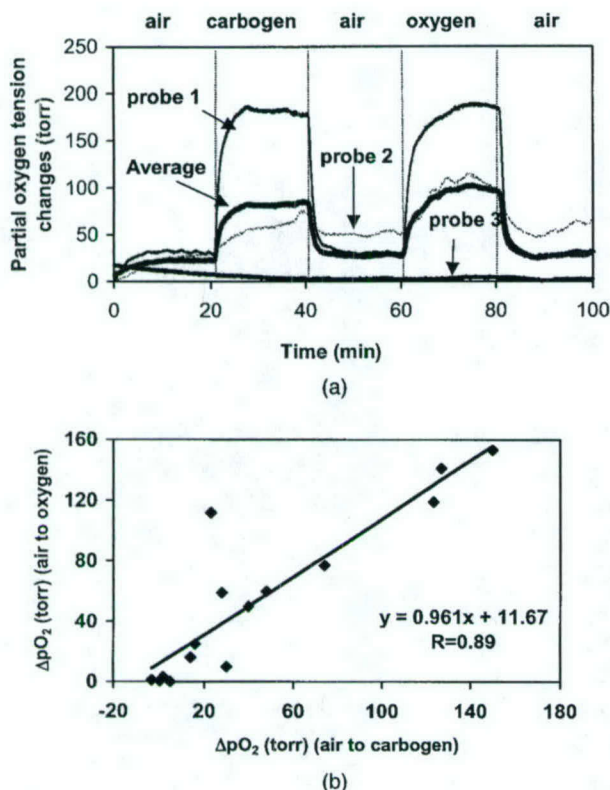


Fig. 6. (a) Time profiles of tumor ΔpO_2 , measured with the three channels of the FOXY fiber-optic, oxygen-sensing system with respect to different gas inhalations for breast tumor No. 3 (4.6 cm^3). The mean signal for the three channels was calculated and is plotted by the thicker trace. (b) Correlation between ΔpO_2 at individual locations in the tumors in response to carbogen or oxygen for the five tumors in Group 1 ($R > 0.8$).

4. Discussion

In this study, we have simultaneously measured the arterial SaO_2 , the global changes in the $\Delta[HbO_2]$ of tumor vasculature, and the regional changes in the ΔpO_2 of tumor tissue, in response to hyperoxic (i.e., carbogen and oxygen) gas interventions with a pulse oximeter, an NIRS system and a multichannel, fiber-optic, oxygen-sensing system, respectively. All three oxygen-sensitive indicators displayed similar

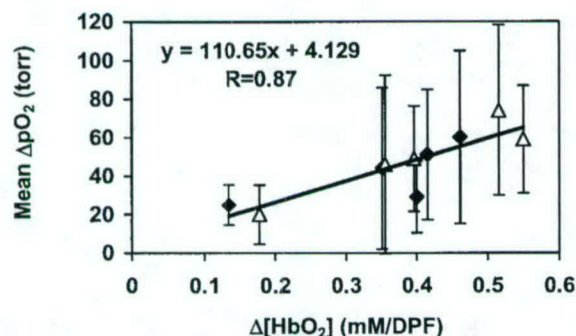


Fig. 7. Correlation between mean ΔpO_2 and $\Delta[HbO_2]$ for the five breast tumors ($R > 0.86$): \blacklozenge , transition from air to carbogen; \triangle , transition from air to oxygen.

dynamic tendency in response to carbogen intervention (Fig. 2).

The simultaneous measurements demonstrate the compatibility of the NIRS system with the FOXY fiber-optic oxygen-sensing system, without interference. Both systems are relatively inexpensive and provide real-time measurements, but the multichannel FOXY fiber-optic system monitors ΔpO_2 in specific locations, whereas the NIRS system provides global measurements. Whether ΔHbO_2 determined with this methodology will be a clinically useful predictor for tumor response to oxygen-dependent interventions and therapies remains to be determined. However, it is established that measurements of pO_2 have prognostic value in the clinic^{18,20} so that correlations between pO_2 and NIR measurements would be very important.

We have previously applied a polarographic oxygen electrode simultaneously with NIR.²⁵ However, that study provided only a single local pO_2 value, and in some cases correlations with global NIR measurements were very poor. The optical fiber system used here allows multiple locations to be interrogated simultaneously. The device can be expanded to many channels, but our system uses four channels. Unfortunately, probes are fragile, and the oxygen-sensitive coating on the tips is readily damaged. Thus, we only had three probes available for this study. Indeed, fiber-optic probe fragility is a well-recognized problem, and our previous experience with the more expensive OxyLite system was also restricted to three channels owing to probe damage.²⁶

The FOXY system ($\sim \$13k$) is much less expensive than the OxyLite ($\sim \$48k$), and its mode of action is also simpler, detecting fluorescent signal intensity rather than fluorescence lifetime. It seems capable of measuring pO_2 across the whole range of atmospheric oxygen tensions (0–760 Torr), whereas the OxyLite is restricted and becomes very insensitive above approximately 100 Torr. However, our experience shows that although the FOXY system provides precise measurements of ΔpO_2 , absolute values of pO_2 may not be reliable. We continue to perform validation experiments. By contrast, the OxyLite system seems to give very accurate pO_2 values.

Our experience shows that the FOXY probes are much easier to use than electrodes, particularly, in terms of calibration and stability. Since the probes are fragile, we insert them into tumors through a fine needle (25 gauge), which readily punctures the surrounding skin and penetrates tough fibrous tissues. The needle is then backed up from the tip to facilitate measurements. The probes often require a few minutes to settle at a stable baseline value, but then show good baseline stability and rapid response to interventions [Figs. 2 and 6(a)]. They are easily moved within the tumor to locate regions, presenting a particular pO_2 of interest, e.g. hypoxic or well oxygenated. In the search for appropriate locations, probes are moved forward to interrogate fresh tissues rather than in reverse, since blood may pool in the tracks owing to vascular damage. However, we observe

minimal bleeding on removal of the probes from the tumors.

We have found no interference between the NIR and FOXY instruments, although any tumor motion associated with moving the fiber probes can alter the optical contact of the NIR optrodes, and thus, alter apparent ΔHbO_2 . Thus, baseline ΔHbO_2 is determined once the fiber probes are situated. New fiber-optic probes of the FOXY system have a thick coating of fluorescent gel and a black covering, but this wears with use and gradually allows reception of the NIR light. Since the LEDs of the two systems operate at very different wavelengths, viz. 475 versus 760 nm, there is no interference for detection. The detection of local NIR light by the FOXY probe opens the exciting possibility of detecting regional hemoglobin oxygen saturation. We believe the FOXY optical probes could be moved within the tumor to map the distribution and path of the transmitted NIR light, helping to explore and validate the optical characteristics of the tumor. This can simultaneously provide a correlation between local ΔHbO_2 and ΔpO_2 .

In this study, we have examined a much larger group of rats than previously.^{16,25} We have now shown rigorously that the two hyperoxic gases induce similar changes in vascular oxygenation (NIR) and regional tissue pO_2 (FOXY) in this type of rat breast tumor. These data are consistent with our previous observations using ^{19}F NMR imaging (FREDOM)³³ in this tumor type and also in rat prostate tumors.^{34,35} If the two gases are indeed equivalent in terms of manipulation of tumor oxygenation, it could have great therapeutic benefit since the popular carbogen, which is in use in clinical trials,³⁶ can cause respiratory discomfort.

The current data show that ΔHbO_2 and ΔpO_2 are correlated (Fig. 7), and thus, such noninvasive observations could have value in the clinic. The major deficiency in our current NIR approach is lack of spatial discrimination, and thus efforts to implement NIR imaging will be of great value. It will also be interesting to correlate other measurements, such as blood-oxygen-level-dependent (BOLD) proton magnetic resonance imaging, which provide high spatial resolution, but which are sensitive to vascular flow and volume as well as oxygenation.³⁷

The biphasic response of ΔHbO_2 to carbogen is intriguing, and we believe it represents the distinct vascular compartments of arterioles (high flow) and capillaries. However, the change to monophasic behavior, when carbogen is administered second, requires further exploration; in the future, we propose to test various concentrations of oxygen and carbon dioxide and air to separate the components of the response. The carbogen dioxide component of carbogen is known to be vasoactive; however, the specific effects may depend on tumor type, site of growth, and other factors.^{9,38}

In terms of vascular oxygen delivery, the data in Table 1 reveal the progressive movement of oxygen: $t_d(\text{SaO}_2) < t_d(\Delta[\text{HbO}_2]) < t_d(\Delta\text{pO}_2)$. As expected, switching to hyperoxic gas caused the systemic arte-

rial SaO_2 to increase, as a result of the immediate combination of deoxyhemoglobin with oxygen. The highly oxygenated blood circulated in the systemic vasculature of the rats (including the capillary bed of the tumor tissue), resulting in a delayed increase in $[\text{HbO}_2]$ in the tumor vasculature, and led to an unloading of oxygen to the tumor tissue. For the biexponential model of $\Delta[\text{HbO}_2]$, the fast component has a similar time constant to the SaO_2 measured with the pulse oximeter on the hind leg, strongly suggesting that it represents arteriolar oxygenation in the tumor. In this study, tumor volumes do not show any direct relation with time constants or changes of amplitude in response to hyperoxic gas interventions.

It is increasingly evident that oxygen and hypoxia play important roles in tumor development and response to therapy.¹⁸ NIR offers an attractive non-invasive means of investigating tumor oxygenation, particularly in terms of dynamic response to interventions, but we had previously shown a potential mismatch between global ΔHbO_2 and local ΔpO_2 .²⁵ The data presented here indicate a correlation between the global NIR measurements and mean pO_2 values with even as few as three representative locations per tumor. This does suggest that it will be important to develop regional NIR measurements and that even relatively crude mapping could reveal heterogeneity. In the meantime, we believe these studies provide further evidence for the value of NIRS to explore tumor physiology.

This study was supported in part by the Department of Defense Breast Cancer Research grants BC000833 (YG) and BC990287 (HL), and NIH RO1 CA79515 (RPM) and RO1 supplement CA79515-S (VB). We are grateful to Mengna Xia and Dawen Zhao for their assistance with data processing. We gratefully acknowledge Weina Cui for helpful discussions.

References

1. R. S. Bush, R. D. T. Jenkin, W. E. C. Allt, F. A. Beale, A. J. Dembo, and J. F. Pringle, "Definitive evidence for hypoxic cells influencing cure in cancer therapy," *Br. J. Cancer* **37**(suppl 3), 302-306 (1978).
2. E. J. Hall, *Radiobiology for the Radiologist*, 4th ed. (Lippincott, Philadelphia, Pa., 1994).
3. M. Nordsmark and J. Overgaard, "A confirmatory prognostic study on oxygenation status and loco-regional control in advanced head and neck squamous cell carcinoma treated by radiation therapy," *Radiother. Oncol.* **57**, 39-43 (2000).
4. O. Thews, D. K. Kelleher, and P. Vaupe, "Erythropoietin restores the anemia-induced reduction in cyclophosphamide cytotoxicity in rat tumors," *Cancer Res.* **61**, 1358-1361 (2001).
5. J. H. A. M. Kaanders, L. A. M. Pop, H. A. M. Marres, R. W. M. van der Maazen, A. J. van der Kogel, and W. A. J. van Daal, "Radiotherapy with carbogen breathing and nicotinamide in head and neck cancer: feasibility and toxicity," *Radiother. Oncol.* **37**, 190-198 (1995).
6. M. I. Saunders, P. J. Hoskin, and K. Pigott, "Accelerated radiotherapy, carbogen and nicotinamide (ARCON) in locally advanced head and neck cancer: a feasibility study," *Radiother. Oncol.* **45**, 159-166 (1997).
7. J. A. Kruuv, W. R. Inch, and J. A. McCredie, "Blood flow and

- oxygenation of tumors in mice. I. Effects of breathing gases containing carbon dioxide at atmospheric pressure," *Cancer* **20**, 51–59 (1967).
8. J. Overgaard and M. R. Horsman, "Modification of hypoxia-induced radioresistance in tumors by the use of oxygen and sensitizers," *Semin. Radiat. Oncol.* **6**, 10–21 (1996).
9. P. Vaupel, D. K. Kelleher, and O. Thews, "Modulation of tumor oxygenation," *Int. J. Radiat. Oncol. Bio. Phys.* **42**, 843–848 (1998).
10. S. Dische, "What we learnt from hyperbaric oxygen?" *Radiother. Oncol.* **20**(Suppl.), 71–74 (1991).
11. S. Dische, M. I. Saunders, and R. Sealy, "Carcinoma of the cervix and the use of hyperbaric oxygen with radiotherapy: a report of a randomized controlled trial," *Radiother. Oncol.* **53**, 93–98 (1999).
12. V. M. Laurence, R. Ward, I. F. Dennis, and N. M. Bleehen, "Carbogen breathing with nicotinamide improves the oxygen status of tumors in patients," *Br. J. Cancer* **72**, 198–205 (1995).
13. L. Martin, E. Lartigau, and P. Weeger, "Changes in the oxygenation of head and neck tumors during carbogen breathing," *Radiother. Oncol.* **27**, 123–130 (1993).
14. H. B. Stone, J. M. Brown, T. Phillips, and R. M. Sutherland, "Oxygen in human tumors: correlations between methods of measurement and response to therapy," *Radiat. Res.* **136**, 422–434 (1993).
15. E. L. Hull, D. L. Conover, and T. H. Foster, "Carbogen induced changes in rat mammary tumor oxygenation reported by near infrared spectroscopy," *Br. J. Cancer* **79**, 1709–1716 (1999).
16. H. Liu, Y. Song, K. L. Worden, X. Jiang, A. Constantinescu, and R. P. Mason, "Noninvasive investigation of blood oxygenation dynamics of tumors by near-infrared spectroscopy," *Appl. Opt.* **39**, 5231–5243 (2000).
17. R. G. Steen, K. Kitagishi, and K. Morgan, "In vivo measurement of tumor blood oxygenation by near-infrared spectroscopy: immediate effects of pentobarbital overdose or carmustine treatment," *J. Neuro-Oncol.* **22**, 209–220 (1994).
18. M. Höckel and P. Vaupel, "Tumor hypoxia: definitions and current clinical, biologic, and molecular aspects," *J. Natl. Cancer Inst.* **93**, 266–276 (2001).
19. L. Gray, A. Conger, M. Ebert, S. Hornsey, and O. Scott, "The concentration of oxygen dissolved in tissues at time of irradiation as a factor in radio-therapy," *Br. J. Radiol.* **26**, 638–648 (1953).
20. A. W. Fyles, M. Milosevic, R. Wong, M. C. Kavanagh, M. Pintile, A. Sun, W. Chapman, W. Levin, L. Manchul, T. J. Keane, and R. P. Hill, "Oxygenation predicts radiation response and survival in patients with cervix cancer," *Radiother. Oncol.* **48**, 149–156 (1998).
21. D. Zhao, A. Constantinescu, E. W. Hahn, and R. P. Mason, "Measurement of tumor oxygen dynamics predicts beneficial adjuvant intervention for radiotherapy in Dunning prostate R3327-HI tumors," *Radiat. Res.* (to be published) (2003).
22. C. Song, I. Lee, T. Hasegawa, J. Rhee, and S. Levitt, "Increase in pO₂ and radiosensitivity of tumors by Fluosol and carbogen," *Cancer Res.* **47**, 442–446 (1987).
23. D. Cater and I. Silver, "Quantitative measurements of oxygen tension in normal tissues and in the tumors of patients before and after radiotherapy," *Acta Radiol.* **53**, 233–256 (1960).
24. D. Zhao, A. Constantinescu, E. W. Hahn, and R. P. Mason, "Differential oxygen dynamics in two diverse Dunning prostate R3327 rat tumor sublines (MAT-Lu and HI) with respect to growth and respiratory challenge," *Int. J. Radiat. Oncol. Biol. Phys.* **53**, 744–756 (2002).
25. J. G. Kim, Y. Song, D. Zhao, A. Constantinescu, R. P. Mason, and H. Liu, "Interplay of tumor vascular oxygenation and pO₂ in tumors using NIRS, ¹⁹F MR pO₂ mapping, and pO₂ needle electrode," *J. Biomed. Optics* **8**, 53–62 (2003).
26. D. Zhao, A. Constantinescu, E. W. Hahn, and R. P. Mason, "Tumor oxygen dynamics with respect to growth and respiratory challenge: investigation of the Dunning prostate R3327-HI tumor," *Radiat. Res.* **156**, 510–520 (2001).
27. J. Bussink, J. H. A. M. Kaanders, A. M. Strik, B. Vojnovic, and A. J. van der Kogel, "Optical sensor-based oxygen tension measurements correspond with hypoxia marker binding in three human tumor xenograft lines," *Radiat. Res.* **154**, 547–555 (2000).
28. J. R. Griffiths, "The OxyLite: a fibre-optic oxygen sensor," *Br. J. Radiol.* **72**, 627–630 (1999).
29. Y. Gu, Z. Qian, J. Chen, D. Blessington, N. Ramanujam, and B. Chance, "High resolution three dimensional scanning optical image system for intrinsic and extrinsic contrast agents in tissue," *Rev. Sci. Instrum.* **73**, 172–178 (2002).
30. Ocean Optics Inc., Dunedin, Fla., March 2003. <http://www.oceanoptics.com/products/foxysystem.asp>
31. C. B. Allen, B. K. Schneider, and C. J. White, "Limitations to oxygen diffusion in *in vitro* cell exposure systems in hyperoxia and hypoxia," *Am. J. Physiol. Lung Cell Molec. Physiol.* **281**, L1021–L1027 (2001).
32. E. W. Hahn, P. Peschke, R. P. Mason, E. E. Babcock, and P. P. Antich, "Isolated tumor growth in a surgically formed skin pedicle in the rat: a new tumor model for NMR studies," *Magn. Reson. Imaging* **11**, 1007–1017 (1993).
33. Y. Song, A. Constantinescu, and R. P. Mason, "Dynamic breast tumor oximetry: the development of prognostic radiology," *Technol. Cancer Res. Treat.* **1**, 1–8 (2002).
34. S. Hunjan, D. Zhao, A. Constantinescu, E. W. Hahn, P. P. Antich, and R. P. Mason, "Tumor oximetry: demonstration of an enhanced dynamic mapping procedure using Fluorine-19 echo planar magnetic resonance imaging in the Dunning prostate R3327-AT1 rat tumor," *Int. J. Radiat. Oncol. Biol. Phys.* **49**, 1097–1108 (2001).
35. D. Zhao, A. Constantinescu, L. Jiang, E. W. Hahn, and R. P. Mason, "Prognostic radiology: quantitative assessment of tumor oxygen dynamics by MRI," *Am. J. Clin. Oncol.* **24**, 462–466 (2001).
36. J. H. Kaanders, J. Bussink, and van der A. J. Kogel, "ARCON: a novel biology-based approach in radiotherapy," *Lancet Oncol.* **3**, 728–737 (2002).
37. F. A. Howe, S. P. Robinson, L. M. Rodrigues, and J. R. Griffiths, "Flow and oxygenation dependent (FLOOD) contrast MR imaging to monitor the response of rat tumors to carbogen breathing," *Magn. Reson. Imaging* **17**, 1307–1318 (1999).
38. T. J. Dunn, R. D. Braun, W. E. Rhemus, G. L. Rosner, T. W. Secomb, G. M. Tozer, D. J. Chaplin, and M. W. Dewhirst, "The effects of hyperoxic and hypercarbic gases on tumour blood flow," *Br. J. Cancer* **80**, 117–126 (1999).

Methods in Enzymology

Volume 386

Imaging in Biological Research

Part B

EDITED BY

P. Michael Conn

OREGON NATIONAL PRIMATE RESEARCH CENTER
OREGON HEALTH AND SCIENCE UNIVERSITY
BEAVERTON, OREGON

METHODS IN ENZYMOLOGY

EDITORS-IN-CHIEF

John N. Abelson Melvin I. Simon

DIVISION OF BIOLOGY
CALIFORNIA INSTITUTE OF TECHNOLOGY
PASADENA, CALIFORNIA

FOUNDING EDITORS

Sidney P. Colowick and Nathan O. Kaplan



AMSTERDAM • BOSTON • HEIDELBERG • LONDON
NEW YORK • OXFORD • PARIS • SAN DIEGO
SAN FRANCISCO • SINGAPORE • SYDNEY • TOKYO

Academic Press is an imprint of Elsevier

ICP. Such processes include hydrocephalus, pseudotumor cerebri, intracranial mass lesions, and toxic-metabolic encephalopathy (where a depressed level of consciousness may or may not correspond to an increased ICP). MR-ICP measurement may prevent unnecessary invasive monitoring in an increased risk setting. Single time measurement of ICP may also be helpful in the evaluation of patients with possible ventriculoperitoneal shunt malfunction—particularly young children who present with nonspecific complaints and/or who are unable to communicate their symptoms. The MRI-based technique would limit exposure to harmful radiation from repeated CT scans. Also, a finding of normal ICP by the MRI-based method might prevent unnecessary shunt exploration.

If proven accurate and reliable, noninvasive, MRI-based measurement of intracranial compliance and pressure and TCBF may provide a valuable adjunct to the evaluation of patients with various neurologic problems. In the setting of TBI, a finding of increased ICP may provide an early warning signal for a physician to adjust therapy. This tool also may prove valuable in situations where external factors confound clinical evaluation (i.e., drug intoxication), where "coma" does not necessarily reflect an increased pressure state (i.e., diffuse axonal injury), or where coexisting medical problems make placement of an invasive monitor too dangerous (i.e., bleeding disorders). In each case, noninvasive MR-ICP measurement would enhance the array of currently available evaluation modalities, providing a novel adjunct to patient diagnosis and serial monitoring with limited expense and morbidity.

[17] Near-Infrared Spectroscopy and Imaging of Tumor Vascular Oxygenation

By HANLI LIU, YUEQING GU, JAE G. KIM, and RALPH P. MASON

Introduction

Current Development in Optical Methods for Vascular Hemoglobin Oxygenation

In recent years, a large number of investigations have been conducted in both laboratory and clinical settings to noninvasively monitor tissue vascular oxygenation using near-infrared (NIR) spectroscopy (NIRS) and imaging. Although the NIR imaging techniques are limited by their spatial resolutions, they have a great potential to be developed as a new imaging

Elsevier Academic Press
525 B Street, Suite 1900, San Diego, California 92101-4495, USA
84 Theobald's Road, London WC1X 8RR, UK

This book is printed on acid-free paper. ©

Copyright © 2004, Elsevier Inc. All Rights Reserved.

No part of this publication may be reproduced or transmitted in any form or by any means, electronic or mechanical, including photocopying, recording, or any information storage and retrieval system, without permission in writing from the Publisher.

The appearance of the code at the bottom of the first page of a chapter in this book indicates the Publisher's consent that copies of the chapter may be made for personal or internal use of specific clients. This consent is given on the condition, however, that the copier pay the stated per copy fee through the Copyright Clearance Center, Inc. (www.copyright.com), for copying beyond that permitted by Sections 107 or 108 of the U.S. Copyright Law. This consent does not extend to other kinds of copying, such as copying for general distribution, for advertising or promotional purposes, for creating new collective works, or for resale. Copy fees for pre-2004 chapters are as shown on the title pages. If no fee code appears on the title page, the copy fee is the same as for current chapters. 0076-6879/2004 \$35.00

Permissions may be sought directly from Elsevier's Science & Technology Rights Department in Oxford, UK: phone: (+44) 1865 843830, fax: (+44) 1865 853333, E-mail: permissions@elsevier.com.uk. You may also complete your request on-line via the Elsevier homepage (<http://elsevier.com>), by selecting "Customer Support" and then "Obtaining Permissions."

For all information on all Academic Press publications visit our Web site at www.academicpress.com

ISBN: 0-12-182791-7

PRINTED IN THE UNITED STATES OF AMERICA
04 05 06 07 08 9 8 7 6 5 4 3 2 1

modality because of their capabilities to provide functional images. NIR spectroscopy and imaging research has been mainly focused on two organs: (1) the brain and (2) the breast.

The NIR studies of the brain include detection of brain injury or trauma,¹ determination of cerebrovascular hemodynamics and oxygenation,^{2,3} and functional brain imaging in response to a variety of neurologic activations.⁴⁻⁷ NIR functional brain imaging increasingly has become of great interest in studying hemodynamic response to brain activation.⁸ This is mainly because the optical signals of the NIR techniques are able to non-invasively penetrate through the scalp and skull of an adult human and are sensitive to changes in the concentration of oxygenated (HbO) and deoxygenated hemoglobin (Hb). Although it is difficult to obtain very accurate quantification of cerebral HbO and Hb concentrations from the NIR imaging techniques due to rigorous requirements of theory and boundary conditions,⁹ the techniques can offer relatively accurate measurements of changes of HbO and Hb, thus providing quantitative changes in total cerebral blood volume (CBV), which is assumed to be proportional to total hemoglobin concentration, HbT, where $HbT = HbO + Hb$.

The objective of NIR breast imaging is to develop a novel functional imaging modality for early breast cancer detection and diagnosis beyond currently available techniques. Various efforts by several research groups¹⁰⁻¹⁵ have been made in either laboratory or clinical studies. For example, the research groups of Paulsen and colleagues¹² and of Jiang¹⁵

- ¹ S. Gopinath, C. S. Robertson, R. G. Grossman, and B. Chance, *J. Neurosurg.* **79**, 43 (1993).
- ² C. Cheung, J. P. Culver, K. Takahashi, J. H. Greenberg, and A. G. Yodh, *Phys. Med. Biol.* **46**, 2053 (2001).
- ³ G. Zhang, A. Katz, R. R. Alfano, A. D. Kofinas, P. G. Stubblefield, W. Rosenfeld, D. Beyer, D. Maulik, and M. R. Stankovic, *Phys. Med. Biol.* **45**, 3143 (2000).
- ⁴ M. Fabiani, G. Gratton, and P. M. Corballis, *J. Biomed. Opt.* **1**, 387 (1996).
- ⁵ R. Wenzel, H. Obrig, J. Ruben, K. Villringer, A. Thiel, J. Bernarding, U. Dirnagl, and A. Villringer, *J. Biomed. Opt.* **1**, 399 (1996).
- ⁶ B. Chance, E. Anday, S. Nioka, S. Zhou, L. Hong, K. Worden, C. Li, T. Murray, Y. Oveysky, D. Pidikiti, and R. Thomas, *Opt. Express* **2**, 411 (1998).
- ⁷ D. A. Boas, T. Gaudette, G. Strangman, X. Cheng, J. J. A. Marota, and J. B. Mandeville, *Neuroimage* **13**, 76 (2001).
- ⁸ D. A. Boas, G. Jaszczewski, G. Strangman, J. P. Culver, and R. Poldrack, "OSA Biomedical Topical Meetings, Technical Digest," p. 307. Miami, FL, April 7-10, 2002.
- ⁹ J. C. Hebden, E. M. C. Hillman, A. Gibson, N. Everdell, R. M. D. Yusef, D. T. Delpy, S. R. Arridge, T. Austin, and J. H. Meek, "OSA Biomedical Topical Meetings, Technical Digest," p. 587. Miami, FL, April 7-10, 2002.
- ¹⁰ B. Tromberg, N. Shah, R. Lanning, A. Cerussi, J. Espinoza, T. Pham, L. Svaasand, and J. Butler, *Neoplasia* **2**, 26 (2000).
- ¹¹ S. Fantini, S. A. Walker, M. A. Franceschini, M. Kaschke, P. M. Schlag, and K. T. Moesta, *Appl. Opt.* **37**, 1982 (1998).

have developed a frequency-domain (FD) 16-source, 16-detector breast imager and have reported their *in vivo* results of optical properties of abnormalities from female volunteers and patients. The research group led by Chance has employed a time-domain (TD) 32-channel imaging system in conjunction with magnetic resonance imaging (MRI) to increase specificity and sensitivity of breast cancer detection.¹³ Because of simplicity and low cost in comparison, to the FD and TD imaging systems, continuous-wave (CW) NIR breast imaging systems also have been developed by the groups of Barbour *et al.*¹⁴ and Chance.¹⁶ These systems are currently under clinical tests for better breast cancer detection and diagnosis.

Although Hb, HbO, and HbT concentrations and light-scattering properties of tumors may be different from those of surrounding tissues, the optical contrast between tumor and surrounding tissue is about 2-3-fold at most in absorption, and much less in light scattering.¹⁷ Thus much effort on increasing the optical contrast between tumor and healthy surrounding tissues also has been made using fluorescence imaging¹⁸ or molecular beacons¹⁶ to detect and diagnose cancer or tumor with improved sensitivity and specificity.

However, efforts in using NIR techniques to monitor tumor responses to therapeutic interventions¹⁹⁻²¹ and therapy, such as to chemotherapy²² or photodynamic therapy,²³ are very limited and preliminary. Moreover,

- ¹² T. O. McBride, B. W. Pogue, S. Jiang, U. L. Österberg, and K. D. Paulsen, *Opt. Lett.* **26**, 822 (2001).
- ¹³ V. Ntziachristos and B. Chance, "SPIE Proceedings of Optical Tomography and Spectroscopy of Tissue III," Vol. 3597, p. 565, 1999.
- ¹⁴ R. L. Barbour, C. H. Schmitz, H. L. Graber, and Y. Pei, "OSA Biomedical Topical Meetings, Technical Digest," p. 456. Miami, FL, April 7-10, 2002.
- ¹⁵ X. Gu, N. Iftimia, Y. Xu, H. Jiang, and L. L. Fajardo, "OSA Biomedical Topical Meetings, Technical Digest," p. 468. Miami, FL, April 7-10, 2002.
- ¹⁶ B. Chance, "OSA Biomedical Topical Meetings, Technical Digest" p. 450. Miami, FL, April 7-10, 2002.
- ¹⁷ J. B. Fishkin, O. Coquoz, E. R. Anderson, M. Brenner, and B. J. Tromberg, *Appl. Opt.* **36**, 10 (1997).
- ¹⁸ R. H. Mayer, J. S. Reynolds, and E. M. Sevick-Muraca, *Appl. Opt.* **38**, 4930 (1999).
- ¹⁹ H. Liu, Y. Song, K. L. Worden, X. Jiang, A. Constantinescu, and R. P. Mason, *Appl. Opt.* **39**, 5231 (2000).
- ²⁰ J. G. Kim, Y. Song, D. Zhao, A. Constantinescu, R. P. Mason, and H. Liu, *J. Biomed. Opt.* **8**, 53 (2003).
- ²¹ E. L. Hull, D. L. Conover, and T. Foster, *Br. J. Cancer* **79**, 1709 (1999).
- ²² D. B. Jakubowski, A. E. Cerussi, F. Bevilacqua, N. Shah, and B. J. Tromberg, "OSA Biomedical Topical Meetings, Technical Digest," p. 456. Miami, FL, April 7-10, 2002.
- ²³ H. Wang, T. C. Zhu, M. Solonenko, S. M. Hahn, J. Metz, A. Dimofte, J. Mile, and A. G. Yodh, "OSA Biomedical Topical Meetings, Technical Digest," Miami, FL, April 7-10, 2002.

from both prostate and breast tumors under hyperoxic respiratory interventions, using both one-channel and multichannel NIR systems, as well as one-channel and three-channel pO₂ fiber optic needle probes. At the end, we wish to demonstrate that the NIR techniques are complementary with tumor pO₂ readings and can be used as a new prognostic means for cancer therapy prognosis and therapy planning.

Theory and Algorithms

It is well known that hemoglobin concentrations and oxygen saturation in tissue vasculature can be determined using NIRS, since light absorptions of HbO and Hb in the NIR range are distinct. As with our previous work,^{19,20} we assumed that HbO and Hb are the major significant absorbing species in tissue vasculature, including tumors, within the selected NIR range of 700–900 nm. Although diffusion theory has been a well-accepted theoretical approach to mathematically quantify light-tissue interaction,^{6,7,10,47} no analytical solution has been available for solid tumors because of their finite size and high heterogeneity. While our future work will use the finite element method to obtain numerical solutions for the diffusion equation, our current approach is based on modified Beer-Lambert's law to account for light scattering in tumor tissue.

For a nonscattering medium, Beer-Lambert's law gives rise to the following expressions for the relationships between the absorption coefficient, μ_a , and the extinction coefficient for deoxyhemoglobin (ϵ_{Hb}) and oxyhemoglobin (ϵ_{HbO}):

$$\mu_a^{758} = 2.3 \{ \epsilon_{\text{Hb}}^{758} [\text{Hb}] + \epsilon_{\text{HbO}}^{758} [\text{HbO}] \} \quad (1)$$

$$\mu_a^{785} = 2.3 \{ \epsilon_{\text{Hb}}^{785} [\text{Hb}] + \epsilon_{\text{HbO}}^{785} [\text{HbO}] \} \quad (2)$$

where [HbO] and [Hb] are concentrations of HbO and Hb, respectively, the factor of 2.3 results from the different definitions of μ_a and ϵ in relation to the incident and detected optical intensities. The conventional definitions for μ_a and ϵ are $I = I_0 e^{-\mu_a L}$ and $I = I_0 10^{-\epsilon CL}$, respectively, where I_0 and I are the incident and detected optical intensities in transmission measurement from a nonscattering medium, C is the concentration of hemoglobin measured in mM/L, and L is the optical pathlength through the medium in cm. By eliminating I and I_0 in these two expressions, we arrived at a relationship of $\mu_a = 2.3 \epsilon C$.

⁴⁷ M. S. Patterson, B. Chance, and B. C. Wilson, *Appl. Opt.* **28**, 2331 (1989).

Because of light scattering in tissue, Beer-Lambert's law cannot be applied directly to biologic tissue, such as tumors. By taking an empiric approach to modify Beer-Lambert's law, we arrived at $\mu_a = 2.3 \epsilon C = 2.3/L_S \log(I_0/I)$, where L_S represents the optical pathlength in a scattering medium and is no longer equal to the physical distance between the source and detector, d . In a highly light-scattering medium, L_S is much longer than d . Specifically, in the tumor study, we use I_0 and I to represent the incident and detected light intensities, when the tissue sample is without and with light absorption from [HbO] and/or [Hb]. Then, changes in absorption coefficient of the tumor, $\Delta\mu_a$, between baseline and transient conditions under respiratory intervention can be expressed as

$$\Delta\mu_a = \mu_{aT} - \mu_{aB} = 2.3 \log(I_B/I_T)/L_S \quad (3)$$

where I_B and I_T are baseline and transient light intensities of the measured optical signals, respectively.

Using the transmitted light intensities at $\lambda_1 = 758$ nm and $\lambda_2 = 785$ nm and manipulating Eqs. (1)–(3), we can quantify the changes of tumor [HbO] and [Hb] due to an intervention as follows:

$$\Delta[\text{HbO}] = -11.73 \times \frac{\log(I_B/I_T)^{\lambda_1}}{L_S^{\lambda_1}} + 14.97 \times \frac{\log(I_B/I_T)^{\lambda_2}}{L_S^{\lambda_2}} \quad (4)$$

$$\Delta[\text{Hb}] = 8.09 \times \frac{\log(I_B/I_T)^{\lambda_1}}{L_S^{\lambda_1}} - 6.73 \times \frac{\log(I_B/I_T)^{\lambda_2}}{L_S^{\lambda_2}} \quad (5)$$

where $L_S^{\lambda_1}$ and $L_S^{\lambda_2}$ are optical path lengths between the source and detector at the respective wavelengths. The units of $\Delta[\text{HbO}]$ and $\Delta[\text{Hb}]$ in Eqs. (4) and (5) are mM. The constants given in the equations were computed with the extinction coefficients for oxygenated and deoxygenated hemoglobin at the two wavelengths used.⁴⁸

In principle, $L_S^{\lambda_1}$ and $L_S^{\lambda_2}$ in Eqs. (4) and (5) are variables, depending on the actual separation of source and detector, as well as the optical properties of tumor. Previously, a differential pathlength factor (DPF), (i.e., $L_S = d \times \text{DPF}$) has been introduced to associate L_S with d .⁴⁹ The DPF values of blood-perfused tissues have been studied intensively for muscles⁵⁰ and

⁴⁸ W. G. Zijlstra, A. Buursma, and W. P. Meeuwse-van der Roest, *Clin. Chem.* **37**, 1633 (1991).

⁴⁹ D. T. Delpy, M. Cope, P. van der Zee, S. Arridge, S. Wray, and J. Wyatt, *Phys. Med. Biol.* **33**, 1433 (1988).

⁵⁰ M. Ferrari, Q. Wei, L. Carraresi, R. A. De Blasi, and G. Zaccanti, *J. Photochem. Photobiol.* **16**, 141 (1992).

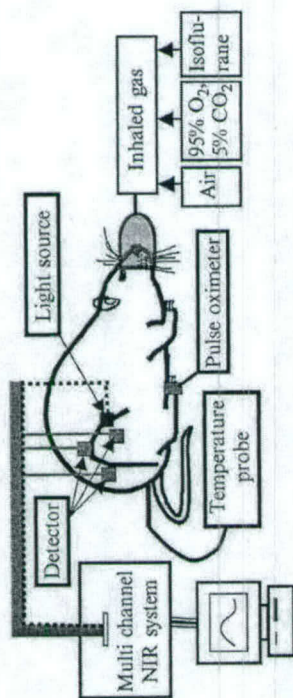


Fig. 2. Schematic experimental setup for three-channel NIRS experiments. One of the three detectors was placed opposite to the light source in order to detect light in transmission mode, and the other two detectors were set in the semireflection mode on the tumor surface.

at the measured wavelengths, $I_{bc}(\lambda)$ and $Q_{bc}(\lambda)$, lead to the quantification of optical amplitudes, $A(\lambda)$, and phase, $\theta(\lambda)$, that have passed through the tumor tissues³⁵:

$$A(\lambda) = \sqrt{I(\lambda)_{DC}^2 + Q(\lambda)_{DC}^2} \quad (9)$$

$$\theta(\lambda) = \arctan \left(\frac{Q(\lambda)_{DC}}{I(\lambda)_{DC}} \right) \quad (10)$$

where λ represents the respective wavelengths used in the NIR system. Then, changes in light intensity through the tumor caused by hyperoxic interventions are used to compute changes in tumor vascular [HbO] and [Hb]. Whether the readings of $\theta(\lambda)$ can be linked to tumor physiology remains to be further explored.

Besides a one-channel NIR system, we have also used a multichannel NIR system (Fig. 2) to explore and reveal intratumoral vascular heterogeneity by having simultaneous readings at several separations of the source and detectors. Unlike the single-channel system, the multichannel system uses two laser diodes at 730 and 850 nm with constant light intensities (i.e., DC light) and three photo detectors. These detectors are placed along the circumference together with the light source, with three different source-detector separations in order to detect different depths within the tumor volume, as demonstrated in Fig. 3.

Following the same procedures as those described in the previous section, we arrived at the expression of $\Delta[HbO]$ for the multichannel system with the two wavelengths of 730 and 830 nm, as follows:

³⁵ Y. Yang, H. Liu, X. Li, and B. Chance, *Opt. Eng.* 36, 1562 (1997).

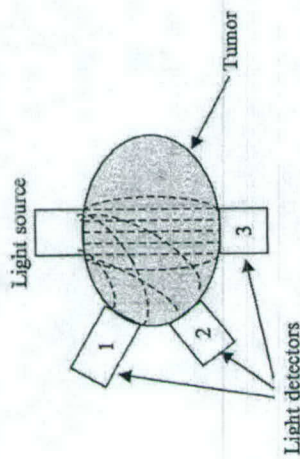


Fig. 3. A schematic diagram showing the locations of the three detectors and possible internal tumor volumes interrogated by the different detectors.

$$\Delta[HbO] = \frac{-0.674 \cdot \log \left(\frac{A_B}{A_T} \right)^{730} + 1.117 \cdot \log \left(\frac{A_B}{A_T} \right)^{830}}{d} \quad (11)$$

where d is the direct source-detector separation in cm, and the unit of $\Delta[HbO]$ is mM/DPF.

System Testing and Calibration

It is important to characterize and verify linearity of the NIRS system before any animal experiment starts. We have performed two critical system tests: (1) to quantify the output voltage range, within which the NIR system has a linear response, and (2) to perform liquid phantom measurements to confirm the physiologic readings derived from the optical NIRS system.

Linearity Testing Associated with Crosstalk Between the Amplitude and Phase. In principle, changes in amplitude of an FD photon migration system should be independent of its changes in phase (i.e., the crosstalk between amplitude and phase should be minimal for an ideal NIR system). However, in reality, it is difficult to have such a perfect condition for an actual instrument, so it is necessary to conduct the crosstalk test. We altered the optical densities (O.D.) of optical filters in front of the two light sources (758 and 785 nm) to attenuate the detected amplitude, so we could see whether changes in amplitude and phase were correlated. The test showed that phase-amplitude crosstalk exists, if the measured output intensity is either too small (<50 mV) or too large (>380 mV), as shown in Fig. 4A and 4B for 758 nm and 785 nm, respectively. We also plotted O.D. values of the filters versus log (amplitude of the output signal) to see the electrical attenuation of the system output in response to the optical

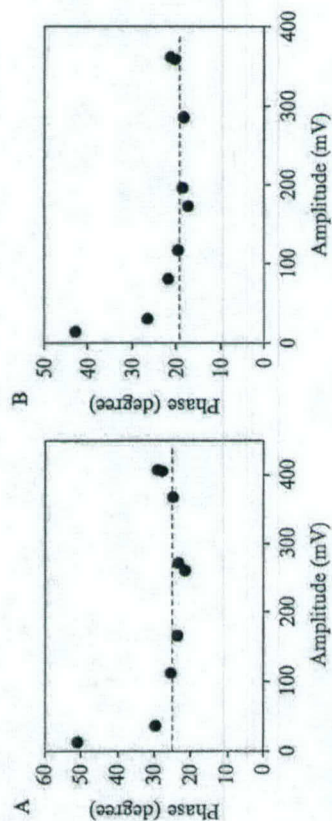


FIG. 4. Relationships between the output amplitude (mV) and phase (in degree) of the NIR single-channel system at (A) 758 nm and (B) 785 nm.

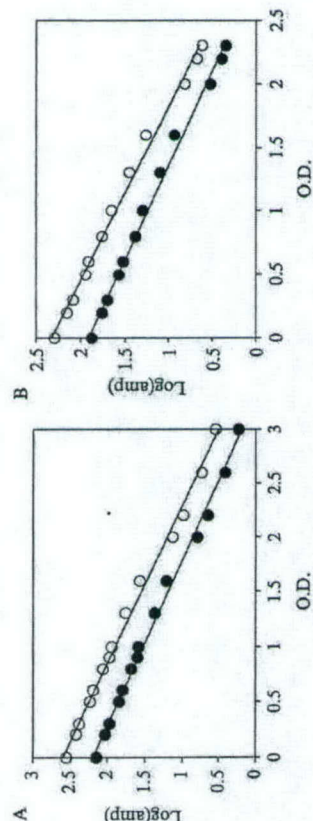


FIG. 5. Linearity tests for the NIR system between the optical input attenuation and electrical output signals at 758 nm (open circles) and 785 nm (solid circles). The X variable is the optical density (O.D. = $\log(I_0/I)$) of the filters, which were inserted before the detector to attenuate the light intensity. Cases (A) and (B) correspond to a higher (350 mV for 758 nm) and lower (193 mV for 785 nm) output voltage, respectively. Both 350 and 193 mV were obtained when the measurement was performed without any optical attenuation.

attenuation. It was found that as long as the output is in the range 100–350 mV, good linearity is achieved for the system response, as shown in Fig. 5A and 5B.

Blood Phantom Study. To calibrate the NIRS system for quantifying hemoglobin concentrations, we used human blood for tissue phantom experiments. Two packets of Sigma (St. Louis, MO) P-3813 phosphate buffered saline (PBS) (pH 7.4) powder was used to make a 2-liter buffer, and 100 ml of 20% intralipid was added into the buffer for a 1% intralipid solution, as shown in Fig. 6A. Then 14 g of baking yeast was mixed with tap

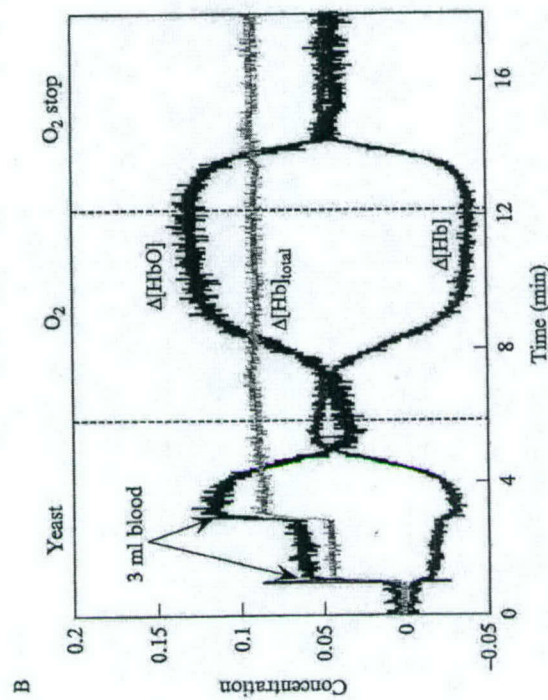
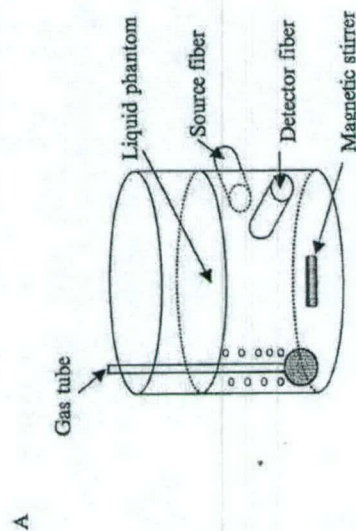


FIG. 6. (A) Experimental setup for system calibration using a liquid phantom with 1% Intralipid and baker's yeast in saline buffer. The NIRS probes were placed in reflectance geometry, while the gas bubbler was placed opposite to minimize liquid movement effects. (B) Simultaneous dynamic changes of $\Delta[HbO]$, $\Delta[Hb]$, and $\Delta[Hb]_{total}$ in the phantom solution measured using the NIR single-channel system. The dark solid curve is for $\Delta[HbO]$, the lighter solid line is for $\Delta[Hb]_{total}$, and the gray solid line shows $\Delta[Hb]$ in the phantom solution. Blood was deoxygenated by the yeast's oxygen consumption and oxygenated by bubbling O₂. During the oxygenation and deoxygenation process, $\Delta[Hb]_{total}$ was maintained as a constant.²⁰

water before being added into the 2-liter buffer solution to deoxygenate the tissue phantom solution. Amount of blood for each addition to the solution was 3 ml for two additions after the yeast was well mixed in the solution.

When the blood was fully deoxygenated by yeast, pure oxygen was introduced in the solution to oxygenate the blood. After the blood was fully oxygenated, oxygen blowing was stopped in order to re-deoxygenate the solution by yeast again. The gas tube for oxygen delivery was placed far from the NIRS probes to minimize any liquid movement effects, as shown in Fig. 6A. Source and detector probes for the NIRS system were placed in reflection geometry with a direct separation of ~ 3 cm. The solution was stirred constantly with a magnetic stirrer to maintain homogeneity.

After getting the raw amplitude data from the experiment, we used Eqs. (6) to (8) to calculate $\Delta[\text{HbO}]$, $\Delta[\text{Hb}]$, and $\Delta[\text{Hb}]_{\text{total}}$. As shown in Fig. 6B, $\Delta[\text{Hb}]_{\text{total}}$ remained constant, as expected, whereas $\Delta[\text{HbO}]$ and $\Delta[\text{Hb}]$ altered in opposite directions during the oxygenation and deoxygenation cycle. This demonstrates that the two assumptions used to derive Eqs. (6) and (8) are correct and necessary to compensate the differences in DPF caused by two different wavelengths.²⁰ Notice that there appears to be a delay between the gas switch and responses of $\Delta[\text{HbO}]$ and $\Delta[\text{Hb}]$ as shown in Fig. 6B. This delay is possibly caused by the entire process of transporting oxygen gas from the tube to the solution, oxygenating/deoxygenating the solution, and reaching a homogeneous state near the detectors.

Animal Models

In the prostate tumor study, Dunning prostate R3327-HI rat tumors (originally obtained from Dr. Peter Peschke, DKFZ Heidelberg) were implanted in pedicles on the foreback of adult male Copenhagen rats.⁵⁶ In the breast tumor study, rat mammary adenocarcinomas 13762NF (originally obtained from the Division of Cancer Therapeutics, National Cancer Institute [DCT NCI]) grown in the hindlimb of adult female Fisher 344 rats (~ 200 g) were used. Once the tumors reached approximately 1–2 cm in diameter, the rats were anesthetized with 0.2 ml ketamine hydrochloride (100 mg/ml; Aveco, Fort Dodge, IA) and maintained under general gaseous anesthesia with isoflurane in air (1.3% isoflurane at 1 dm³/min air) through a mask placed over the mouth and nose. Tumors were shaved to improve optical contact for transmitting light. Body temperature was maintained by a warm water blanket and was monitored by a rectally

⁵⁶ E. W. Hahn, P. Peschke, R. P. Mason, E. E. Babcock, and P. P. Antich, *Magn. Reson. Imaging* 11, 1007 (1993).

inserted thermal probe (see Fig. 1) connected to a digital thermometer (Digi-Sense, Model 91100-50; Cole-Parmer Instrument Company, Vernon Hills, IL). A pulse oximeter (Model 8600; Nonin, Inc., Plymouth, MN) was placed on the hindfoot to monitor arterial oxygenation (S_aO_2). Tumor volume V (in cm³) was estimated as $V = 4\pi/3(L + W + H/6)^3$, where L , W , and H are the three respective orthogonal dimensions.

In general, the source-detector fiber separation was about 1–1.5 cm in transmittance geometry, and thus the tumor volume interrogated by NIR light can be estimated as follows. The radius of probe is 0.4 cm, which makes the volume of the cylinder 0.5–0.75 cm³. By diffusion approximation, the optical penetration depth is about one third of the direct distance between the source and detector, which makes an additional spherical volume with a radius from 0.5–0.75 cm. Therefore the total tumor volume interrogated by NIR light can be estimated in the range of 1.0–2.5 cm³, depending on the actual source-detector separation.²⁰

Measurements of $p\text{O}_2$ Using Oxygen Needle Electrode and Fiber-Optic Fluorescence-Quenched Probe

Needle Electrode. We used a needle-type oxygen electrode for local $p\text{O}_2$ readings in several tumors. Linear two-point calibrations were performed with air (21% O_2) and pure nitrogen (0% O_2) saturated saline buffer solutions before the animal experiments, and we estimated an instrumental precision of 2–3 mmHg. After calibration, the needle electrode was inserted carefully into the tumor with the reference electrode being placed rectally, as described in detail previously.²⁰ Both the sample and reference electrodes were connected to a picoammeter (Chemical Microsensor; Diamond Electro-Tech, Inc., Ann Arbor, MI) and polarized at -0.75 V. Measurement points of $p\text{O}_2$ were manually recorded, whereas the NIRS data were acquired automatically. Measurements of $p\text{O}_2$ and NIRS were initiated, while rats breathed air for ~ 10 min to demonstrate a stable baseline. The inhaled gas was then switched to carbogen (5% CO_2 and 95% O_2) or oxygen for 15 min and switched back to air.

Fiber-Optic Fluorescence-Quenched Probe. For multiple $p\text{O}_2$ readings, we used a multichannel, fiber-optic, oxygen-sensing system (FOXY; Ocean Optics, Inc.). We calibrated the three fluorescence-quenched, optical fiber probes initially and then inserted them into different regions of the tumors to monitor the changes of oxygen tension ($\Delta p\text{O}_2$) in response to the respiratory challenges as described previously.²⁴ The probes were placed in such a way that at least one was in a relatively poorly oxygenated region (low baseline $p\text{O}_2$) and at least one was in a relatively well-oxygenated region (high baseline $p\text{O}_2$). A mean $\Delta p\text{O}_2$ of the tumor was obtained by

averaging the three readings. A typical FOXY channel used a pulsed blue light-emitting diode (LED) at ~475 nm and was coupled into one branch of a bifurcated optical fiber bundle. Then, the fluorescent light was propagated to the FOXY probe tip. Each probe had two 300- μ m-diameter optical fibers with an aluminum jacket. The distal end of the probes was coated with a thin layer of a hydrophobic sol-gel material, so that an oxygen-sensing ruthenium complex was effectively trapped and protected from water. The ruthenium complex at the probe tips was excited by the blue LED and emitted fluorescence at ~600 nm. If the excited ruthenium complex encountered an oxygen molecule, the excess energy would be transferred to the oxygen molecule in a nonradiative transition, decreasing or quenching the fluorescence signal.

The fluorescence response of the ruthenium complex was highly temperature dependent, so the probe calibration was accomplished by streaming gases of known oxygen concentrations (100, 20.9, 10, 2, and 0%) through a cylindrical water jacket heated to 37°. Calibration curves were calculated by the vendor-supplied software, using the second-order, polynomial calibration:

$$\frac{I_0}{I} = 1 + K_1[O] + K_2[O]^2 \quad (12)$$

where I_0 is the fluorescence intensity at zero concentration (nitrogen), I is the measured intensity of fluorescence at a pressure p of oxygen, $[O]$ represents the oxygen concentration (related to pO_2), and K_1 and K_2 are the first- and second-order coefficients and are automatically supplied by the curve-fitting routine from the calibration measurements. After the system calibration, the oxygen concentration in tumor-tissue sample measurements was deduced using Eq. (12).

NIR Measurements of Breast-Prostate Tumors Under Interventions

We conducted all animal experiments in a darkened room, and the measurements were initiated while the rats breathed air for 10 min to get a stable baseline. The inhaled gas was switched to carbogen (5% CO_2 and 95% O_2) or pure oxygen for 15–20 min, and then back to air for 15 min. Sometimes, repeated cycles were taken either to check the reproducibility or to minimize preconditioning effects. Raw amplitude data from either the one-channel or three-channel detectors were recorded simultaneously during the experiments, processed, and displayed through the computer to obtain tumor $\Delta[HbO]$ and $\Delta[Hb]_{total}$. The dynamic data were fitted with a single-exponential and/or double-exponential expression, using Kaleidagraph software (Synergy Software, Reading, PA), to obtain time constants

and amplitudes. Those fitted parameters allowed us to further develop a two-region tumor model, which will be discussed in a later section.

In many cases, we performed simultaneous measurements of changes in tumor HbO and in tumor pO_2 , using either the needle electrode or the fiber-optic FOXY system along with the NIRS readings, as shown in Fig. 1, for both breast and prostate tumors.

Results and Model Development

HbO and pO_2 Changes in Prostate Tumors Under Carbogen Intervention

We have measured relative changes of $[HbO]$, $[Hb]_{total}$, and tumor tissue pO_2 from several Dunning prostate R3327-HI tumors, and Fig. 7 shows two representative data sets. Figure 7A shows the temporal profiles of $\Delta[HbO]$ and pO_2 in a Dunning prostate R3327-HI tumor (3.6 cm^3) measured simultaneously with the NIRS and pO_2 needle electrode during carbogen respiratory challenge. After the breathing gas was switched from air to carbogen, $\Delta[HbO]$ increased rapidly, whereas $\Delta[Hb]_{total}$ seemed to have much smaller responses. In this case, tumor tissue pO_2 increased at a much slower rate, from a baseline of 60 mmHg to ~80 mmHg during the entire carbogen intervention. Figure 7B is obtained from another prostate tumor (3.1 cm^3); the electrode readings showed a slower pO_2 response from ~15 to 40 mmHg, whereas the NIRS response was biphasic, a sharp rise in $\Delta[HbO]$ followed by a further slow, gradual significant increase over the next ~15 min. In this case, $\Delta[Hb]_{total}$ showed little change, ~2% of the maximum in $\Delta[HbO]$. The biphasic feature of $\Delta[HbO]$ has been a commonly observed dynamic characteristic under tumor vascular oxygenation, as reported previously.^{19,20,24}

HbO and pO_2 Changes in Breast Tumors Under Carbogen and Oxygen Intervention

For a representative 13762NF breast tumor (3.2 cm^3), typical time profiles of the normalized $\Delta[HbO]$ and mean ΔpO_2 in response to carbogen and then oxygen intervention are shown in Fig. 8. When the inspired gas was switched from air to carbogen, the normalized $\Delta[HbO]$ showed a sharp initial rise in the first minute ($p < 0.0001$), followed by a slower, gradual, but further significant increase over the next 19 min ($p < 0.001$). The mean ΔpO_2 profile was averaged over the three individual ΔpO_2 readings (FOXY), and it increased rapidly by about 50 torr (= mmHg) within 8 min ($p < 0.0005$) and also continued a slower and gradual increase over the next 12 min ($p < 0.005$). Return to breathing air produced a significant

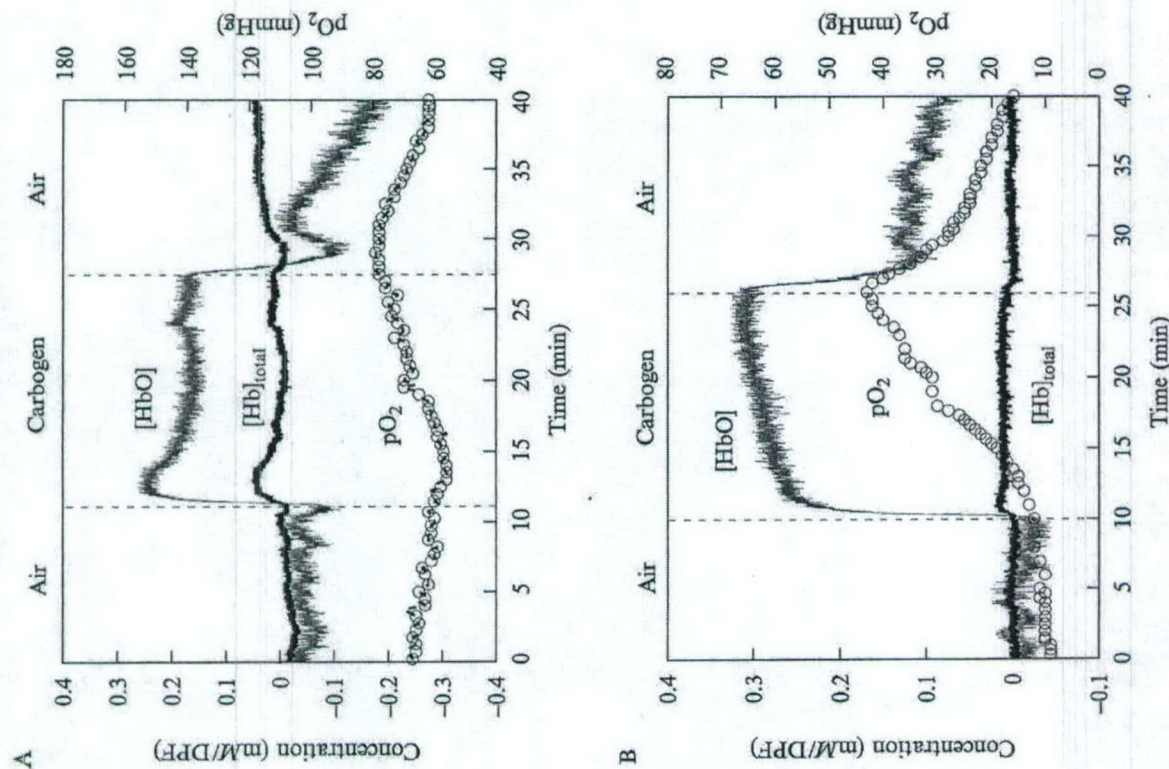


Fig. 7. Simultaneous dynamic changes of $\Delta[\text{HbO}]$ and $p\text{O}_2$ in R3327-H1 rat prostate tumors using NIRS and $p\text{O}_2$ needle electrode. (A) A representative tumor (3.6 cm^3) showed a rapid NIR response, whereas (B) another tumor (3.1 cm^3) showed a clear biphasic feature in $\Delta[\text{HbO}]$ with a slow $p\text{O}_2$ response. The unit of $\Delta[\text{HbO}]$ is mM/DPF , where DPF is equal to the optical pathlength divided by the source-detector separation. Dotted vertical line marks the time when the gas was changed.

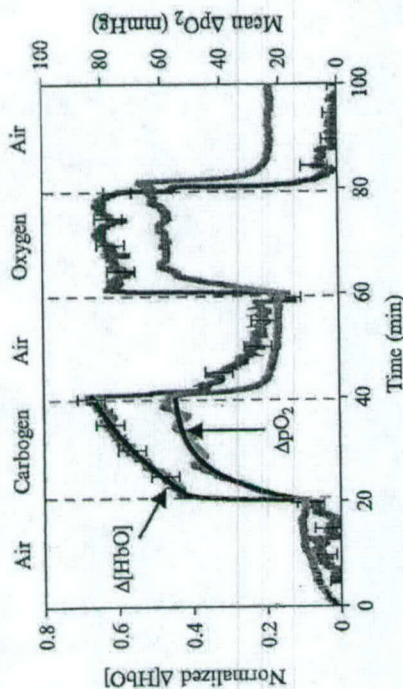


Fig. 8. Dynamic responses of $\Delta[\text{HbO}]$ and mean $\Delta p\text{O}_2$ to hyperoxic gas intervention in a rat breast tumor (3.2 cm^3). In response to carbogen breathing, single-exponential curve fitting yielded $\Delta p\text{O}_2 = 42.68 [1 - \exp(-(t - 21.01)/4.56)] + 16.66$ ($r = 0.98$), and biexponential fitting resulted in $\Delta[\text{HbO}] = 0.373 [1 - \exp(-(t - 20.36)/0.61)] + 0.648 [1 - \exp(-(t - 20.36)/21)]$ ($r = 0.97$). The smooth black curves plotted along with the data are obtained according to the previous exponential expressions, respectively.

decline for both signals ($p < 0.0001$). When the hyperoxic intervention was repeated with pure oxygen, the dynamic features of $\Delta[\text{HbO}]$ and $\Delta p\text{O}_2$ remained consistent, except that the biphasic behavior of $\Delta[\text{HbO}]$ was less apparent. A detailed investigation on $\Delta[\text{HbO}]$ differences in response to carbogen and oxygen interventions has been given in our earlier study.²⁴

In response to carbogen intervention, the $p\text{O}_2$ profile displayed a single-phase dynamic behavior, whereas $\Delta[\text{HbO}]$ showed an apparent biphasic response. These dynamics may be characterized by time constants of single- and double-exponential responses, respectively. A single exponential fitting gives rise to a slow $\Delta p\text{O}_2$ response of $\tau(\Delta p\text{O}_2) = 4.56 \pm 0.06 \text{ min}$ ($r = 0.98$). A double-exponential expression with two time constants, τ_1 and τ_2 , was used to fit the normalized $\Delta[\text{HbO}]$, yielding fast and slow time constants of 0.61 min and 21 min, respectively. Figure 8 plots the fitted curves along with the experimental data. During the course of our study, we have often observed biphasic characteristic of $\Delta[\text{HbO}]$, which motivated us to develop a model to interpret the experimental finding, to be described in a later section.

The advantage of using FOXY $p\text{O}_2$ probes is to detect distinct heterogeneity in tumor $p\text{O}_2$. The individual responses at different locations within the tumor to the hyperoxic gas were diverse: those probes that indicated

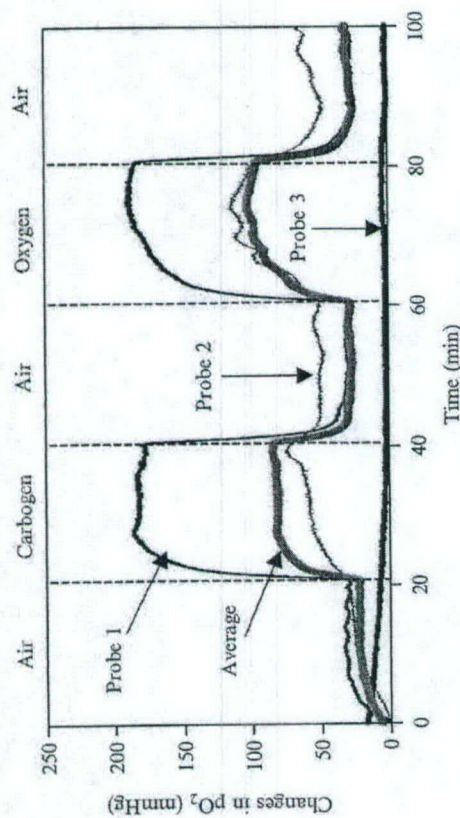


FIG. 9. Time profiles of tumor oxygen tension changes, ΔpO_2 , measured with three channels of a FOXY fiber-optic, oxygen-sensing system with respect to different gas inhalations for a breast tumor (4.6 cm^3). The mean signal for the three channels was calculated and plotted by the thicker trace. Modified from Gu *et al.*²⁴

apparently well-oxygenated regions usually showed a large and rapid response, whereas those with lower baseline pO_2 often showed little change (Fig. 9). By studying a group of five rats with both carbogen and oxygen interventions, we obtained a distinct correlation between the maximal values of global $\Delta[HbO]$ and the mean ΔpO_2 , as shown in Fig. 10. Because of heterogeneity in regional pO_2 , the standard deviations of the mean pO_2 values were quite large.

Tumor Heterogeneity Observed by a Multichannel NIRS System

To study tumor heterogeneity, the multichannel NIRS system also has been used to detect changes in $[HbO]$ with different source-detector separations. Fig. 11A shows three temporal profiles of $\Delta[HbO]$ obtained from three detectors in a breast tumor (16.6 cm^3), with a source-detector separation of 1.5 cm for detector 1, 2.5 cm for detector 2, and 2.8 cm for detector 3, respectively (Fig. 3). The measurement uncertainties are plotted at discrete times in Fig. 11A. After 10 min of air breathing measurement as the baseline, the inhaled gas was switched from air to carbogen, causing a sharp increase in $\Delta[HbO]$ ($p < 0.0001$ after 1 min from gas switch), followed by a further gradual, but significant, increase over the next 15 min ($p < 0.0001$).

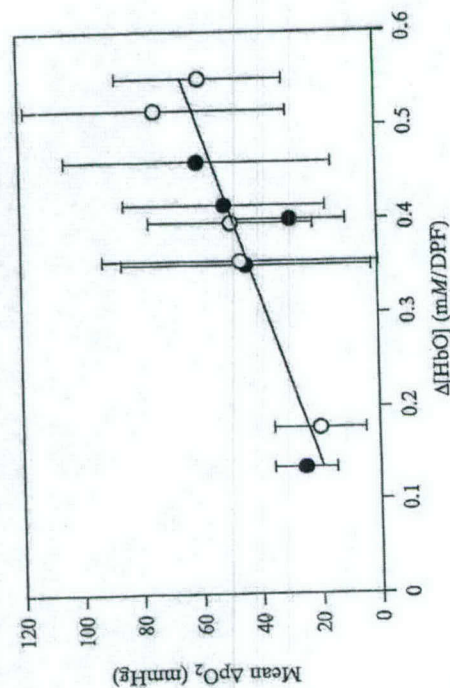


FIG. 10. Correlation between mean ΔpO_2 and ΔHbO for five breast tumors ($r > 0.86$) with a linear relationship of $\Delta pO_2 = 110.65 \Delta HbO + 4.1285$. Solid circles are for transition air to carbogen, whereas open circles are for transition carbogen to oxygen.²⁴

As with the single-channel NIRS measurement, the biphasic features appear clearly in the multichannel results. The rising parts of $\Delta[HbO]$ from detectors 1, 2, and 3 after gas switch to carbogen are shown in Fig. 11B–11D, respectively, along with the fitted curves. The two equations used for the curve fitting are

$$\Delta[HbO]_{\text{single}} = A\{1 - \exp[-(t - t_0)/\tau]\} \quad (13)$$

$$\Delta[HbO]_{\text{double}} = A_1\{1 - \exp[-(t - t_0)/\tau_1]\} + A_2\{1 - \exp[-(t - t_0)/\tau_2]\} \quad (14)$$

respectively, for the single-exponential and double-exponential expressions. It is clear that the double-exponential expression gives a much better fit, as confirmed by the respective chi squared (χ^2) and R^2 values. Table I summarizes all the fitted parameters for the respective detectors.

Mathematical Model Development to Interpret Data

As shown in the last section, the temporal profiles of tumor $\Delta[HbO]$ caused by respiratory challenge can be well fitted with a double-exponential equation, represented by two time constants (fast and slow). To understand these time constants and to interpret the experimental findings, we further developed a hemoperfusion model,¹⁹ briefly described as follows.

TABLE I
SUMMARY OF VASCULAR OXYGEN DYNAMICS FROM THREE DETECTORS FROM FIG. 11

Double-exponential fitting $\Delta\text{HbO}_2 = A_1[1 - \exp(-t/\tau_1)] + A_2[1 - \exp(-t/\tau_2)]$			
Parameters	Detector 1	Detector 2	Detector 3
Separation: d (cm)	1.5	2.5	2.8
A_1 (mM/DPF)	0.0134 ± 0.0002	0.0125 ± 0.0002	0.0134 ± 0.0002
τ_1 (min)	0.24 ± 0.01	0.30 ± 0.02	0.27 ± 0.01
A_2 (mM/DPF)	0.020 ± 0.001	0.0130 ± 0.0004	0.0060 ± 0.0002
τ_2 (min)	8.27 ± 0.72	9.87 ± 0.84	7.00 ± 0.58
χ^2	0.005	0.001	0.0005
R^2	0.95	0.96	0.95
$\tau_1/\tau_2 = A_1/A_2$	1.85 ± 0.07	0.96 ± 0.05	2.23 ± 0.08
τ_1/τ_2	0.029 ± 0.004	0.030 ± 0.004	0.039 ± 0.005
$f_1/f_2 = (A_1/A_2)/(\tau_1/\tau_2)$	64 ± 9	32 ± 5	58 ± 9

Following an approach used to measure regional cerebral blood flow (rCBF) with diffusible radiotracers,⁵⁷⁻⁵⁹ we made an analogy to evaluate tumor hemodynamics, using the respiratory intervention gas as a tracer.

In response to respiratory intervention, a sudden small change introduced in arterial O_2 saturation (S_aO_2) results in an increase in arterial HbO concentration ($\Delta\text{HbO}^{\text{artery}}$). This increase in $\text{HbO}^{\text{artery}}$ can be considered as an intravascular tracer.⁶⁰ Following Kety's method and assuming that changes in dissolved O_2 are negligible,⁶⁰ we have

$$\frac{d}{dt}(\Delta\text{HbO}^{\text{vasculature}}) = f \left(\Delta\text{HbO}^{\text{artery}} - \frac{\Delta\text{HbO}^{\text{vasculature}}}{\gamma} \right) \quad (15)$$

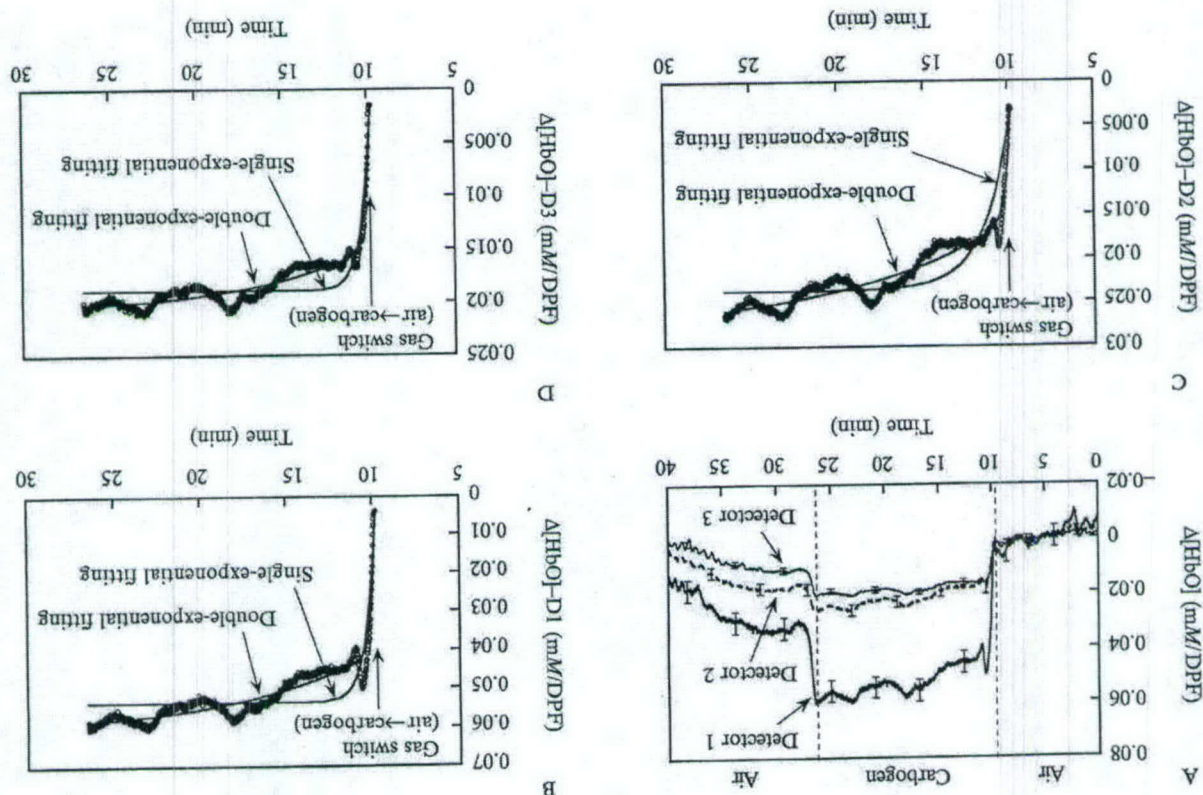
⁵⁷ S. S. Kety, *Pharmacol. Rev.* 3, 1 (1951).

⁵⁸ S. S. Kety, *Israel J. Med. Sci.* 23, 3 (1987).

⁵⁹ H. Watabe, M. Itoh, V. Cunningham, A. A. Lammeritsma, P. Bloomfield, M. Mejia, T. Fujiwara, A. K. P. Jones, T. Jones, and T. Nakamura, *J. Cerebr. Blood Flow Metab.* 16, 311 (1996).

⁶⁰ A. D. Edwards, C. Richardson, P. van der Zee, C. Elwell, J. S. Wyatt, M. Cope, D. T. Delpy, and E. O. R. Reynolds, *J. Appl. Physiol.* 75, 1884 (1993).

Fig. 11. (A) Dynamic changes of $[\text{HbO}]$ measured at three detectors from a rat breast tumor (volume: 16.6 cm^3). Dotted vertical lines mark the points when the gas was changed. The rising parts of $\Delta[\text{HbO}]$ obtained from three detectors were fitted using both single-exponential and double-exponential expressions, and (B) to (D) are from detectors 1 to 3, respectively.



where f represents blood perfusion rate, and γ is defined as a vasculature coefficient of the tumor. The coefficient, γ , is the ratio of HbO concentration change in the vascular bed to that in veins and equals $(\Delta\text{HbO}^{\text{vasculature}})/(\Delta\text{HbO}^{\text{vein}})$.

In Eq. (15), whereas f and γ are constants, $\Delta\text{HbO}^{\text{vasculature}}$ is a time-dependent variable. In principle, $\Delta\text{HbO}^{\text{vasculature}}$ can be solved rigorously given a constant input, H_0 , for $\Delta\text{HbO}^{\text{artery}}$ after time 0. Our previous study demonstrates that changes in arterial HbO (S_aO_2) are much faster than that in the vascular bed.¹⁹ Then we arrive at Eq. (16):

$$\Delta\text{HbO}^{\text{vasculature}}(t) = \gamma \times H_0 \times (1 - e^{-ft/\gamma}) \quad (16)$$

Equation (16) indicates that the change in oxygenated hemoglobin concentration in tumor vasculature, $\Delta\text{HbO}^{\text{vasculature}}(t)$, depends on the blood perfusion rate, f , the arterial oxygenation input, H_0 , and the vasculature coefficient of the tumor, γ .

Our NIR instrument indeed measures changes in vascular HbO concentration (i.e., $\Delta[\text{HbO}]^{\text{vasculature}}$). Then, Eq. (16) can be used to interpret the NIR measurements, since it gives the same exponential form as Eqs. (13) and (14), used to fit the experimental data. The comparison between Eqs. (13) and (16) reveals that the measured time constant is closely associated with the blood perfusion rate, f , and the vasculature coefficient of the tumor, γ in the measured volume. Furthermore, if the measured volume involves two distinct regions, then the detected signal will involve two different blood perfusion rates, f_1 and f_2 , and/or two different vasculature coefficients, γ_1 and γ_2 . In this case, it is reasonable to assume that the measured signal results from both of the regions, as illustrated in Fig. 12A. Consequently, Eq. (16) can be modified with a two-exponential expression and two time constants:

$$\begin{aligned} \Delta\text{HbO}^{\text{vasculature}}(t) &= \gamma_1 \times H_0 \times (1 - e^{-f_1 t/\gamma_1}) + \gamma_2 \times H_0 \times (1 - e^{-f_2 t/\gamma_2}) \\ &= A_1 \times (1 - e^{-f_1 t/\gamma_1}) + A_2 \times (1 - e^{-f_2 t/\gamma_2}) \end{aligned} \quad (17)$$

where f_1 and γ_1 are the blood perfusion rate and vasculature coefficient from region 1, respectively, f_2 and γ_2 are from region 2, and $A_1 = \gamma_1 \times H_0$ and $A_2 = \gamma_2 \times H_0$. The two time constants are equal to $\tau_1 = \gamma_1/f_1$ and $\tau_2 = \gamma_2/f_2$, respectively. When A_1, A_2 , and the two time constants are determined from our NIR measurements, we arrive at the ratios for the two vasculature coefficients and the two blood perfusion rates:

$$\frac{\tau_1}{\tau_2} = \frac{A_1}{A_2}; \quad \frac{f_1}{f_2} = \frac{A_1/A_2}{\tau_1/\tau_2} \quad (18)$$

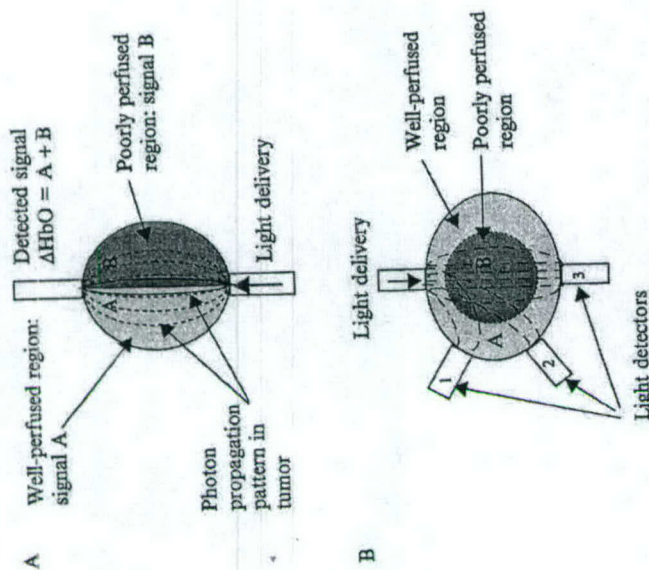


Fig. 12. (A) Schematic diagram to show a tumor model with two vascular perfusion regions, along with the light patterns propagating within the tumor tissue. "A" represents a portion of the detected signal interrogating the well-perfused region, and "B" represents another portion of the detected signal, mainly passing through the poorly perfused region. Our assumption is that the total detected signal is a sum of A and B. (B) A more realistic tumor tissue model with the center poorly perfused (leading to signal A) and the periphery well perfused (leading to signal B). It demonstrates possible tumor volumes interrogated by the multichannel detectors. The total detected signal is still a sum of A plus B.

In this way, by quantifying these two ratios, we are able to obtain insight into the tumor vasculature and blood perfusion. For example, a rather uniform vascular structure will result in a ratio of γ_1/γ_2 near 1, whereas the coexistence of two time constants possibly reveals two mechanisms of regional blood perfusion in the tumor. A large time constant implies a slow perfusion through a poorly perfused area, whereas a small time constant indicates a fast perfusion through a well-perfused area. In the meantime, we can determine the ratio of the perfusion rates in these two areas after obtaining the ratios of amplitudes and time constants from the two-exponential curve fitting. In this way, we have developed a hemodynamic model for the NIR data interpretation, which allows us to associate tumor

blood oxygenation dynamics with regional blood perfusion and vascular structures of the tumor within the measured volume.

Discussions

NIRS is noninvasive and provides a real-time assessment of changes in tumor vascular hemoglobin oxygenation. In this chapter, we basically provide demonstration of the ease and utility of NIRS studies of tumors. By switching the inhaled gas from air to carbogen, the NIRS measurement produces a rapid biphasic elevation in $\Delta[\text{HbO}]$. The rapid time constant is in the range of seconds to a minute, whereas the slow component (10 to 50 times slower) continues for many minutes (see Figs. 7B and 8). The elevated oxygenation process is completely reversible upon returning air breathing, but still present 10 to 20 min after the baseline inhalation in many cases (see Figs. 7B and 8). The high reproducibility of results suggests that one can apply repeated interventions to explore the efficacy of interventions designed to alter tumor vascular oxygenation (e.g., vascular targeting agents). Our recent study has also shown that tumor response to oxygen was much more rapid and fit well to a monoexponential curve. For almost every tumor in a group of seven breast tumors, the time to reach 80% of maximum elevation in $\Delta[\text{HbO}]$ was longer with carbogen intervention than with oxygen breathing.²⁴

With single-channel and multichannel NIRS, we have measured relative changes in $[\text{Hb}]_{\text{total}}$ and $[\text{HbO}]$ in breast and prostate rat tumors in response to hyperoxic respiratory intervention. We observed that respiratory challenge caused $\Delta[\text{HbO}]$ to rise promptly and significantly in both breast and prostate tumors. However, the total concentration of hemoglobin did not always behave consistently. The dynamic changes of tumor oxygenation can be modeled by a two-exponential expression with a fast and slow time constant. Based on the model, we suggest that the NIRS measurement can "see" two vascular mechanisms during tumor oxygenation under hyperoxic gas intervention. By fitting the two-exponential model with the NIR experimental data, we can determine the two time constants and their corresponding amplitudes, leading to the relationships between the two perfusion rates and between the vascular structures, as expressed in Eq. (18).

With this tumor model, we are able to obtain information on the blood perfusion of tumor: a large time constant usually represents a slow blood perfusion, whereas a small time constant indicates a fast blood perfusion. A combination of well-perfused and poorly perfused mechanisms in tumor vasculature will result in coexistence of two time constants. Indeed, some tumor lines have been reported with only 20–85% of vessels

perfused,⁶¹ and it is known that tumor structures and oxygen distribution are highly heterogeneous.^{46,62} Therefore it is highly possible that our NIRS readings often detect a mixture of both well-perfused and poorly perfused regions in the tumor, depending on the locations of sources and detectors of the NIR system.

In the process of developing the model, we introduced a vasculature coefficient, γ . We expect that γ depends on (1) oxygen consumption and (2) capillary density of the tumor. Further studies are underway to quantify more about this coefficient and to confirm our speculations.

As an example to demonstrate the direct use of the newly developed model, the multichannel NIR results are fitted with the model, and the corresponding fitted parameters are listed in Table I. It is reasonable to expect that the central region of a solid tumor is close to necrosis (i.e., a poorly perfused region), whereas the tumor peripheral region is highly vascularized. Then, Fig. 12B can be used to schematically illustrate possible tumor volumes interrogated by the multichannel detectors. Close inspection of Table I reveals that the tumor structure ratios of γ_1/γ_2 from the three respective detectors are significantly different, whereas the perfusion ratios of f_1/f_2 from detectors 1 and 3 are almost doubled with respect to that from detector 2. Besides the results presented here, we have observed similar ΔHbO profiles and fitted parameters from other breast tumors. In such a way, we can obtain more details of tumor heterogeneity by having more source-detector pairs in the measurements. Indeed, we are now in the process of developing a multichannel NIR imaging system, along with the imaging reconstruction algorithm, so that tumor heterogeneity can be studied with better spatial resolution.

The time constants are not source-detector separation-sensitive. Equations (6), (7), and (11) demonstrate that ΔHbO and ΔHb are proportional to $1/d$, where d is the source-detector separation. This indicates that a different d value will only stretch or compress an entire temporal profile of ΔHbO , but it does not change the transient behavior of time response. The same argument can apply to DPF. Currently we have grouped DPF into the unit of $[\text{HbO}]$ for simplicity. If the DPF value is larger than 1, the values of $\Delta[\text{HbO}]$ and $\Delta[\text{Hb}]_{\text{total}}$ will decrease by a factor of DPF. However, this decrease does not affect the time constants, τ_1 and τ_2 the dynamic responses of tumor $\Delta[\text{HbO}]$ to respiratory intervention.

⁶¹ H. J. J. A. Bernsen, P. F. J. W. Rijken, T. Oostendorp, and A. J. van der Kogel, *Br. J. Cancer* 71, 721 (1995).

⁶² R. P. Mason, P. P. Anich, E. E. Babcock, A. Constantinescu, P. Peschke, and E. W. Hahn, *Int. J. Radiat. Oncol. Biol. Phys.* 29, 95 (1994).

The simultaneous measurements of $\Delta[\text{HbO}]$ and ΔpO_2 , shown in this chapter, demonstrate the compatibility of the NIRS system with the needle electrode and the FOXY fiber-optic oxygen-sensing system, without interference. All three systems are relatively inexpensive and provide real-time measurements, but the needle electrode and the three-channel FOXY system monitor pO_2 (viz., ΔpO_2) in specific locations, whereas the NIRS system provides global measurements. There are a few advantages of the FOXY system over the needle electrode: (1) it allows multiple locations to be interrogated simultaneously and (2) it is much easier to use than electrodes, particularly in calibration and stability. However, the FOXY probes may not provide accurate absolute pO_2 readings.

It is well known that measurements of tumor pO_2 have prognostic value in the clinic.^{28,63} In this chapter, we have shown a linear correlation between tumor ΔHbO and mean ΔpO_2 (Fig. 10) when a tumor undergoes a hyperoxic respiratory intervention, and thus the noninvasive NIRS monitoring could have a potential value for clinical practice. The major deficiency in our current approach is lack of spatial resolution, so implementation of an NIR imaging system for tumor monitoring is our current effort.

NIRS provides a global assessment, in contrast to blood oxygenation level dependent (BOLD)-MRI, which can provide high-resolution images.^{64,65} Although the latter approach can show heterogeneity in both temporal and spatial response, the results are often summarized to show mean values only. As such, an a priori global measurement can provide similar insight into dynamic tumor physiology or drug pharmacodynamics, while being more cost-effective, portable, and easier to implement and operate. For example, several groups of researchers have previously used NIR studies of tumors to observe the influence of chemotherapy,⁵² pentobarbital overdose,⁵² ischemic clamping,⁶⁶ and infusion of perfluorocarbon blood substitute.⁶⁷ All of these investigations demonstrate potential versatility of the NIRS application for diverse future studies.

Furthermore, the setup in our NIRS uses transmission mode between the source and detector, which we believe probes large and deep portions of the tumor, including the periphery on each side, as well as the center (see Fig. 3). This is in contrast to the setups used by most other investigators,

⁶³ M. Höckel and P. Vaupel, *J. Natl. Cancer Inst.* **93**, 266 (2001).

⁶⁴ S. P. Robinson, D. R. Collingridge, F. A. Howe et al., *NMR Biomed.* **12**, 98 (1999).

⁶⁵ X. Fan, J. N. River, M. Zamora et al., *Int. J. Radiat. Oncol. Biol. Phys.* **54**, 1202 (2002).

⁶⁶ F. Steinberg, H. J. Röhrborn, K. M. Scheufler, T. Otto, and C. Streffer, *Adv. Exp. Med. Biol.* **428**, 69 (1996).

⁶⁷ H. D. Sostman, S. Rockwell, A. L. Sylva, D. Madwed, G. Cofer, H. C. Charles, R. Negro-Villar, and D. Moore, *Magn. Reson. Med.* **20**, 253 (1991).

who apply reflectance mode,^{21,66,68} which predominately detects the behavior of the peripheral vasculature. Indeed, the dynamic results measured from breast tumors reported by Hull et al.²¹ are consistent with the fast component that we have observed and attributed to the well-perfused regions of our tumors.

Given the evidence for intratumoral heterogeneity from MRI^{46,69} and histology,⁷⁰ it will be important to advance the NIRS system to an NIR imaging system so as to study not only dynamic, but also spatial aspects of blood oxygenation in tumor vasculature. In the meantime, we believe the preliminary results reported here are proof of principle for NIR imaging of tumor vascular oxygenation, laying a foundation for more extensive studies to correlate NIR imaging measurements with tumor heterogeneity and heterogeneous responses to various tumor therapeutic interventions and treatments.

Conclusions

In conclusion, we believe that NIRS presents a new potential imaging modality to examine tumor vasculature rapidly, noninvasively, and cost-effectively. Ease of implementation and operation permit rapid application to accessible tumors in cancer patients. The inherent compatibility of fiber-optics technology and light with other modalities, such as electrodes^{20,24} and MRI,⁷¹ will facilitate multiparametric multimodality investigations of tumor heterogeneity and vasculature in the near future.

In summary, we have demonstrated in this chapter that the NIR technology can provide an efficient, real-time, noninvasive means for monitoring vascular oxygenation dynamics in tumors during hyperoxic respiratory challenge. Concentration changes in HbO measured from both breast and prostate tumors often display a very prompt rise, followed by a gradual persistence throughout the intervention. By developing a hemoperfusion model with two exponential terms and fitting the model to the ΔHbO data, we have recognized two perfusion mechanisms in tumor vasculature and quantified the ratios of the two perfusion rates.

Furthermore, we have also obtained tumor pO_2 measurements using a needle electrode or multichannel, fiber-optic, FOXY probe in simultaneous conjunction with the noninvasive NIRS measurement. The comparative

⁶⁸ M. Kragh, B. Quistorff, and P. E. Kristjansen, *Eur. J. Cancer* **37**, 924 (2001).

⁶⁹ S. P. Robinson, F. A. Howe, L. M. Rodrigues, M. Stubbs, and J. R. Griffiths, *Semin. Radiat. Oncol.* **8**, 198 (1998).

⁷⁰ B. M. Fenton, *Radiother. Oncol.* **44**, 183 (1997).

⁷¹ G. Gulsen, H. Yu, J. Wang, O. Nalcioğlu, S. Merritt, F. Bevilacqua, A. J. Durkin, D. J. Cuccia, R. Lanning, and B. J. Tromberg, *Technol. Cancer Res. Treatment* **1**, 497 (2002).

results exhibit a linear correlation between ΔHbO and ΔpO_2 of the tumors under hyperoxic gas intervention, suggesting that the NIRS approach could have a good potential value in the clinic. Finally, the newly developed tumor hemodynamic model allows us to reveal tumor heterogeneities at different tumor locations based on the multichannel NIRS results. Through this chapter, we lay a foundation for an NIR imaging technique to be further developed to facilitate investigations of tumor heterogeneity and vascular perfusion. Such a noninvasive imaging approach can enhance our understanding of the dynamics of tumor oxygenation and the mechanism of tumor physiology under baseline and perturbed conditions.

Acknowledgments

This work was supported in part by the Department of Defense Breast Cancer Research grants BC990287 (HL) and BC000833 (YG), and NIH R01 CA79515 (NCI)/EB002762 (NIBIB) (RPM). We are grateful to Vincent Bourke for his collaborative work on multichannel pO_2 measurements and Dr. Anca Constantinescu for her assistance with all the tumor investigations. We also gratefully acknowledge Dr. Britton Chance for his technical support on the multichannel NIR system.

[18] Measuring Changes in Tumor Oxygenation

By DAWEN ZHAO, LAN JIANG, and RALPH P. MASON

Introduction

Significance of pO_2 in Oncology

It has long been appreciated that hypoxic tumor cells are more resistant to radiotherapy.¹ Indeed, a 3-fold increase in radio resistance may occur when cells are irradiated under hypoxic conditions compared with oxygen pressure $\text{pO}_2 > 15$ torr for a given single radiation dose. However, recent modeling has indicated that the proportion of cells in the range 0–20 torr may be most significant in terms of surviving a course of fractionated radiotherapy.² Certain chemotherapeutic drugs also present differential efficacy, depending on hypoxia.^{3,4} Increasingly, there is evidence that hypoxia also

¹ L. Gray, A. Conger et al., *Br. J. Radiol.* **26**, 638 (1953).

² B. G. Wouters and J. M. Brown, *Radiat. Res.* **147**, 514 (1997).

³ B. Teicher, J. Lazo et al., *Cancer Res.* **41**, 73 (1981).

⁴ A. C. Sartorelli, *Cancer Res.* **48**, 775 (1988).

influences such critical characteristics as angiogenesis, tumor invasion, and metastasis.^{5–8} Moreover, repeated bouts of intermittent hypoxic stress may be important in stimulating tumor progression.⁹ Thus the ability to measure pO_2 noninvasively and repeatedly, with respect to acute or chronic interventions, becomes increasingly important.

Early work examined cells *in vitro*, where ambient oxygen concentrations are readily controlled. *In vivo*, hypoxia may be achieved by clamping the blood supply to a tumor,¹⁰ but other levels of oxygenation reflect the interplay of supply and consumption.^{11,12} Robust fine-needle polarographic electrodes opened the possibility of measuring pO_2 in tumors *in situ* and *in vivo* to define local pO_2 under baseline conditions or with respect to interventions. In early work, Cater and Silver¹³ showed the ability to monitor pO_2 at individual locations in patients' tumors with respect to breathing oxygen. Later, Gatenby et al.¹⁴ showed that pO_2 in a tumor was correlated with clinical outcome. Tumor oximetry received its greatest boost with the development of the Eppendorf Histograph polarographic needle electrode system.¹⁵ This computer-controlled device equipped with a stepper motor can reveal distributions of tumor oxygenation and has been applied extensively to clinical trials. Many reports have now shown that tumors are highly heterogeneous and have extensive hypoxia; furthermore, strong correlations have been shown in cervix and head and neck tumors between median pO_2 or hypoxic fraction and survival or disease-free survival.^{5,16–20} Extensive hypoxia also has been found in tumors of the prostate and breast.^{21–23} Thus tumor oxygenation is now recognized as a strong

⁵ E. K. Roestad, K. Sundfor et al., *Br. J. Cancer* **83**, 354 (2000).

⁶ K. De Jaeger, M. C. Kavanagh et al., *Br. J. Cancer* **84**, 1280 (2001).

⁷ M. Höckel and P. Vaupel, *J. Natl. Cancer Inst.* **93**, 266 (2001).

⁸ H. J. Knowles and A. L. Harris, *Breast Cancer Res.* **3**, 318 (2001).

⁹ R. A. Cairns, T. Kalliomaki et al., *Cancer Res.* **61**, 8903 (2001).

¹⁰ J. Moulder and S. Rockwell, *Int. J. Radiat. Oncol. Biol. Phys.* **10**, 695 (1984).

¹¹ T. W. Secomb, R. Hsu et al., *Adv. Exp. Med. Biol.* **454**, 629 (1998).

¹² M. W. Dewhirst, B. Klitzman et al., *Int. J. Cancer* **90**, 237 (2000).

¹³ D. Cater and I. Silver, *Acta Radiol.* **53**, 233 (1960).

¹⁴ R. A. Gatenby, H. B. Kessler et al., *Int. J. Radiat. Oncol. Biol. Phys.* **14**, 831 (1988).

¹⁵ M. Nozue, I. Lee et al., *J. Surg. Oncol.* **66**, 30 (1997).

¹⁶ D. M. Brizel, S. P. Scully et al., *Cancer Res.* **56**, 941 (1996).

¹⁷ M. Höckel, K. Schlenger et al., *Cancer Res.* **56**, 4509 (1996).

¹⁸ M. Nordmark, M. Overgaard et al., *Radiother. Oncol.* **41**, 31 (1996).

¹⁹ A. W. Fyles, M. Milosevic et al., *Radiother. Oncol.* **48**, 149 (1998).

²⁰ T. H. Knocke, H. D. Weimann et al., *Radiother. Oncol.* **53**, 99 (1999).

²¹ P. W. Vaupel, K. Schlenger et al., *Cancer Res.* **51**, 3316 (1991).

²² P. Hohenberger, C. Felger et al., *Breast Cancer Res. Treat.* **48**, 97 (1998).

²³ B. Movsas, J. D. Chapman et al., *Urology* **53**, 11 (1999).

Investigation of breast tumor hemodynamics using tumor vascular phantoms and FEM simulations

Jae G. Kim and Hanli Liu

Joint Program in Biomedical Engineering, University of Texas Southwestern Medical Center at Dallas and University of Texas at Arlington,
Arlington, Texas 76019

Tel: (817) 272-2054; FAX: (817) 272-2251; email address: hanli@uta.edu

Abstract: We have developed dynamic tumor vascular phantoms and utilized the finite element method to investigate the bi-phasic behavior of oxyhemoglobin concentration increase that were observed *in vivo* from rat breast tumors during carbogen inhalation.

©2004 Optical Society of America

OCIS codes: (170.1470) blood/tissue constituent monitoring; (170.3660) Light propagation in tissues; (170.4580) Optical diagnostics for medicine; (170.6510) Spectroscopy, tissue diagnostics

1. Introduction

Solid tumors develop regions of hypoxia during their growth due to an imbalance between the rate of tumor cell proliferation and branching of the blood vessels [1,2]. Tumor hypoxia can contribute to the failure of radiotherapy [3], some forms of chemotherapy [4] and photodynamic therapy [5]. In addition, a number of clinical trials have found that patient survival measured either as tumor regression or as local control depends highly on tumor oxygenation [6]. Therefore, increasing tumor oxygenation could improve cancer therapy efficiency. As one means to improve tumor oxygenation, breathing hyperoxic gas has been used to enhance cancer treatment efficacy.

Based on near infrared spectroscopy (NIRS) measurements, our previous *in vivo* animal study has clearly demonstrated that carbogen (95% CO₂ and 5% O₂) inhalation can improve the vascular oxygen level of breast tumors [7]. The observed changes in tumor vascular oxygenation ($\Delta[\text{HbO}_2]$) exhibited a rapid increase, followed by a gradual but significant increase, in response to carbogen intervention. To explain these biphasic behaviors of tumor hemodynamics, we established a mathematical model based on Kety's approach [8], and we formed a hypothesis that tumor vasculature is comprised with a well-perfused and poorly perfused region to explain why there are two different time constants in the $\Delta[\text{HbO}_2]$ data. The mathematical model further allows us to associate the signal amplitudes to the ratio of vascular coefficients and the ratio of the perfusion rates in the two different regions.

Even though we associated our fitting parameters of the NIR measurements mathematically with physiological factors, such as tumor vascular coefficients and perfusion rates, we did not provide solid validation for the model at the time. In this study, to further investigate breast tumor vasculature and to interpret the mathematical model, we designed and developed a tumor hemodynamic phantom for multi-channel NIRS experiments. Furthermore, we used the FEMLAB software to simulate the dynamic processes of light distribution in tumor hemodynamic phantoms, giving rise to better understanding of the association between the NIR readings and tumor physiological parameters.

2. Materials and methods

2.1 Mathematical Model of Tumor Vascular Oxygenation

The mathematical model for tumor vascular oxygenation during carbogen inhalation has been described in details in our previous report [7]. Briefly, we followed an approach used to measure regional cerebral blood flow (rCBF) with diffusible radiotracers, as originally developed by Kety [8] in the 1950's. By applying Fick's principle and assuming that tumor has two distinct perfusion regions, the measured NIRS signal, which has a double-exponential feature observed in the rat tumor experiments, can be expressed as

$$\begin{aligned} \Delta\text{HbO}_2^{\text{vasculature}}(t) &= \gamma_1 H_0 [1 - \exp(-f_1 t / \gamma_1)] + \gamma_2 H_0 [1 - \exp(-f_2 t / \gamma_2)] \\ &= A_1 [1 - \exp(-t / \tau_1)] + A_2 [1 - \exp(-t / \tau_2)], \end{aligned} \quad (1)$$

where H_0 is the arterial oxygenation input, f_1 and γ_1 are the blood perfusion rate and the vasculature coefficient in region 1 for the well perfused region, respectively; f_2 and γ_2 have the same respective meanings in region 2 for the poorly perfused region, and $A_1 = \gamma_1 H_0$, $A_2 = \gamma_2 H_0$, $\tau_1 = \gamma_1 / f_1$, $\tau_2 = \gamma_2 / f_2$. Basically, A_1 , A_2 , τ_1 , and τ_2 can be determined from the NIRS measurements by fitting equation (1) with the experimental data. It follows that the ratios of two vasculature coefficients, γ_1 / γ_2 , and the two blood perfusion rates, f_1 / f_2 , can be obtained as

$$\frac{\gamma_1}{\gamma_2} = \frac{A_1}{A_2}, \quad \frac{f_1}{f_2} = \frac{A_1 / A_2}{\tau_1 / \tau_2} \quad (2)$$

2.2 Tumor Hemodynamic Phantom and Multi-Channel NIR Spectroscopy

To represent vascular blood vessels in tumor, we designed a vascular modeling device (VMD) by winding a small diameter tube (I.D.=0.51 mm) around a big diameter core tube (O.D.=14.4 mm). Tumor hemodynamic phantom was fabricated by embedding two VMDs into a cylindrical shape of gel, which is made of Intralipid and gelatin powder to represent tissues. The optical properties of tumor gel phantom were measured using near infrared tissue spectrometer (model: 96208, ISS Inc., Champaign, IL), and those values were close to tissue optical properties ($\mu_a = 0.032 \text{ cm}^{-1}$, $\mu_s = 9.2 \text{ cm}^{-1}$ at 750 nm).

Schematic experimental setup for tumor hemodynamic phantom study is shown in Figure 1a. As shown here, NIR light at 730 nm from a multi-channel NIRS system was delivered to the tumor hemodynamic phantom, and three optical detectors were placed on the side of cylindrical phantom (D1, D2, and D3 in Fig. 1b) to collect signals, which were then processed in the computer. A certain amount of ink was injected into the two VMDs by two syringe pumps (model KDS200, KdScientific Inc., New Hope, PA), and the ink wastes were collected in the waste beaker. We used two syringe pumps so that we could control different ink flow rates for different VMDs.

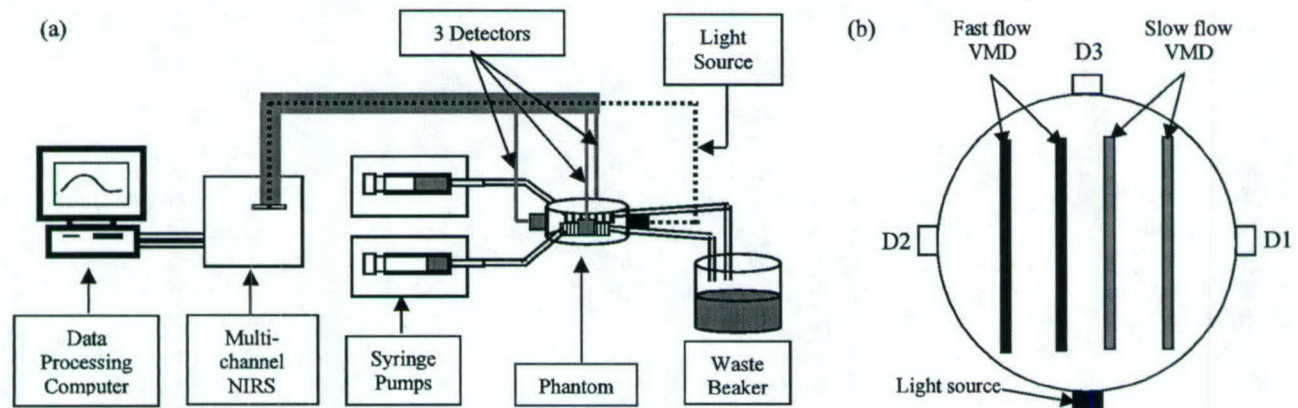


Fig. 1(a) Schematic diagram of tumor vascular phantom experimental setup. (b) The geometry of FEM simulation for tumor hemodynamic phantom.

2.3 FEM Simulation

To further investigate bi-phasic features of tumor hemodynamics, we used the FEMLAB software (COMSOL Inc. Burlington, MA), which is based on the finite element method, to simulate our dynamic tumor phantom experiments. The geometry of FEM simulations for the tumor hemodynamic phantom is shown also in Figure 1b, and it represents a 2-dimensional horizontal cross section of our tumor vascular phantom. The large circle represents the body of tumor phantom (diameter = 4 cm), and each VMD used in the dynamic phantom is represented by two thin rectangles (0.1 x 2.4 cm rectangle) within the circle as a blood vessel network: left two rectangles are for the vessels with a fast flow rate, and right two rectangles denote the vessels with a slow flow rate.

In the simulation, we used a uniform reduced scattering coefficient of 10 cm^{-1} for both the background and vasculature. Two absorption coefficients of 0.03 and 1.5 cm^{-1} were used to simulate the phantom and ink absorption in VMDs, respectively. The FEM model was performed with 1147 elements and 609 nodes and solved for the light distribution within the vascular phantom dynamically, using the stationary nonlinear solver type.

3. Results

Figure 2a shows the changes of absorption from the three detectors on the tumor hemodynamic phantom. Since two VMDs are having same inner diameter (0.51 mm), the velocities of ink in VMDs will be totally depending on the ink flow rates controlled by the two syringe pumps. The first step for this experiment was injecting ink only into left VMD with a flow rate of 20 ml/hr. As a result, D2 showed largest increase of $\Delta\mu_a$ while D1 showed smallest increase of $\Delta\mu_a$ because D1 was located quite away from the left VMD. For the second step, right VMD was injected with ink at the same flow rate of 20 ml/hr. Here, D1 showed largest increase of $\Delta\mu_a$ and D2 showed

smallest increase of $\Delta\mu_a$. Then, as the third step, the ink solution was injected into both left and right VMDs with the same flow rate (20 ml/hr). In all of the above cases, the signals from D3 showed similar profiles as the others, without clear bi-exponential patterns. For the fourth step, we injected ink into both VMDs, but with two different flow rates: 5 ml/hr for right VMD and 20 ml/hr for the left VMD. Now we can see that bi-exponential behavior appears on D3 since D3 is detecting signals from both left and right VMDs, which have two different ink flow rates.

For the further analysis, $\Delta\mu_a$ increases detected from the three detectors at step 4, as shown in Figure 2a, were fitted by using our mathematical model to obtain amplitudes and time constants values (Figure 2b). The time constant analysis shows that the $\Delta\mu_a$ increases from D1 and D2 are well fitted by the mono-exponential model, while $\Delta\mu_a$ increases from D3 is fitted well with the double exponential model, i.e., eq. (1). There exist a fast and slow time constants with $\tau_1 = 18.1 \pm 0.9$ sec and $\tau_2 = 134. \pm 11$ sec from D3, and they are well matched with τ_1 in D2 ($= 20.9 \pm 0.5$ sec) and τ_1 in D1 ($= 131. \pm 3$ sec). All of these suggest that the bi-phasic $\Delta\mu_a$ signals obtained from D3 with a fast and slow component indeed result from the dynamic changes in both left and right VMDs. We have further confirmed the same results from the FEM simulations on tumor hemodynamic phantom experiments.

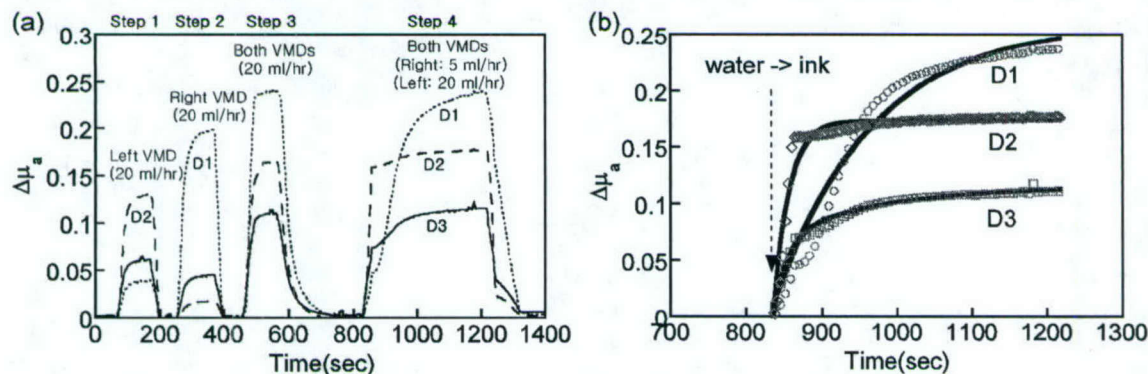


Fig. 2 (a) Effects of overdose KCl injection on tumor vascular $\Delta[\text{HbO}_2]$ and $\Delta[\text{Hb}]_{\text{total}}$ for a breast tumor (12.7 cm^3), (b) relationship between the tumor oxygen consumption rate and tumor volume.

4. Discussion and Conclusions

We have developed dynamic tumor phantom models to demonstrate our hypothesis on tumor hemodynamics during carbogen inhalation. We believe that the bi-phasic feature of tumor blood oxygenation increases during carbogen inhalation is highly associated with distinct vascular structures of the tumors, which are composed of well-perfused and poorly perfused region. We found that the two time constants in tumor hemodynamic models can result from different blood flow velocities or anything that can cause changes in blood flow velocities, such as blood vessel diameter and length. Also, the FEM simulation based on light diffusion equation was performed to simulate the tumor phantom experiments, and the results were well matched with the experiments, further supporting our previous hypothesis and the mathematical model.

5. Acknowledgements: This work was supported in part by the Department of Defense Breast Cancer Research grants of DAMD17-03-1-0353 (JGK) and BC990287 (HL).

6. References

- ¹ P. Vaupel, O. Thews, D. K. Kelleher, and M. Höckel, "Current status of knowledge and critical issues in tumor oxygenation", In: Hudetz and Bruley (eds), *Oxygen Transport to Tissue XX*, 591-602, Plenum Press, New York, 1998.
- ² P. Vaupel, "Oxygen transport in tumors: Characteristics and clinical implications", *Adv. Exp. Med. Biol.*, **388**, 341-351, 1996.
- ³ R. H. Thomlinson, and L. H. Gray, "The histological structure of some human lung cancers and the possible implications for radiotherapy", *Br. J. Cancer*, **9**, 539-549, 1955.
- ⁴ B. Teicher, J. Lazo, and A. Sartorelli, "Classification of antineoplastic agents by their selective toxicities toward oxygenated and hypoxic tumor cells", *Cancer Res.*, **41**, 73-81, 1981.
- ⁵ J. D. Chapman, C. C. Stobbe, M. R. Arnfield, R. Santus, J. Lee, and M. S. McPhee, "Oxygen dependency of tumor cell killing *in vitro* by light activated photofrin II", *Radiat. Res.*, **126**, 73-79, 1991.
- ⁶ A. W. Fyles, M. Milosevic, R. Wng, M. C. Kavanagh, M. Pintile, A. Sun, W. Chapman, W. Levin, L. Manchul, T. J. Keane, and R. P. Hill, "Oxygenation predicts radiation response and survival in patients with cervix cancer", *Radiother. Oncol.*, **48**, 149-156, 1998.
- ⁷ H. Liu, Y. Song, K. L. Worden, X. Jiang, A. Constantinescu, and R. P. Mason, "Noninvasive Investigation of Blood Oxygenation Dynamics of Tumors by Near-Infrared Spectroscopy", *Applied Optics*, **39**(28), 5231-5243, 2000.
- ⁸ S. S. Kety, "The theory and applications of the exchange of inert gas at the lungs and tissue," *Pharmacol. Rev.*, **3**, 1-41, 1951.